Measurement of the decay parameter ρ and a search for non-Standard Model decays in the muon decay spectrum

by

Ryan D. Bayes
B.Sc., Simon Fraser University, 2003
M.Sc., University of Victoria, 2006

A Dissertation Submitted in Partial Fulfillment of the
Requirements for the Degree of

DOCTOR OF PHILOSOPHY

in the Department of Physics and Astronomy

Measurement of the decay parameter ρ and a search for non-Standard Model decays in the muon decay spectrum

by

Ryan D. Bayes
B.Sc., Simon Fraser University, 2003
M.Sc., University of Victoria, 2006

Supervisory Committee

Dr. A. Olin, Co-Supervisor
(Department of Physics and Astronomy)

Dr. R. Kowalewski, Co-Supervisor
(Department of Physics and Astronomy)

Dr. D. Karlen, Departmental Member
(Department of Physics and Astronomy)

Dr. J. Alberts, Departmental Member
(Department of Physics and Astronomy)

Dr. R. N. Horspool, Outside Member
(Department of Computer Science)

Supervisory Committee

Dr. A. Olin, Co-Supervisor
(Department of Physics and Astronomy)

Dr. R. Kowalewski, Co-Supervisor
(Department of Physics and Astronomy)

Dr. D. Karlen, Departmental Member
(Department of Physics and Astronomy)

Dr. J. Alberts, Departmental Member
(Department of Physics and Astronomy)

Dr. R. N. Horspool, Outside Member
(Department of Computer Science)

ABSTRACT

The study of the muon decay process $\mu^+ \rightarrow e^+\nu_e\bar{\nu}_\mu$ is a powerful constraint on the behaviour of the weak interaction, without contamination of the other, stronger, fundamental interactions. The spectrum measured from the momentum and angles of the decay positrons is parametrized using a set of four decay parameters. The purpose of the TWIST experiment is to measure these decay parameters to an unprecedented precision; an order of magnitude improvement in the uncertainties over measurements completed before the TWIST experiment. Measurements of the muon decay parameters constrain the values of a series of 19 weak coupling constants. In the standard model, V-A weak interaction, 18 of these constants are 0, while the remaining constant describes interactions between left handed particles, $g^V_{LL} = 1$.

The decay parameter ρ quantifies the behaviour of the spectrum with respect to momentum. According to the standard model the value of this parameter is 3/4. TWIST measured a value of $\rho = 0.74991 \pm 0.00009(\text{stat}) \pm 0.00028(\text{sys})$. The measurement is limited by its systematic uncertainty, so a large focus of the experiment was on the determination and control of these uncertainties. The systematic uncertainties are derived from uncertainties in the detector construction and uncertainties in the biases generated by differences between the data and a matching Monte Carlo.

Muon decay also limits the possibility of family symmetry breaking interactions. TWIST can be used to search for the possibility of muons decaying into a positron and a single unidentified neutral particle $\mu^+ \rightarrow e^+ X^0$ that does not otherwise interact with normal matter. The large momentum and angle acceptance of the TWIST spectrometer allows for searches of two body decays for masses of the X^0 boson $m_{X^0} \in [0, 80]$ MeV/c, with a variety of behaviours with respect to the angle of the positron track. Upper limits on massive and mass-less X^0 decays are set with a 90% confidence level separately at parts in 10^6 for massive decays and 10^5 for mass-less decays.

Contents

List of Tables

List of Figures

ACKNOWLEDGEMENTS

I would like to thank:

My wife Lindsay, for her quiet wisdom, and not so quiet support.

Art Olin, Glen Marshall, and Dick Mischke, for mentoring, support, encouragement, and patience.

My fellow graduate students, for their friendship, understanding, and really good ideas.

DEDICATION

For Kiona. May the breadth of your horizons never exceed your grasp.

Chapter 1

Introduction

The standard model of particle physics is the great incomplete success of 20th century physics. This model describes all observations made in particle physics with a few minor exceptions. It describes all matter in the context of six "light" particles, or leptons, grouped in three families, six quarks, also grouped in three "families", and four force moderating fields. This arrangement is shown graphically in Fig. 1.1. The interactions are described succinctly using a set of operations in the mathematical symmetry $SU(3) \times SU(2)_L \times U(1)$, where the $SU(3)$ symmetry describes the strong interactions between the quarks, and the $SU(2) \times U(1)$ broken symmetry describes the behaviour of electromagnetic and weak interactions.

The incompleteness of the standard model appears in its requirement to insert a number of its parameters by hand, with no theoretical motivation, and in the observation of neutrino mass, where the standard model assumed the neutrino to be mass-less. Extensions to the standard model accounting for the neutrino mass have been made. Measurements of the free parameters of the Standard model have been carried out to various degrees of precision.

One feature of the standard model is the maximal parity violation that appears in the weak interaction. The consequence of this behaviour is that weak interactions only occur between left handed "helicity" particles, in an interaction mediated by a spin one vector boson. While the standard model is built with this behaviour, the source of this description is entirely based on experiment.

The TRIUMF weak interaction symmetry test (TWIST) is an explicit test of the parity violation in the standard model weak interaction. The purpose is to study the weak interaction via the process of muon decay. The muon is a massive lepton, 200 times more massive than the electron, that almost always decays into an electron,

or for positively charged muons, into a positron, and two neutrinos. This decay is mostly free of strong interaction effects, making it an attractive system for the study of weak decay processes.

The muon was discovered in 1938 in cosmic rays using measurements from cloud chambers. The mass and charge properties of the particle where not consistent with any particle known at the time. The new particle was called the mesotron and was associated with the massive particle postulated by Yukawa to mediate interactions within the nucleus [6]. Further experiments conducted in 1946 by Conversi, Pancini, and Piccioni found that this particle decayed at rest in matter, rather than interacting with the nucleus as would the Yukawa particle [7]. The mystery was resolved in 1947 by Powell *et al* [8] when they discovered a second particle in cosmic rays which they called π or the "pion", which turned out to be the true Yukawa particle. They

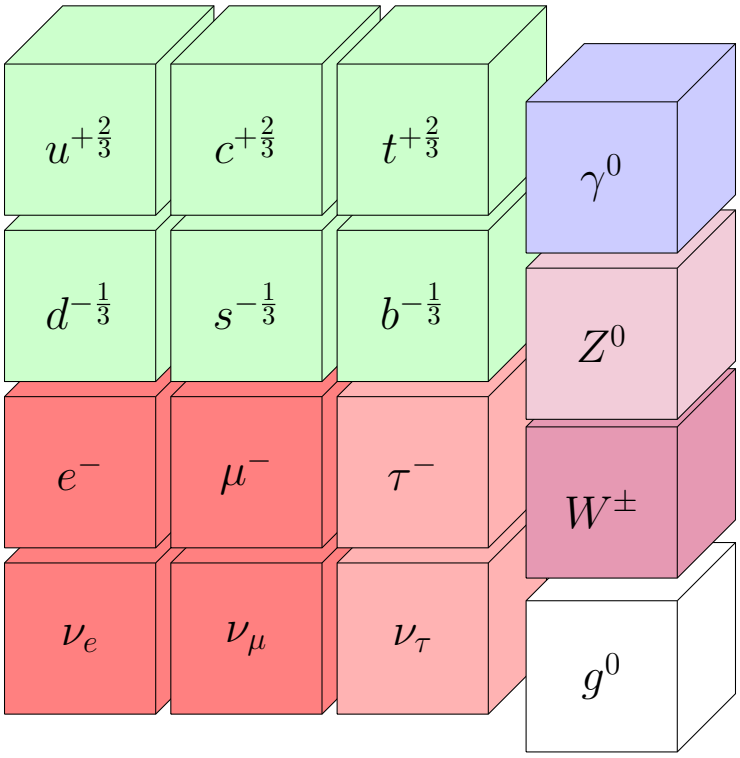

Figure 1.1: Schematic depiction of the standard model of particle physics. Quarks are shown in green, the leptons are shown in red, and the bosons are shown vertically on the right. The TWIST experiment studies the behaviour of the anti particles of the μ^- and e^- particles shown with the heavier shading as well as their corresponding neutrinos. In the standard model this interaction is mediated by the W^+ boson also highlighted.

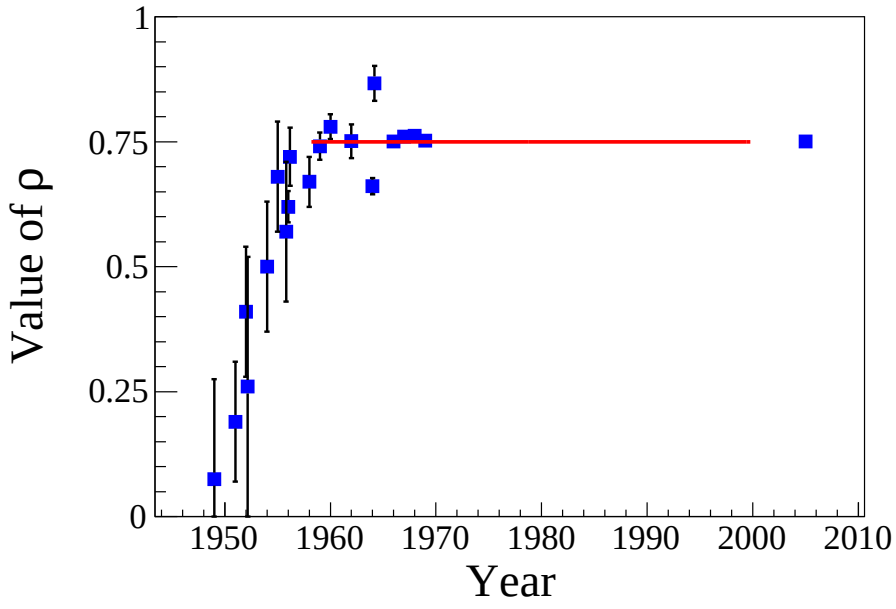

Figure 1.2: Measurements of the muon decay parameter, ρ, as a function of time. The results were compiled by Rosenson [2], Sherwood [3] and the Particle Data Group [4].

then rechristened the "mesotron" particle as the μ or "muon". The shape of the electron spectrum generated by the muon decays was first measured and described by Hincks and Pontecorvo in 1948 [9] and then by Steinberger in 1949 [10] independently confirming that the decay is a four body interactions with two neutrinos.

The first theoretical description of the general spectrum of positrons from muon decay was given by Louis Michel in 1950[11]. Michel's definition of the spectrum only encompassed the behaviour of the spectrum as a function of the positron energy using two parameters, ρ and η. These parameters are sometimes known as the Michel parameters. The label has been erroneously extended to include the parameters which describe the anisotropy of the positron spectrum δ and ξ, which were first described in 1957 by Kinoshita and Sirlin. The shape of the decay spectrum and how these parameters are related to the weak coupling constants is discussed in Chapter 2. TWIST measures these muon decay parameters to an unprecedented precision.

The isotropic momentum spectrum is primarily described by the ρ as the impact of the η parameter is suppressed. Improvements in the precision of the ρ parameter improve limits on the magnitude of the weak coupling constants. Specifically, limits on right handed coupling processes can be set by improving measurements of the ρ parameter. The most recent measurements of the ρ parameter, previous to the

TWIST experiment, were conducted in the 1960s [12]. Measurements of ρ completed before 1970 are shown in Fig. 1.2. Two measurements of this decay parameter have been published by the TWIST experiment in association with the anisotropy parameter δ. The measurement described here is the final TWIST measurement and the first simultaneous measurement of the three muon decay parameters ρ, δ, and ξ completed by the experiment.

The TWIST experiment is limited by the systematics of the measurement and so most of the challenge of the experiment is in minimizing these uncertainties. A very precise spectrometer was constructed to make this measurement. This spectrometer is described here in Chapter 3. The positron tracks measured by this spectrometer are analyzed in multiple stages to determine the positron momentum and angle as described in Chapter 4. A simulation of muon decays in the TWIST detector, subject to the same analysis as the data is described in Chapter 5, and compared to the data using an analysis described in Chapter 6. The systematic uncertainties are reduced to uncertainties in the properties of the simulation relative to the real TWIST detector, either because of the physics in the simulation or uncertainties in the construction of the detector itself, as described in Chapter 7. The results of the muon decay measurements and some of their ramifications are discussed in Chapter 8.

The author's contributions included;

- Aiding data taking with multiple turns as run coordinator involving organizing personnel to run shifts, programming the activities to be accomplished during a run period, and communicating with the operations group about TWIST related issues.

- Assuming responsibility for the decay parameter fitting and energy calibration procedures. Wrote the code used to generate the relative endpoint calibration described in Section 6.2 with the goal of improving the systematics and understanding the associated physics. Studied the resulting statistical (Section 6.2.3) and systematic uncertainties (Section 7.2.3).

- Coding a script for running the event selection analysis, described in Section 4.4, in parallel on the TWIST local cluster. This allows an analysis that can take a 12 to 18 hours to be completed in 1 to 2 hours.

- Studying the biases in the analysis of positron tracks; particularly effects due to the corrections for the momentum loss and multiple scattering through the

detector which are described in Section 4.2.3.

- Studying a special set of data where the muons stopped in the far upstream end of the detector allowing for positrons to be tracked through the entire detector, described in Section 5.2. These data were used to validate the positron physics in the simulation compared directly to the data, and to study the reconstruction efficiency of the detector.

- Preparing and running simulations and analysis on the Westgrid computing cluster. Have acted a coordinator for TWIST activities on Westgrid.

- Assuming responsibility for the TWIST blackbox procedure described in Section 5.1, including generating the blackbox samples and preparing the white box test after the analysis (Section 8.1.1).

Searches for alternative decay modes have been conducted since muon decays were identified [13]. The most obvious decay mode was into an electron and a photon ($\mu^+ \rightarrow e^+\gamma$) as this is the only final state involving known particles with invariant masses less than a muon. The lack of evidence for this decay mode is a leading source of evidence for lepton family number conservation. A measurement of rare muon decays is described in Chapter 9. This special analysis was entirely the work of the author.

Chapter 2

Theory

The Standard Model (SM) is built assuming that the charged current weak interactions behave according to the maximal parity violating V-A interaction. The $V - A$ interaction is not a theoretical requirement; rather it is the theoretical assumption that best fits existing experimental data. TWIST is an example of such an experiment.

TWIST studies the decay of positive muons into positrons to verify the weak interaction model. This experiment makes two of five measurements necessary to define the weak interaction coupling [14] the others being,

- muon lifetime, which is used to define the Fermi coupling constant, G_F;
- measurements of the decay positron polarization;
- measurements of inverse muon decay with ν_μ of known helicity.

Muon decay is an attractive system for the study of the weak interaction for a number of reasons. The hadronic component of the decay is small with loop corrections affecting decay spectrum on the level of parts in 10^6. Polarized muons are also easily produced at particle accelerators, such as TRIUMF's 500 MeV proton cyclotron, from the decay of charged pions.

2.1 Lorentz Structure of Muon Decay

The most general Lorentz invariant, derivative free expression describing muon decay is the four fermion interaction [14],

$$\mathcal{M} = \frac{4G_F}{\sqrt{2}} \sum_{\substack{\gamma=S,V,T \\ \epsilon,\mu=R,L}} g^{\gamma}_{\epsilon\mu} \langle \bar{e}_{\epsilon} | \Gamma^{\gamma} | (\nu_e)_n \rangle \langle (\bar{\nu}_{\mu})_m | \Gamma_{\gamma} | \mu_{\mu} \rangle. \tag{2.1}$$

This interaction is represented graphically by the Feynman diagram shown in Fig. 2.1. This matrix describes the interaction between a left (L) or right (R) handed muon and positron, and their associated neutrinos via scalar (S), vector (V), and tensor (T) couplings. The chiralities of the neutrinos, n and m, are dictated by the handedness of the interaction muon, "μ", and positron, "ϵ". The matrices Γ^{γ} dictate how this interaction behaves under Lorentz transformations. Because the interaction is point-like, the Γ^{γ} matrices are composed of the Dirac matrices; specifically, $\Gamma^S = 1$, $\Gamma^V = \gamma^{\nu}$, and $\Gamma^T = \gamma^{\nu}\gamma^{\mu} - \gamma^{\mu}\gamma^{\nu}$. The magnitude of the decay interaction is dictated by the Fermi coupling constant, G_F. This representation is equivalent to descriptions that involve axial vector and pseudo-scalar interactions. In this chiral basis, the left handed lepton is the Dirac spinor projected using the $\frac{1}{2}(1-\gamma^5)$ operator, while the right handed lepton state is projected using a $\frac{1}{2}(1+\gamma^5)$ operator. Axial vector terms in the summation will have a $\gamma_{\mu}\gamma^5$ factor while psuedo-scalar terms will have a propagator multiplied by a γ^5 factor.

The set of complex coupling coupling constants, $g^{\gamma}_{\epsilon\mu}$, dictate the probability for any of these interactions taking place. Out of these coupling constants two, g^T_{LL} and g^T_{RR} are identically zero, and one arbitrary phase, leaving 19 degrees of freedom in this system. In the $V-A$ coupling assumed by the standard model only one coupling, g^V_{LL}, is non-zero. This requirement is set by experiment, and is not required by any fundamental symmetry law. After the expansion of the chiral spinors the interaction contains an interaction matrix for a $V-A$ coupling contains the Dirac matrix $\gamma_{\mu} - \gamma_{\mu}\gamma^5$. Pure $V+A$ coupling will have a values of $g^V_{RR} = 1$ with all other couplings zero. The expansion of the chiral spinors in the interaction matrix produces a $\gamma_{\mu} + \gamma_{\mu}\gamma^5$ term in this case. Likewise the magnitude of $S-P$ (scalar minus psuedo-scalar) terms are dictated by the g^S_{LL} coupling constant, while the magnitude of the $S+P$ coupling is dictated by the magnitude of the g^S_{RR} constant.

In the general case the coupling constants are subject to a normalization condition

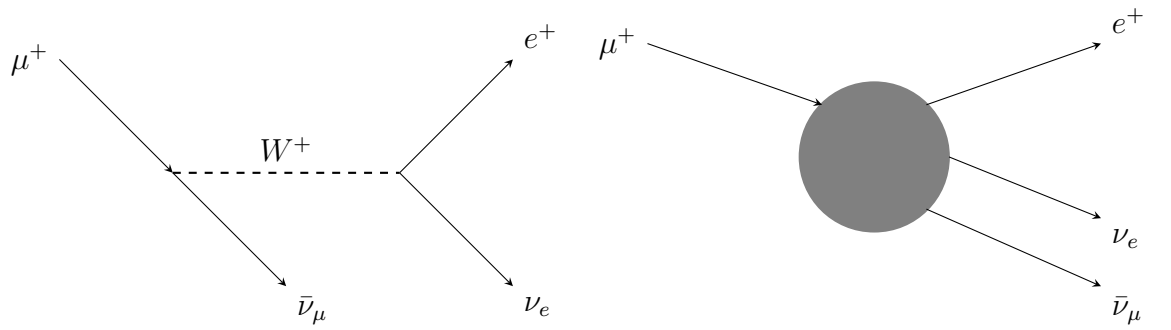

(a) Standard model muon decay (b) Muon decay as a four fermion point interaction

Figure 2.1: Feynman diagram of the decay of a muon into a positron and two neutrinos. In the standard model the interaction is moderated through the appearance of a virtual W^+ boson. The TWIST experiment instead assumes that this interaction is point-like with arbitrary couplings between the four fermions.

[15];

$$\begin{aligned} 1 &= \frac{1}{4}\left(|g^S_{RR}|^2 + |g^S_{RL}|^2 + |g^S_{LR}|^2 + |g^S_{LL}|^2\right) + \\ &\quad |g^V_{RR}|^2 + |g^V_{RL}|^2 + |g^V_{LR}|^2 + |g^V_{LL}|^2 + 3\left(|g^T_{RL}|^2 + |g^T_{LR}|^2\right). \end{aligned} \tag{2.2}$$

The terms in this condition can be rearranged according to the chiralities of the electron and the muon to define four quantities, $Q_{\epsilon\mu}$, that represent the probability of a μ handed muon to decay to a ϵ handed positron. These quantities are

$$Q_{RR} = \frac{1}{4}|g^S_{RR}|^2 + |g^V_{RR}|^2 \tag{2.3}$$

$$Q_{RL} = \frac{1}{4}|g^S_{RL}|^2 + |g^V_{RL}|^2 + 3|g^T_{RL}|^2 \tag{2.4}$$

$$Q_{LR} = \frac{1}{4}|g^S_{LR}|^2 + |g^V_{LR}|^2 + 3|g^T_{LR}|^2 \tag{2.5}$$

$$Q_{LL} = \frac{1}{4}|g^S_{LL}|^2 + |g^V_{LL}|^2 \tag{2.6}$$

where $0 \leq Q_{\epsilon\mu} \leq 1$ and $\sum_{\epsilon\mu} Q_{\epsilon\mu} = 1$[14]. Of these quantities, muon decay sets limits on Q_{RR} and Q_{LR}. Limits on Q_{LL} require measurements which limit the g^S_{LL} coupling, which can be achieved with inverse muon decays, $e^-\nu_\mu \rightarrow \mu^-\nu_e$. Two additional

quantities are important in the decay asymmetry,

$$B_{LR} = \frac{1}{16}|g^S_{LR} + 6g^T_{LR}|^2 + |g^V_{LR}|^2 \quad (2.7)$$

$$B_{RL} = \frac{1}{16}|g^S_{RL} + 6g^T_{RL}|^2 + |g^V_{RL}|^2, \quad (2.8)$$

where, $0 \leq B_{e\mu} \leq Q_{e\mu}$.

2.1.1 The Muon Decay Spectrum

The parametrization of the muon decay spectrum, first written down by Louis Michel, and later expanded by Kinoshito and Sirlin, describes the spectrum of the decay positrons without making specific assumptions about the coupling strengths. This spectrum takes the form

$$\frac{\partial^2\Gamma}{\partial x \partial \cos\theta} = \frac{m_\mu}{4\pi^3} W^4_{e\mu} G^2_F \sqrt{x^2 - x_0^2}(F(x) + |\boldsymbol{P}_\mu| \cos\theta G(x)) \quad (2.9)$$

where the positron is produced with a reduced energy between x and $x + dx$, at an angle θ with respect to the muon polarization vector $\boldsymbol{P}_\mu$. In the context of the TWIST experiment a positive muon, μ^+, is polarized in the opposite direction to its momentum when it is produced from the pion decay. The experimental θ is defined with repect to the beam line direction so $\cos\theta_{ex} = -\cos\theta_{th}$. The parameter $W_{e\mu} = \sqrt{m_\mu^2 + m_e^2}/2m_\mu$ is the maximum kinetic energy of the positron and sets the scale for the reduced energy, $x = E_e/W_{e\mu}$, and the reduced positron mass $x_0 = m_e/W_{e\mu}$.

The functions $F(x)$ and $G(x)$ describe the behaviour of the isotropic and anisotropic parts of the spectrum as functions of the reduced energy.

$$F(x) = x(1-x) + \frac{2}{9}\rho(4x^2 - 3x - x_0^2) + \eta x_0(1-x) + R.C. \quad (2.10)$$

$$`G(x) = \frac{\xi}{3}\sqrt{x^2 - x_0^2}\left(1 - x + \frac{2}{3}\delta[4x - 3 + (\sqrt{1 - x_0^2} - 1)]\right) + R.C. \quad (2.11)$$

The four parameters ρ, η, ξ, and δ are the subset of muon decay parameters that defines the shape of the positron spectrum, when the polarization of the decay positron, $\mathcal{P}_e$, is ignored. These expressions are subject to radiative corrections ($R.C.$) which are important for a high precision measurement of the decay parameters. Higher order radiative corrections to the spectrum have been calculated in the context of the $V - A$ interaction up to the leading logarithmic corrections of $\mathcal{O}(\alpha^2)$ [16] [17]. The

calculations of pure $\mathcal{O}(\alpha^2)$ corrections were not complete before the TWIST analysis started[16]. Calculation of the radiative corrections do not exist in the general case because some of the couplings are not renormalizable in higher orders. The forms and the magnitude of these contributions will be discussed in a Chapter 5.

In the limit $x = 1$ the positron spectrum is proportional to $1 - \cos\theta P_\mu \xi\delta/\rho$. The parameters are constrained such that $\rho > P_\mu \xi\delta$ to ensure that the spectrum is positive definite at all momenta and angles. This is an important, general constraint on the values of the decay parameters.

In the $V - A$ interaction $\rho = \frac{3}{4}$, $\eta = 0$, $\xi = 1$, and $\delta = \frac{3}{4}$. The muon decay spectrum assuming the $V - A$ interaction and ignoring terms proportional to the positron mass becomes,

$$\frac{\partial^2\Gamma}{\partial x \partial \cos\theta} = \frac{G_F^2 m_\mu^5}{192\pi} x^2 \left(3 - 2x + |\boldsymbol{P}_\mu| \cos\theta(2x - 1)\right) + R.C. \tag{2.12}$$

The surface defined by this theoretical spectrum, assuming $|\boldsymbol{P}_\mu| = 1$ is shown in Fig. 2.2.

The muon decay parameters are bi-linear combinations of the weak coupling con-

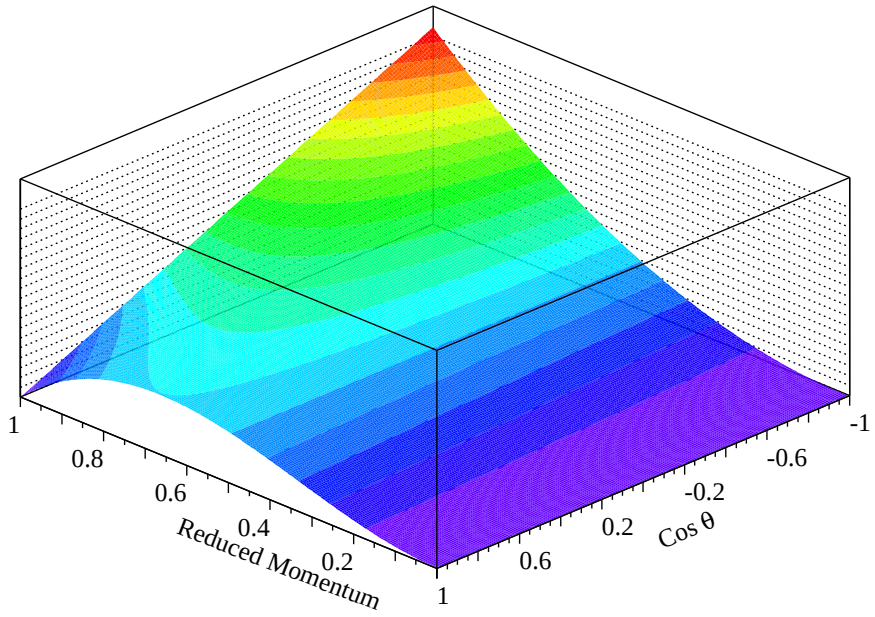

Figure 2.2: The muon decay spectrum assuming a $V - A$ interaction. Radiative corrections are not included in this spectrum.

stants. For example, ρ can be represented as

$$\rho = \frac{3}{4} - \frac{3}{4}\left(|g_{LR}^V|^2 + |g_{RL}^V|^2 + 2(|g_{LR}^T| + |g_{RL}^T|^2) + Re(g_{LR}^S g_{LR}^{T*} + g_{RL}^S g_{RL}^{T*})\right) \quad (2.13)$$

Alternatively the muon decay parameters can be represented using the interaction probability quantiles;

$$\rho = \frac{3}{4} + \frac{1}{4}(Q_{LR} + Q_{RL}) - (B_{LR} + B_{RL}), \quad (2.14)$$

$$\xi = 1 - 2Q_{RR} - \frac{10}{3}Q_{LR} + \frac{4}{3}Q_{RL} + \frac{16}{3}(B_{LR} - B_{RL}), \quad (2.15)$$

$$\xi\delta = \frac{3}{4} - \frac{3}{2}Q_{RR} - \frac{7}{4}Q_{RL} + \frac{1}{4}Q_{RL} + (B_{LR} - B_{RL}) \quad (2.16)$$

The measurement of ρ does not, by itself constrain any single coupling constant. Furthermore, these decay parameters do not directly constrain the coupling constant g_{LL}^V; this constant can only constrained by the measurements of the inverse muon decay measurements. A global analysis which includes all available information about the muon decay, as described by Fetscher *et.al.* [14] and, more recently, Gagliardi *et.al.* [18], is required to make advances in the precision of the coupling constants.

2.1.2 ρ and Physics beyond the Standard Model

The ρ parameter is sensitive to a few different Standard model extensions. This new physics comes in as a result of considering right handed couplings in muon decays.

The ρ parameter is sensitive potential mixing between W_L and W_R bosons found in left-right symmetric models [5]. In this set of models an alternate Lagrangian is assumed for the weak interaction in the lepton sector which separates the interaction into $V - A$ and $V + A$ components,

$$L = \frac{g_L}{2\sqrt{2}} W_L \left(\bar{N}^0 \gamma_\lambda (1 - \gamma_5) U^\dagger E\right) + \frac{g_R}{2\sqrt{2}} W_R \left(\bar{N}^0 \gamma_\lambda (1 + \gamma_5) V^\dagger E\right) \quad (2.17)$$

where $g_L = g_{LL}^V$ and $g_R = g_{RR}^V$ are the left and right coupling constants, N^0 is the vector of the mass eigenstates of the neutrinos, E is the vector of the charged leptons, and $U^\dagger$ and $V^\dagger$ are the neutrino mixing matrices. The W_R and W_L bosons can be

expressed as linear combinations of mass eigenstates, W_1 and W_2:

$$W_L = W_1 \cos\zeta + W_2 \sin\zeta \tag{2.18}$$
$$W_R = e^{i\omega}(-W_1 \sin\zeta + W_2 \cos\zeta). \tag{2.19}$$

Where ω is a CP violating phase, and ζ is the left-right mixing angle. The mixing angle and the W_2 mass, m_2, can be expressed in combinations,

$$t = \frac{g_R^2 m_1^2}{g_L^2 m_2^2} \tag{2.20}$$
$$\zeta_g = \frac{g_R}{g_L}\zeta \tag{2.21}$$

whose relationships are easily written in terms of the muon decay parameters. Specifically

$$\rho = \frac{3}{4}(1 - 2\zeta_g^2) \tag{2.22}$$
$$\xi = 1 - 2(t^2 + \zeta_g^2) \tag{2.23}$$
$$\delta = \frac{3}{4} \tag{2.24}$$
$$\frac{\xi\delta}{\rho} = 1 - 2t^2. \tag{2.25}$$

Thus the combination of ρ, ξ, and $\xi\delta/\rho$ define an allowed region of the $m_2 - \zeta$ phase space. Assumptions about the relative strengths of the coupling constants will dramatically alter the allowed values of $m_2 - \zeta$ given the measured muon decay parameters.

In a special case, known as the Manifest Left-Right Symmetric model, the left and right handed coupling constants are the same, that is $g_R = g_L$, the CP violating phase, $\omega = 0$ and the mixing angle becomes

$$|\zeta| = \sqrt{\frac{1}{2}(1 - \frac{4}{3}\rho)}. \tag{2.26}$$

The limit set by this relationship is unchanged when the CP violating phase is allowed to be non-zero (Pseudo-manifest left right symmetry). In a third case the restriction on the coupling constants is relaxed, making a non-manifest left right symmetric

model. The condition of Eq.2.26 is then altered by the substitution $\zeta_g = \zeta g_R/g_L$;

$$|\zeta| = |\frac{g_L}{g_R}|\sqrt{\frac{1}{2}(1-\frac{4}{3}\rho)}. \tag{2.27}$$

In both cases a limit can be set on the left-right mixing angle that is directly proportional to the value of ρ.

ρ is also potentially sensitive to the neutrino mass [19]. Changes in ρ, resulting from the inclusion of $V+A$ interaction couplings which are allowed by the massive neutrinos, are measurable by a muon decay experiment such as TWIST. The weak coupling constants g^V_{LR} and g^V_{RL} couple to the neutrino mass matrix in the Dirac neutrino case. The current neutrino mass constraints, coupled with the assumptions, are expected to produce values for $g^V_{LR,RL}$ on the order of parts in 10^{-6}; several orders of magnitude below the current experimental sensitivity. The neutrino mass do not constrain the values of $g^{S,T}_{LR,RL}$.

2.2 Rare Modes of Muon Decay

The standard model is constructed with an implicit lepton flavour symmetry. The requirement for this symmetry is entirely based on observation, and any observation of a lepton flavour violating process will represent new physics outside of the SM. Searches for flavour violating processes, the simplest being $\mu \to e\gamma$, have been conducted since the muon was first identified as a lepton. Important previous limits are summarized in Table 2.1. The limits pertinent to this measurement are those of $\mu \to eX^0$ where X^0 is a unknown neutral boson of unknown mass. Other measurements are out of the reach of the TWIST detector either because of its limited acceptance, such as the case of a $\mu^+ \to e^+e^+e^-$ measurement, or because the detector system is not equipped to handle the measurement, such as for a $\mu^+ \to e^+\gamma$ measurement.

As demonstrated by Nambu and Goldstone, the breaking of a symmetry in vacuum will produce a boson. If the lepton flavour symmetry is global, then this particle will have no mass and will be observed as a mono-energetic signal of excess positrons at the endpoint of the TWIST positron spectrum. If the symmetry is instead local, then the outgoing boson will be massive, and a positron peak will appear away from the endpoint. To consider both local cases a search will be conducted at all accessible momenta through the TWIST decay spectrum.

A special class of Nambu-Goldstone bosons can arise in minimal super-symmetric

Decay process	Upper Limit	Conf. level	Ref.
$\mu \to e\gamma$	1.2×10^{-11}	90 %	Brooks, 1999[20]
$\mu^- \to e^- e^+ e^+$	1.0×10^{-12}	90 %	Bellgardt, 1987[21]
$\mu^+ \to e^+ X^0$	3.4×10^{-4}	90 %	Bryman, 1986 [22]
$\mu^+ \to e^+ X^0$	2.6×10^{-6}	90 %	Jodidio, 1986 [23]
$\mu^+ \to e^+ X^0, X^0 \to e^+ e^-$	1×10^{-10}	90%	Eichler, 1986 [24]

Table 2.1: Previous published limits on the presence of rare decay processes.

extensions of the standard model (MSSM) where there is a spontaneous violation of the R-parity. The breaking of the Lepton number symmetry which results produces Majorons (J) by the process $l_j \to l_i J$ is enhanced by the R-parity violation process. For muon decay, surplus positrons will occur with a distribution

$$\frac{\partial\Gamma(\mu^+ \to e^+ J)}{\partial\cos\theta} \propto \frac{m_\mu^2}{64\pi}\left[1 \pm P_\mu \cos\theta\right] \tag{2.28}$$

when terms of order m_e^2 and higher are ignored [25]. Indirect limits have been set on such a process as enumerated by Hirsch et al. A limit of $\mathcal{B}(\mu \to eJ) < 0.0011$ has been set based on limits on Majoron production in the pion decay $\pi \to e\nu J$. A direct limit can be set in using the TWIST decay positron spectrum explicitly because of its high angular acceptance.

Chapter 3

TWIST apparatus

The TWIST experiment uses a high precision, low mass detector system to characterize the decay of polarized muons. The beam line used by the TWIST experiment to provide the muons will be discussed here. The record of an event in the TWIST detector is started when a muon passes through a scintillation detector. The muons then enter a symmetrical stack of parallel plane drift chambers immersed in a 2 Tesla magnetic field to determine the momenta and decay angles of positrons generated by muon decay. The magnetic field was mapped to minimize systematic effects in the measurement of the positron tracks.

The following sections will describe the significant portions of the apparatus for the purpose of this measurement. The beam line used by TWIST will be described in some detail, followed by a description of the detector apparatus, and the results of the field mapping.

3.1 M13 beam line

A source of highly polarized muons is required for a muon decay experiment testing the V-A interaction. The M13 secondary beam line at TRIUMF, shown in Fig. 3.1, provides the muon source for the TWIST experiment. For this beam line a graphite production target is exposed to 500 MeV protons in the 1A primary beam line. Pions are produced throughout the production target from interactions between the protons and the carbon atoms. The pions quickly decay into muons. Pion decays on the surface of the production target generate the high helicity muons required by the TWIST experiment. The protons are produced in bunches every 43 ns. A

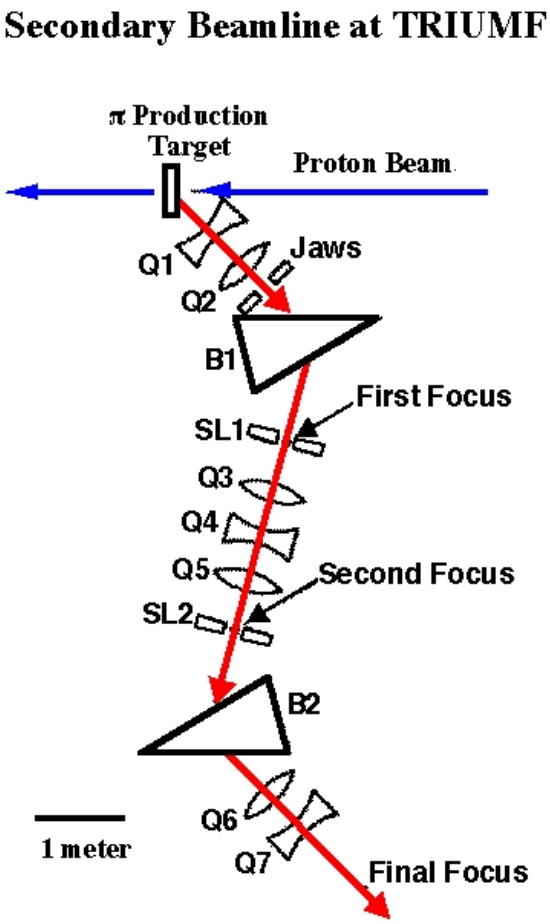

Figure 3.1: The M13 beam line.

time structure in the muon rate the repeats with the proton pulse rate. The time structure is dominated by the pion decay time distribution. Muons are also generated from pion decays within the production target, which will have a lower momentum than the surface muons, from pions that leave the production target and decay near the target — which are referred to as cloud muons, and from pions that decay to muons within the M13 channel. Muons that come from inside the target are removed by the momentum selection. The cloud muons appear in the detector immediately after the arrival of the proton at the production target. After a short time the free pions drift away from the entrance of the channel and the cloud muons no longer accepted by M13. As a result the cloud muons arrive in coincidence with the early

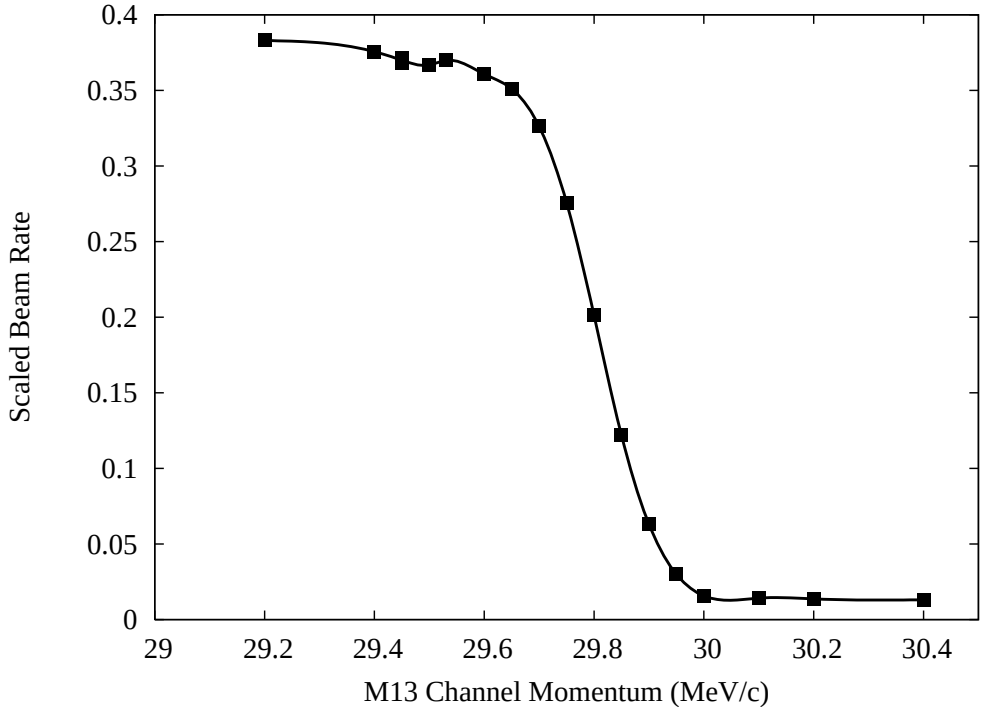

Figure 3.2: A momentum edge scan of the M13 beam line.

surface muons and quickly disappear from the signal. These muons can be removed from the analysis with consideration of the time structure. The majority of pions that enter the channel will decay before they reach the detector.

The M13 beam line is designed to select and focus muons at a particular momentum. The momentum selection is accomplished through the use of a matched pair of magnetic dipoles; the first to separate the beam momenta, and the second to remove the focusing aberration created by the first. Seven sets of quadrupole magnets along the beam line focus the beam at a spot immediately before it enters the M13 experimental area. Positive muons are selected by the polarity of the magnets in the beam line; the negative muons are removed from the beam at the first bend. A set of slits and jaws before and after the first dipole magnet controls the momentum bite selected by the beam line, as well as the muon rate and position of the final focus of the beam. The currents of the magnets in the beam line and the positions of the slits and jaws were all controlled by the experimenters using the EPICS (Experimental Physics and Industrial Control Software) package.

During the nominal data collection, a muon momentum of 29.6 MeV/c was selected. This ensured that surface muons are primarily selected by the beam line, as

muons generated inside the production target will have a lower momentum than the pion decay peak due to material interactions. The typical range of momenta selected, or momentum bite, was 3% of the selected momentum. The beamline momentum was tuned by locating the momentum edge of the muon production peak. This calibration involved sweeping through various settings of the B1 dipole magnets and determining the muon production rate for that setting. A scan of the momentum edge is shown in Fig. 3.2. The decay rate decreases to half of its maximum at a momentum of 29.8 MeV/c; the momentum of muons generated from pions at rest. The momentum of 29.6 MeV/c is achieved by setting the currents of the dipole magnets to values relative to the 29.8 MeV/c momentum edge. These settings are maintained using a current regulator in association with an NMR probe located at the B1 magnetic dipole. This software regulator served to keep the fields in the magnetic dipoles stable to within 0.05 Gauss; a fractional stability of 5×10^{-5}.

The nominal muon beam was tuned to minimize the transverse momentum of the beam when it is introduced on the detector axis to minimize the depolarization of the muon beam as it entered the TWIST solenoid field. A pair of low mass, removable, time expansion chambers (TEC) [26] was periodically introduced into the muon beam to monitor its position and angle in the horizontal and vertical directions before entering the detector solenoid. From studies of the muon beam using the TEC, it is known that the basic elements of the beam line are insufficient in the presence of the TWIST solenoid field to simultaneously adjust both the beam transverse momentum and the distance of the beam spot from the detector axis [27]. Additional current sources were added to the last four quadrupole magnets to provide asymmetric horizontal and vertical steering in these beam elements.

3.2 TWIST Spectrometer

The TWIST spectrometer, shown in Fig.3.3, consisted of a stack of 44 planar drift chambers and 12 planar multiwire proportional chambers as shown in Fig.3.4. A detailed description of the detector construction was published by the TWIST group in 2004 [28]. This detector design was chosen because the geometry allows for a relatively easy energy calibration as the mean energy loss of a particle track passing through the detector with a momentum $\vec{p} = \{p_x, p_y, p_z\}$, is proportional to $|\vec{p}|/p_z = 1/\cos\theta$. Additionally the position of the wires serve as very precise references for the position of any tracks that are passing through the detector. In contrast, an

alternative design choice of a TPC would rely on a very precise calibration of the drift properties of the detector.

The drift chambers were the primary source of the tracking information for particles which pass through the detector, while the proportional chambers were used for timing and event identification. The spectrometer was constructed to be symmetric about a target module which contained a high purity metal foil in the centre to stop the muons. While the beamline defines the z-axis of the experiment, the origin of the TWIST coordinate system is based at the centre of the TWIST spectrometer.

A scintillator system at the upstream end of the detector stack, the M12 scintillation counter, served as a muon event trigger. This counter consisted of a 195 μm thick plastic scintillator adiabatically coupled to two photomultiplier tubes. The linear combination of signals from the two photomultiplier tubes defined the M12 signal. This system was contained in a piece of apparatus, called the upstream beam package (not shown in the figure). A scintillator, called the PU scintillator, was used to count high momentum pions for the purpose of alignment and time calibration runs, and was also located in the upstream beam package. This counter was designed with a hole in the centre so that it would not be in the standard muon beam. A scintillator system, referred to as the DS scintillator, was added at the downstream end to serve

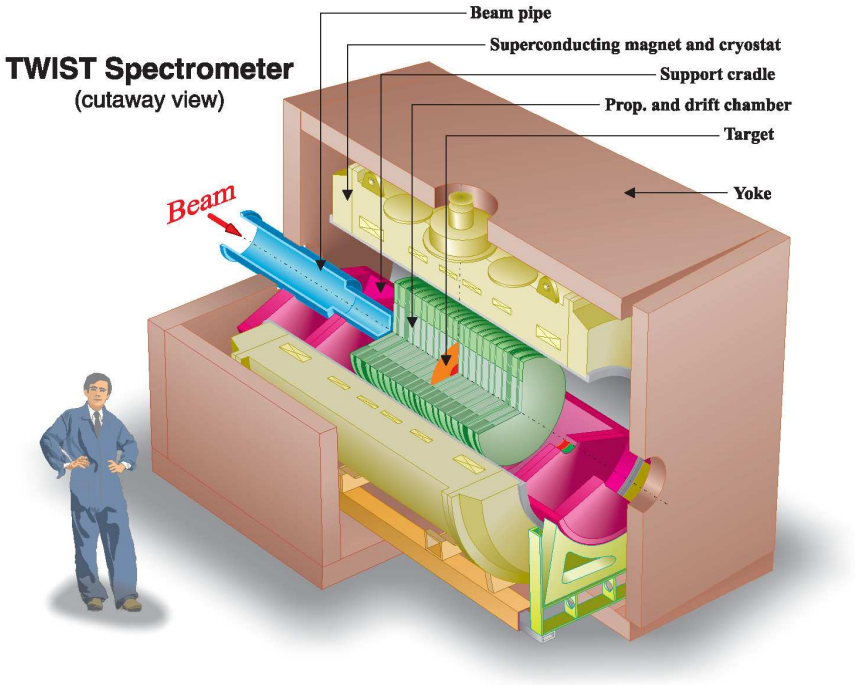

Figure 3.3: A cutaway view of the TWIST spectrometer

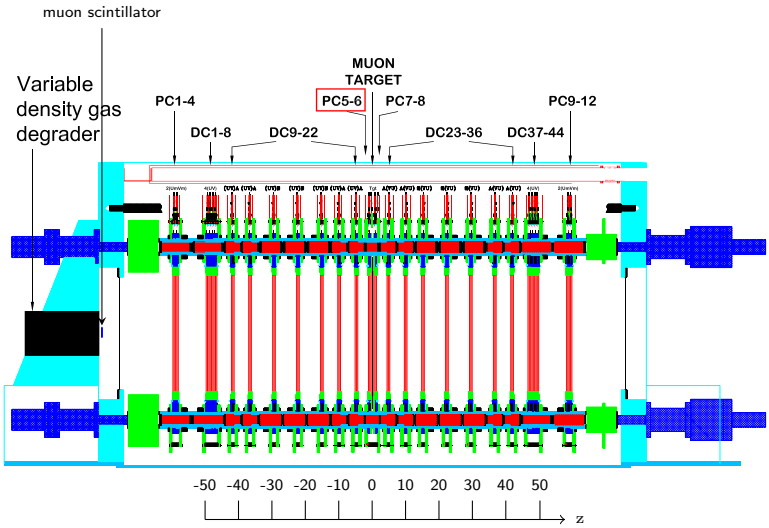

Figure 3.4: A side view of the TWIST spectrometer showing the position of the gas degrader

as a counter for better timing calibrations.

A capacitive probe in the proton beam immediately before the production target detects the proton bursts. The difference between the capacitive probe signal and the M12 signal is interpreted as a time of flight of particles through the M13 beam line, t_{cap}. This is an effective way of identifying surface muons in the muon beam. The width of the M12 pulse could be used to separate muons and beam positrons in the beam. The number of muons collected as a function of the t_{cap} signal is shown in Fig. 3.5. The muons that arrive at the TWIST detector appear with a decay constant defined by the pion decay.

The spectrometer was designed to be as thin as possible in terms of energy loss, both to reduce multiple scattering of decay positrons and to allow the muons to reach the central stopping foil. The total mass of half of the detector must be less than the range of surface muons, $\sim$140 mg/cm^2. To minimize the mass of the detector while maintaining the detector stack at atmospheric pressure, the detector was filled with a Helium/Nitrogen mixture (ratio of $\sim$ 97:3) between the drift and proportional chamber modules. The small concentration of nitrogen was added to prevent HV breakdown on the exterior of the drift chamber modules. A gas control system continuously cycled the gases of the cradle and the wire chambers and maintained the

pressures in the chambers.

Control of the detector mass, and therefore the muon stopping position, is facilitated by a gas volume in front of the detector used to degrade the muon energy. This gas degrader uses a mixture of Helium and CO_2 to control the material in the muon beam. This degrader was used to actively correct the muon stopping position in the detector using a software feedback mechanism. The majority of the muons stop in the metal foil target in the centre of the spectrometer. Because this is not active material, the true stopping distribution cannot the directly observed in data. An example of the simulated distribution is shown in Fig. 3.6. Instead, a mean stopping position was determined from the tails of the stopping distribution based on the last plane hit by the muon before it decays, as shown in Fig.3.7. The mixture in the degrader was altered by the gas system if the difference between the measurement and the preset value exceeded 0.5 mm. This system maintained the centroid of the muon last plane hit position with an accuracy of 0.25 mm of the preset position. Based on simulations,

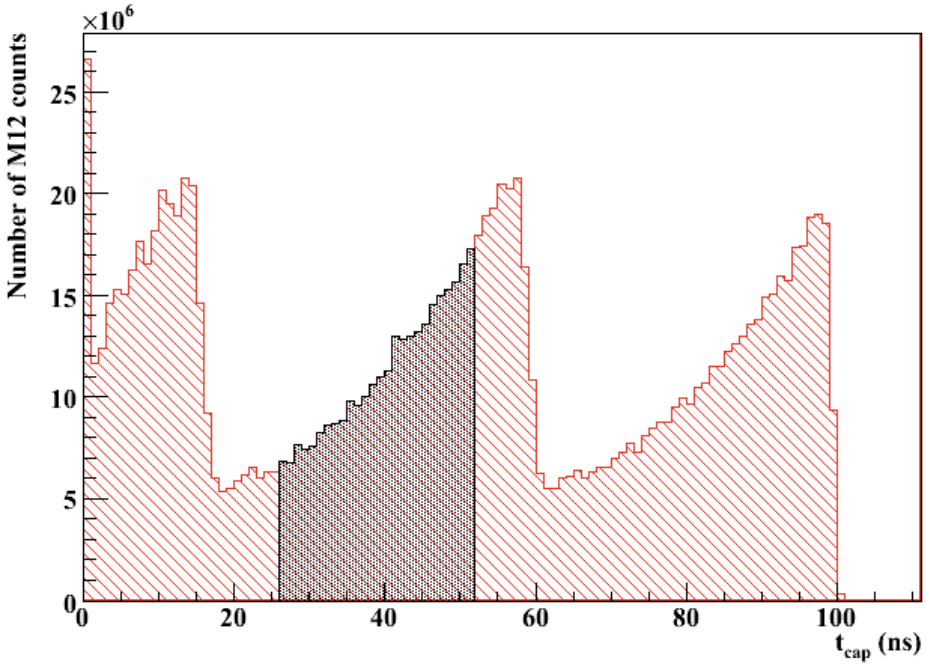

Figure 3.5: The typical time of flight (t_{cap}) distributions of the muons referenced between the M12 scintillation counter and the capacitive probe signal. The surface muons are identified within the shaded region. The time distribution is that of the pion decay in a reversed time scale, repeating with the 43 ns period of the TRIUMF cyclotron proton bursts.

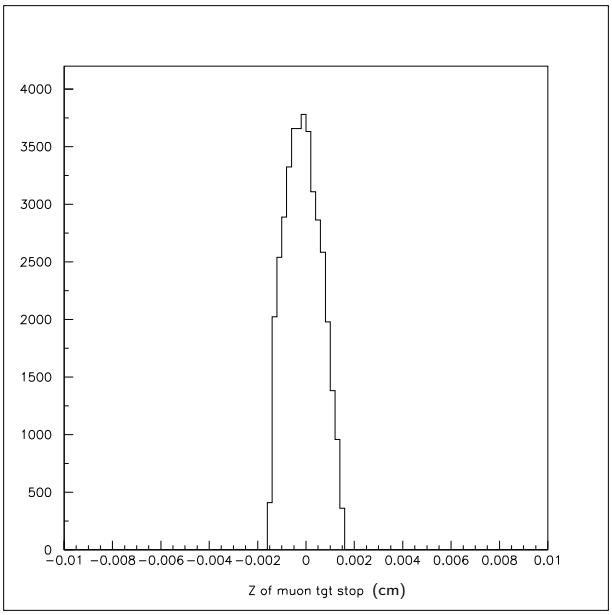

Figure 3.6: The simulated distribution of muons stopping within the target foil. The position is relative to the middle of the target foil.

the mean of the true muon stopping distribution was centred in the muon stopping target when the mean muon last hit position was 6.5 mm upstream of the stopping target. With this regulation of the tails in the muon stopping position in the detector, it is believed that the true stopping distribution is exceptionally stable.

A film degrader was also included in the detector system to make large changes in the muon stopping position. The film degrader was a series of Mylar films of various thicknesses mounted on a roll of acetate plastic. In the nominal setup the muon beam passed through an empty hole in this degrader

3.2.1 TWIST Coordinate System

The spectrometer is oriented along a three dimensional coordinate system where the beam line is defined to be the Z-axis of the system with an origin at the centre of the TWIST spectrometer. Mutually perpendicular U and V directions are defined at -45° and $+45^\circ$ from vertical when one views the detector in the muon beam direction as in Fig.3.8. The wires of each plane are strung to define a U or V position, while the position of the plane in the stack defines the z position of the wire hit. This choice of coordinates was made to keep the readout electronics for both coordinate

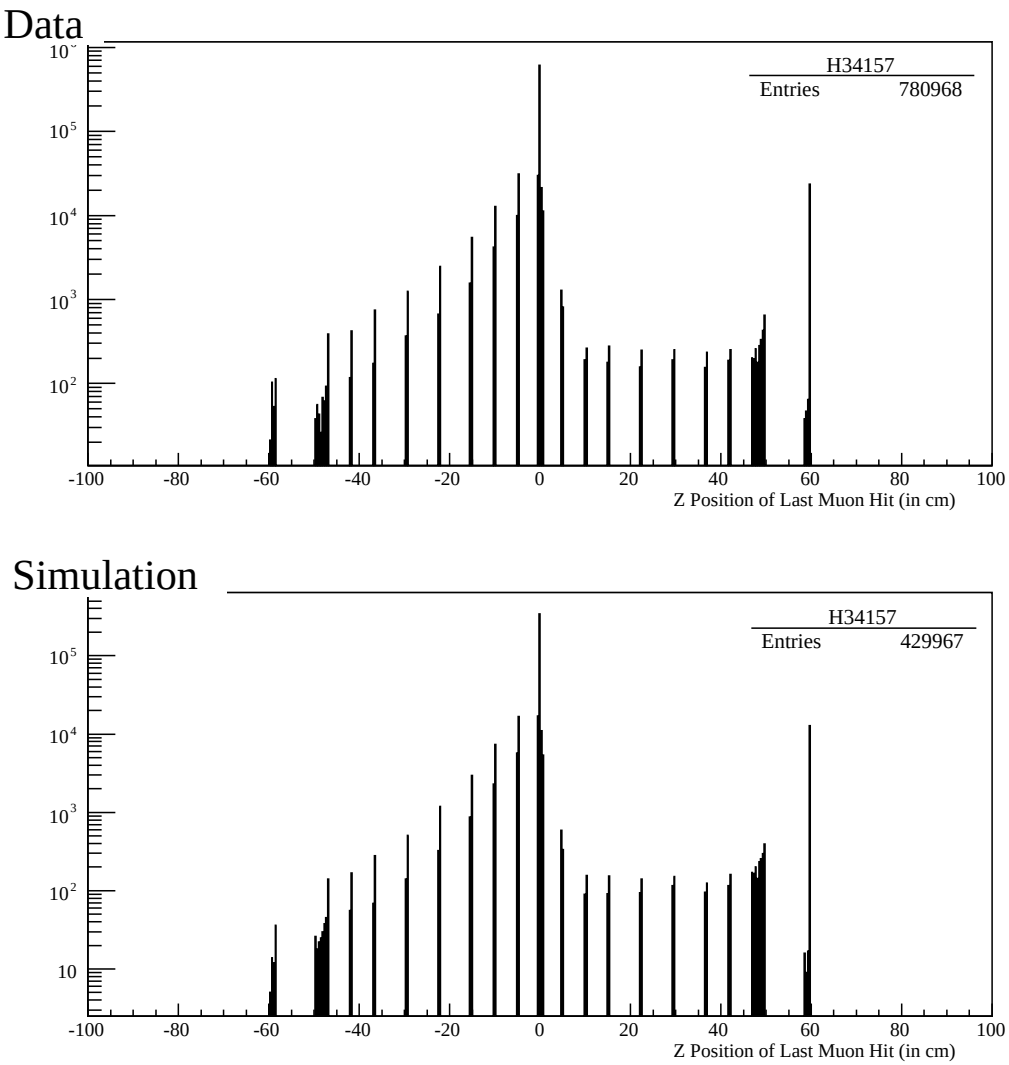

Figure 3.7: The position of the last plane hit by the muon before it decays in both data and simulation. Only the muons that stop within ± 10 cm of the detector centre are used to determine the centroid of the stopping distribution.

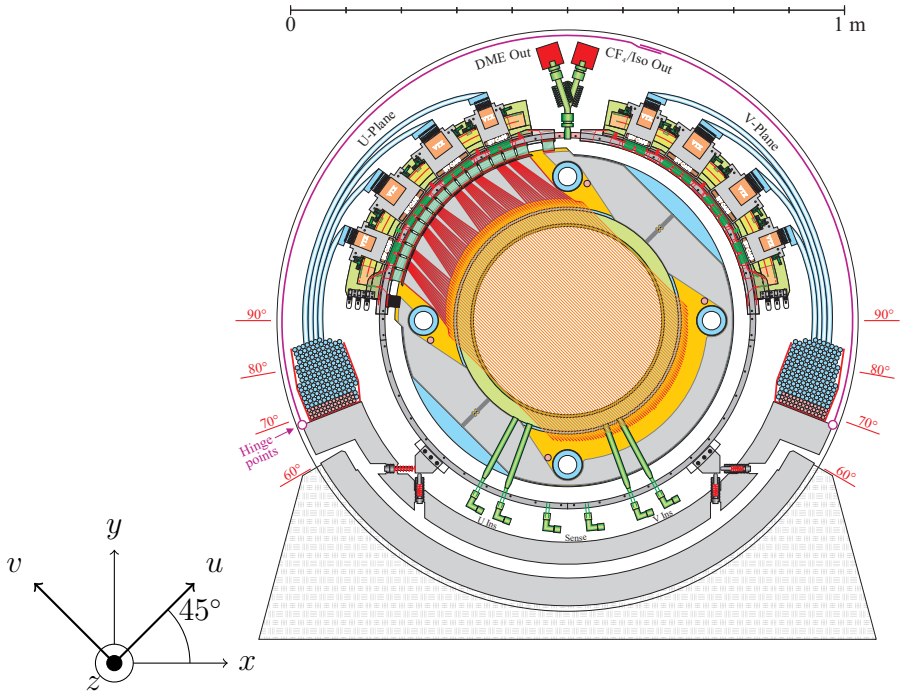

Figure 3.8: A cut away view of the TWIST detector, viewing along the z axis. Coordinate axes of the TWIST detector as viewed from the perspective of the muon beam is supplied. The z-axis points out of the picture.

plane free of the cradle and to avoid an asymmetric sag in the wires due to gravity.

A consequence of this choice of coordinates in the detector is that the reconstructed angle of the positron track, θ, has the opposite definition to that used in the theory. The theoretical definition of θ is the polar angle between the positron direction and the muon polarization vector. However, with this detector system, the muon polarization of positive muons is in the $-z$ direction. The expected muon spectrum has a preferentially backward asymmetry relative to the detector coordinates.

3.2.2 Drift Chambers

The drift chambers were designed to facilitate accurate measurements of the distance between the particle path and the wire. The design effort was lead by Henderson and Selivanov as described in [28]. Each chamber is composed of two aluminized Mylar foils separated by 4.0 mm which serve as cathodes for the drift planes and 80 anode wires strung with a 4 mm pitch, as shown in Fig 3.9. The anode wires are gold plated tungsten/rhenium wires, 15 microns in diameter. The wires were strung under

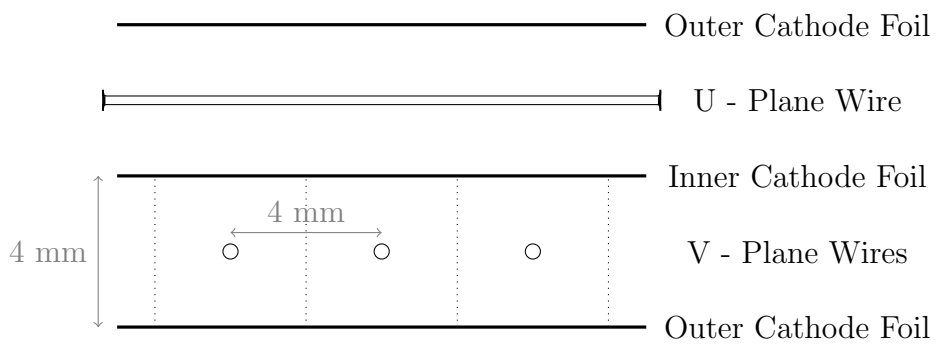

Figure 3.9: A cross section of a paired drift chamber model (to scale).

the tension produced using 30 g weights with a precision in position of 3.3 microns. The tension used to string these planes exceeds the 4 g tension required to keep the wires electrostatically stable under the 2000 V potential used in the drift chambers during operation. Two guard wires are strung on either side of the plane to prevent sparking. Dimethyl ether (DME) was chosen for the drift gas because of its slow drift velocity and small Lorentz angle. The longest drift times expected from the edges of the drift cell can be up to 260 ns. This long drift time gives the TWIST spectrometer an excellent spatial resolution, which is determined by the diffusion characteristics of the drift gas, the ion cluster spacing and the electronics time resolution.

The cathode foils were stretched to a tension greater than 200 N/m so that the planes would remain flat during the chamber operation. Small bulges in the cathode foils of approximately 100 μm were observed during data collection. These distortions in the drift chambers should be absorbed by empirical corrections made to the space time relationships (STRs) defined for the chambers.

The drift chambers are constructed as multi layer modules organized in dense and sparse stacks of planes. Each of these modules is built in layers, starting with an annular glass (FR4) plate with an inner diameter of 39.7 cm and an outer diameter of 60 cm, to serve as a support structure for the gas chambers, the cathode foils and wire planes of the drift chambers and a second glass plate to serve as a lid for the module. A curved glass wall encloses the module.

All of the chamber electronics are fed through this wall using a printed circuit board (PCB) before connecting to the detector preamplifiers. For each of the DC planes the signals from the 80 sense wires are transferred to two 24 channel and two 16 channel preamplifiers that are mounted outside of the chamber walls. The raw signals are carried from the preamps to the post amplifier and discriminator electronics via

9.5 m of coaxial cables. The discriminator electronics produce differential ECL logic outputs representing the time of the chamber wire voltages over threshold. In general this threshold was set to 150 mV. The ECL logic signals are sent to LeCroy 1877s time-to-digital converters (TDCs) which digitize the signals as times relative to the M12 trigger.

Precisely machined Sitall ceramic spacers are used to define the position of each wire plane and cathode foil to a fractional precision of 3×10^{-5}. The Sitall ceramic material was chosen for its small thermal expansion coefficient of $\sim 10^{-7}(dL/L)/C^{\circ}$. The sparse stack consists of seven modules made up of UV plane pairs, distributed in an aperiodic pattern along the z-axis of the detector to establish the momentum of particle tracks along the detector length. The dense stack consists of a single module of eight drift planes, in a VUVUUVUV pattern at either end of the DC tracking volume. The order of the plane orientations is designed to reduce tracking ambiguities.

3.2.3 Proportional Chambers

The proportional chambers (PCs) were designed to produce a fast response to the passage of ionizing particles. The PCs use a fast gas, CF_4/isobutane, as their tracking medium, and are constructed with wires at a 2 mm pitch to decrease the drift time relative to the DCs. Their construction is otherwise identical to the DC planes. A cross section of a PC plane is shown in Fig. 3.10. A module of four PC planes appear at the far upstream (PCs 1-4) and at the far downstream (9-12) ends of the detector. These PCs provide timing information that is used to group events into timing windows as a first step in event recognition [29]. These PC planes consist of 160 instrumented wires with three guard wires on each side of the plane. The active area for this setup then has a 320 mm diameter.

The PCs use the same PCBs as the DC planes to feed the wire signals into the outside electronics. A total of 64 channels are used to handle the 160 sense wires, using four 16-channel preamps. The central 32 wires are read out individually while the wires away from the centre were read out in groups of four to reduce the number of output channels [28].

Four PC planes appear in the centre of the detector (5-8) surrounding the stopping target as part of the target module. These planes serve the dual purpose of providing timing information for the particles in the event and a method to identify muon events

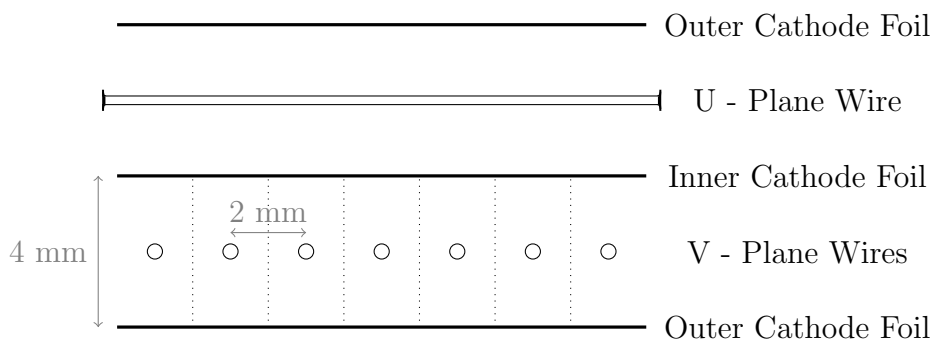

Figure 3.10: U-V pair of projection chambers used in the TWIST detector.

that stop in the PC gas; muons that produce signals in PC 7 or PC 8 did not stop in the target and the pulse height information from PC 5 and 6 can be used to identify stops in the PC gas. Muons that stop in PC 6 will deposit more energy in PC 5 than PC 6. Muons that pass through both PCs will deposit the same energy in both chambers. Muons that decay in the PC gas will experience more depolarization than in the target material which will affect the measured decay asymmetry. A sample of the muon pulse heights in PC 5 versus PC 6 are shown in Fig. 3.11. The cuts shown were chosen to optimize the asymmetry measured from the decay positron which is proportional to the muon polarization.

To facilitate this measurement a lowered voltage was used in PC 5 and PC 6 relative to the other PCs. In general the PC voltages are set to 2050 V to run the gas chambers in a saturation mode so the pulse heights for muons are not strictly proportional to the energy loss. To measure the pulse heights properly, the voltages in PC 5 and PC 6 were dropped to 1600 V.

3.2.4 The Target Modules

The target module was changed twice during the 2006 and 2007 running periods. Each of these three target modules used a different stopping target constructed with one of two different stopping materials. During the fall of 2006 a high purity silver target foil was used in the assembly. This target was exchanged in the winter of 2007 with a high purity aluminum target. Data was collected with the aluminum stopping target through the spring of 2007. A specialized target module using an aluminum target foil with a much larger than normal surface area and no PC chambers was installed in the summer of 2007. The purpose of the these various target modules was to test

the muon depolarization systematics and the positron interaction systematic using different target materials. The last target module, which used the large aluminum foil, could only be used for positron interaction tests because of the removal of the target PCs.

The structure of the standard target modules are very different from any other modules in the TWIST spectrometer. These modules were fabricated as four PC chambers in a UVUV configuration. The centre most cathode foil was replaced with a Mylar annulus with an outer radius of 33.8 cm and an inner diameter of 12.0 cm supporting a circular piece of high purity (99.999%) aluminum or silver foil, 150 mm in diameter. The foil target is glued to the aluminized Mylar foil using a conductive silver epoxy with a 15 mm overlap. A 25 μm mask with a 110 mm diameter central cutout was inserted into the adjacent wire planes so that the gas gain is maintained for the target foil well inside the glue region. Only 48 wires were instrumented in the

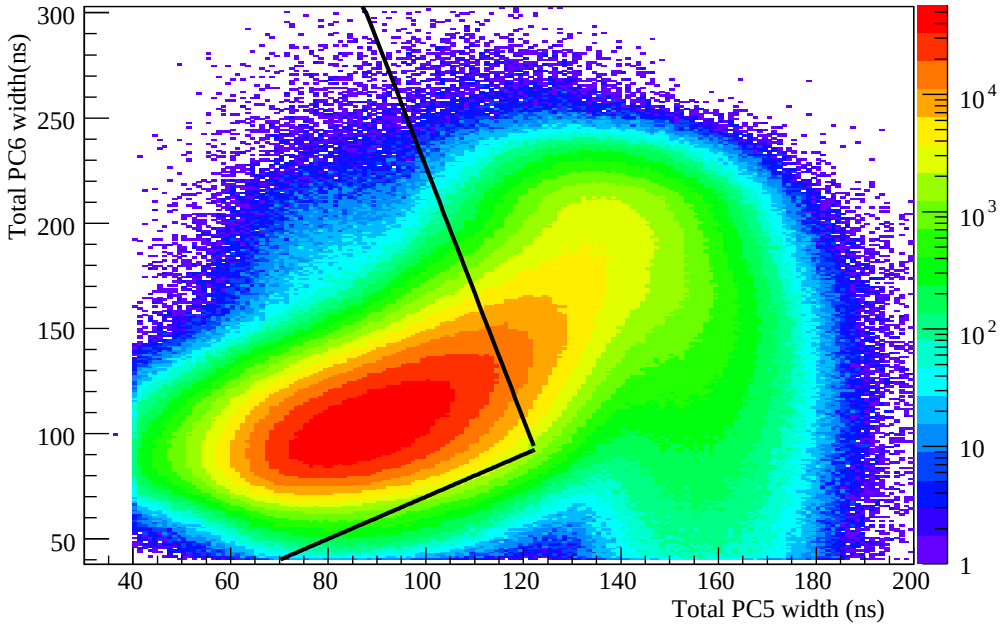

Figure 3.11: Muon pulse widths from PC6 versus PC5 when there are single hits in both PCs. The vertical scale shows the number of muon tracks with a width contained by a 1 ns by 1 ns bin. These widths are proportional to the energy lost in the PC. The location of events in this graph is a measure of the stopping position of muons within the chambers. The black lines show the position of the cuts applied on these pulse widths.

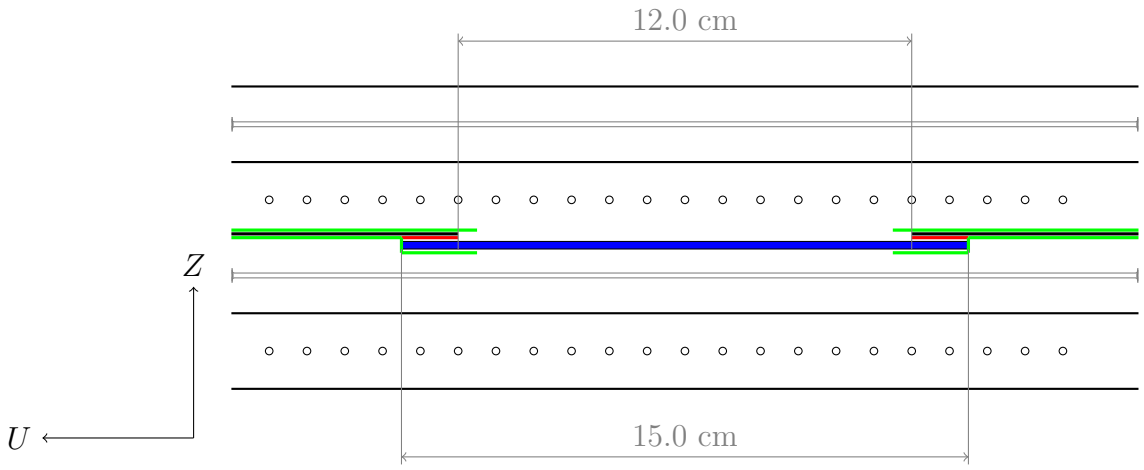

Figure 3.12: Standard target module construction. Metal target foil is shown in blue; epoxy is shown in black; aluminized Mylar is shown in red; and the kapton mask is shown in green. The target assembly acts as the central cathode foil for the two neighbouring PC planes. The surrounding chambers were not drawn to scale. Refer to Fig. 3.10 for the true wire and cathode plane spacings for the PCs.

target PC chambers, thus the active region of the target PCs is only 96 mm wide.

The target thicknesses were chosen so that muons lose approximately the same momentum for both the silver and aluminum targets. The masses of these targets were measured after the detector was decommissioned to produce precise measurements of the target thickness. The thickness of the aluminum target was 71.6±0.5 μm, while the silver target was 30.9±0.6 μm thick.

The large target module was produced purely for systematic studies. The same Sitall spacers and gas box components were used for the production of this target module as for the production of the standard target module. However, all of the PC plane components — the cathode foils and the chamber wires — were left out of its construction. A large disk of aluminum, 76 μm thick, and 300 mm in diameter was mounted on a 23 μm thick Mylar annulus with an inner diameter of 280 mm. The lack of PCs in the target module meant that there was no muon stopping position veto counter, rendering this target geometry of little use for the collection of physics data.

3.3 Magnetic Field

During the standard data collection the magnetic field was held at a constant and nearly uniform 2 Tesla. Two data sets were collected with altered magnetic fields at 2.04 Tesla and 1.96 Tesla to measure muon polarization systematics. The systematics of the momentum scale will depend on the calibration of the magnetic field used in the analysis to the real magnetic field.

The magnetic field is uniform inside the tracking region to the level of 4 Gauss out of 2 Tesla. Non-uniformities on this order will create effects that are visible in the analysis of the data. A model of the magnetic field was developed for the purpose of simulation and analysis. The model of the field was tested using measurements conducted with NMR and Hall Field probes. Empirical corrections and systematic uncertainties were defined for the magnetic field using these measurements.

3.3.1 Field Modelling

The model of the magnetic field was obtained using the OPERA field mapping package. The field maps were constructed using a model of the solenoid coils that matches the design specifications of the TWIST magnet. The current carrying elements of the detector itself were not part of the model. The elements of the magnet were adjusted to account for upstream-downstream asymmetry in the measured field map and a difference in the field gradient between the measured field map and the simulated map. The hysteresis curve of the yoke was scaled by 1.06, and the outer coils were moved toward the centre of the yoke by 0.18 cm to account for these differences. The coils were also shifted in the x-y plane relative to the yoke coordinates.

During standard data collection two NMR probes were placed inside the solenoid bore to continuously monitor the magnitude of the field in the tracking region during data collection. The field map was scaled so that the magnetic field matched the value measured at the NMR probe. The analysis of the 1.96 T and 2.04 T data sets also used the 2.0 T OPERA field map scaled to match the field at the NMR probe position.

3.3.2 Field Measurements

The measurements of the field map were completed in April 2002[30] while the TRIUMF cyclotron was in operation. The data were collected inside the bore of the

solenoid using a radial arm with seven hall probes at regularly spaced positions along its length. The field measurements were taken in runs over ranges along the z axis; ie. 45.0 cm $\leq$ 70.0 cm in 0.5 cm steps; at a series of azimuthal angles between 0° and 180°, covering the active regions of the detector volume. For a subset of these measurement runs taken at the nominal magnetic field of 20 kG a hand held NMR probe was positioned close to one of the Hall probes to allow for a simultaneous measurement of the magnetic field with both probes.

The calibration of the Hall probes was problematic at the required accuracy because they reset each time the probes were turned on. The probes were re-calibrated with the NMR probe using the magnetic field at z = 0 cm before each calibration run. However, the Hall measurements when compared with the NMR measurements at various radii as a function of z still show deviations on the order of up to 2 Gauss.

In principle, differences between a Hall probe measurement and a NMR measurement are expected because a Hall probe, as it was used for this measurement, is only sensitive to the z component of the magnetic field while the NMR probe measures the magnitude of the magnetic field. Studies done using the OPERA simulation package suggest that the radial component of the magnetic field should be small, that is $|\mathbf{B}| - |B_z| \leq 0.001$ G. Because the calibration of the Hall probes was questionable, it was considered necessary to estimate the systematic difference between the OPERA modelled field map and the real field measurements. As a result a much smaller set of measurements are available to map the magnetic field and only for the 2.0 T field. Field maps were compiled for the 2.04 T and 1.96 T magnetic fields, but no NMR mapping measurements were taken for these fields.

Empirical corrections were made to the magnetic field maps using the measurements of the solenoid field. These corrections were made as functions cylindrical coordinates relative to the detector axis, and took the form,

$$\delta B_z = C_2 z^2 + C_3 z^3 + C_r r \tag{3.1}$$

to correct the z-component of the magnetic field. The differences with respect to the azimuth were considered negligible. To preserve the magnetic field divergence condition of Maxwell's equations, $\nabla \cdot \mathbf{B} = 0$, a correction to the transverse magnetic field is also applied.

$$\delta B_r = -C_2 z r - \frac{3}{2} C_3 z^2 r \tag{3.2}$$

where C_2, C_3, and C_r, are the empirically measured coefficients defining the difference

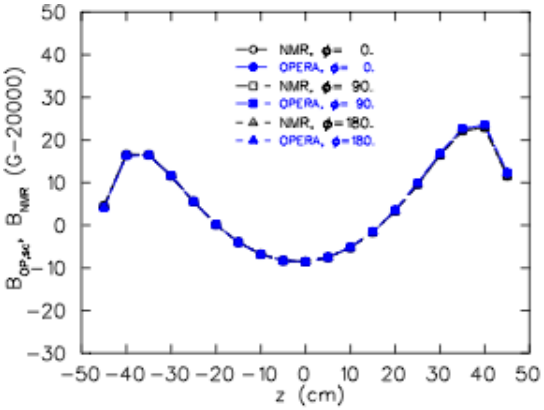

a) Measurements at $r = 0$ cm

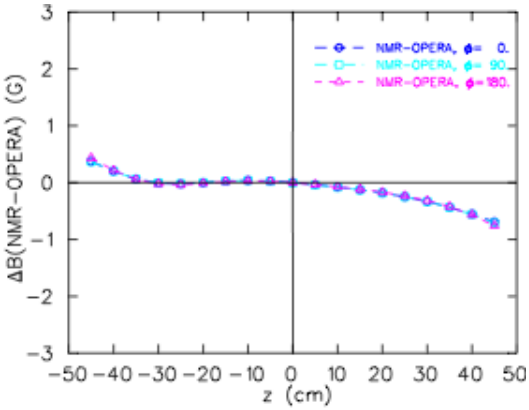

b) Differences at $r = 0$ cm

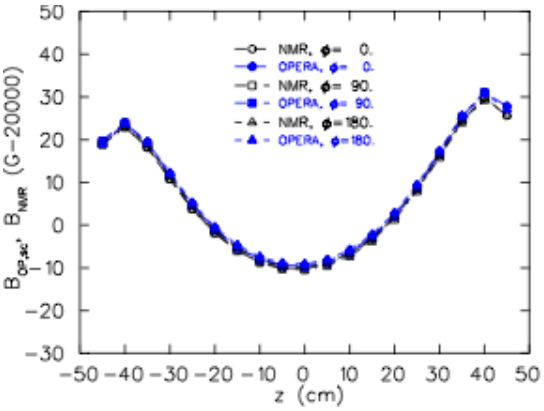

c) Measurements at $r = 8.255$ cm

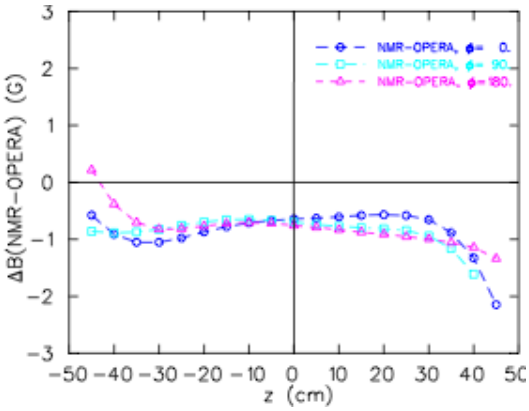

d) Differences at $r = 8.255$ cm

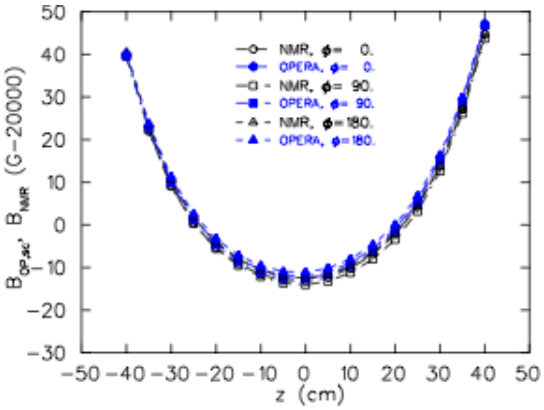

e) Measurements at $r = 16.51$ cm

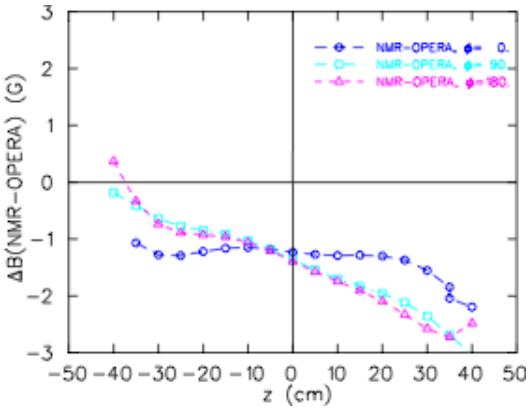

f) Differences at $r = 16.51$ cm

Figure 3.13: Comparison between NMR maps and the OPERA modelled field maps at three different radii and three different angles.

between the measured magnetic field and the OPERA magnetic field. Comparison of these measurements to the OPERA field map show that the opera field map is accurate on the level of 0.5 Gauss; a fractional error of 2.5 parts in 10^5 [31] which translates directly to any momentum measurements completed using this magnetic field. Since it is the component of the magnetic field perpendicular to the momentum of the charged particles that is most important for the reconstruction of their paths, it is important to make these corrections as precise as possible.

Chapter 4

Data Collection and Analysis

A large set of data was collected for the TWIST analysis to achieve its precision goals of an order of magnitude improvement over previous results. A robust analysis was required to extract the momenta and angles of the decay positrons without compromising the gains made by high statistics by increasing the systematic uncertainties. The analysis was completed by way of a multi-stage analysis comparing the data directly to a simulation of muon decays in the TWIST detector. A schematic of the TWIST analysis procedure is shown in Fig. 4.1. This chapter focuses on the data and its analysis.

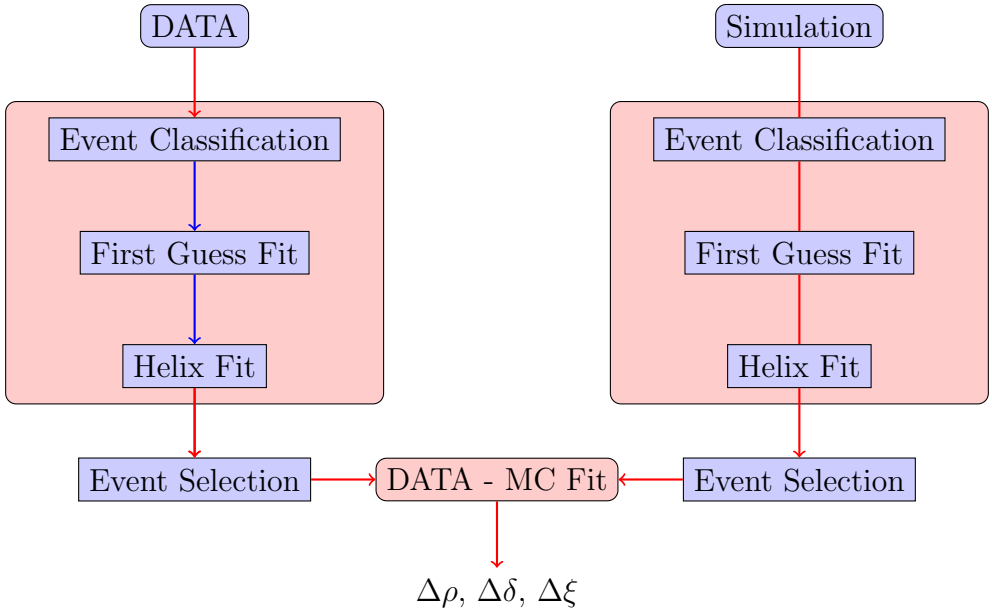

Figure 4.1: A schematic of the TWIST analysis procedures

Set Number	Good runs	Target Material	Description
68	619	Silver	Nominal settings
70	855	Silver	B=1.96 T
71	771	Silver	B=2.04 T
72	979	Silver	TEC in data set
74	549	Silver	Nominal settings
75	838	Silver	Nominal settings
76	689	Silver	Mis-steered data set
83	974	Aluminum	Nominal with downstream beam package
84	874	Aluminum	Nominal without downstream beam package
86	1192	Aluminum	Mis-steered
87	908	Aluminum	Nominal settings
91	241	Aluminum	Low Momentum
92	316	Aluminum	Low Momentum
93	533	Aluminum	Low Momentum

Table 4.1: A summary of the data sets collected for the purpose of the determination of the decay parameters. The three low momentum data sets were taken with slightly different beam line settings.

4.1 Collected Data Sets

TWIST collected in excess of 8 billion muon triggered events during 2006 and 2007 using two different stopping targets. These muon triggered events were collected in runs of 200000 MB, which translated to 850000 muon triggers on average. The data were further collected in sets of data runs during which the experimental conditions were held as constant as possible. Some of these data were collected for the purpose of systematic studies, while the majority of data sets were collected with a sufficient quality that they could be used for the physics measurement of the decay parameters. A summary of the data sets that could be used to determine the decay parameters are shown in Table 4.1. All of the data sets listed were ultimately used in the determination of ρ.

4.1.1 Quality of Data checks

The quality of these data was exhaustively reviewed both during collection and after. The data were subject to checks of the muon rate, beam line stability, the gas system stability, temperature changes during collection. These checks were conducted

through the measurement of scaler quantities recorded during data collection.

A number of on-line tests of the data were conducted through an analysis of a subset of the data. During each run, one event in every ten was selected from the complete run. These data were subjected to a short analysis to check the distribution of TDC hits, the mean stopping position of the muon, the momentum distribution of the positrons measured and other quantities considered for the consistency of the data. The mean muon stopping position, derived from the last plane hit by the decay muons, is a special quantity as it is used in the on-line feedback mechanism for the muon gas degrader system. Other quantities were considered by the experimenter to determine if the data collection is proceeding as it should.

After data collection many of these same quantities were used to determine the suitability of the collected runs for the final physics analysis. Runs that significantly deviate from the baseline run time conditions were removed. The assignment of these runs as bad runs were made conservatively as they represent a small subset, roughly 10%, of the total statistics.

4.2 Measurement of Positron Tracks

The positron spectrum is the product of a staged analysis. This analysis is contained within a package largely developed by TWIST collaborators called `MOFIA`. The analysis begins with a classification of a muon triggered event based on the proportional chamber timing. Groups of hits recognized by the event classification as possible tracks are used to calculate the positron momentum and angle using the drift chamber wire positions as a reference. To further refine these estimates each track is fit to a piecewise helical path, allowing for the estimated momentum loss through the detector.

4.2.1 Event Classification

Events are identified based on a muon trigger. This is supplied by a muon scintillator contained in the upstream beam package. The typical muon trigger rate for nominal running conditions was between 3000 and 4000 Hz. After the muon trigger, the DC hits are grouped in time relative to the muon trigger based on the PC firing times. The particle content of these time groupings, called windows, is classified based on various criteria. The TDC pulse widths of the M12 scintillator and the PCs are used

to separate muons from positrons. Positron windows are further separated into beam positron windows, if there are PC hits in both the upstream and downstream ends of the detector, decay positrons, if there are PC hits only on one side of the detector, or delta ray events if there is a decay positron on one side of the target and a small radius track on the opposite side.

A strong limitation on the classification of windows is the reaction time of the PCs. This means that it is impossible to distinguish particle windows separated by less than 100 ns. Similarly the drift time of the DC gas imposes a limit on the minimum time required to separate DC hits between windows.

The events are classified by the windows present in the event. A considerable fraction of events (40%) are composed of a single muon window with a matching decay positron window that are separated by more than the 1050 ns DC overlap time. These are called "simple clean" events. Alternatively an event containing a muon, a decay positron, and a beam positron, all well separated in time are called "time clean" events and constitute a much smaller fraction of events. Other event types can be more complicated involving other window types. A list of the important event types can be found in Table 4.2. A graph showing the number of events for the various window types is shown in Fig. 4.2.

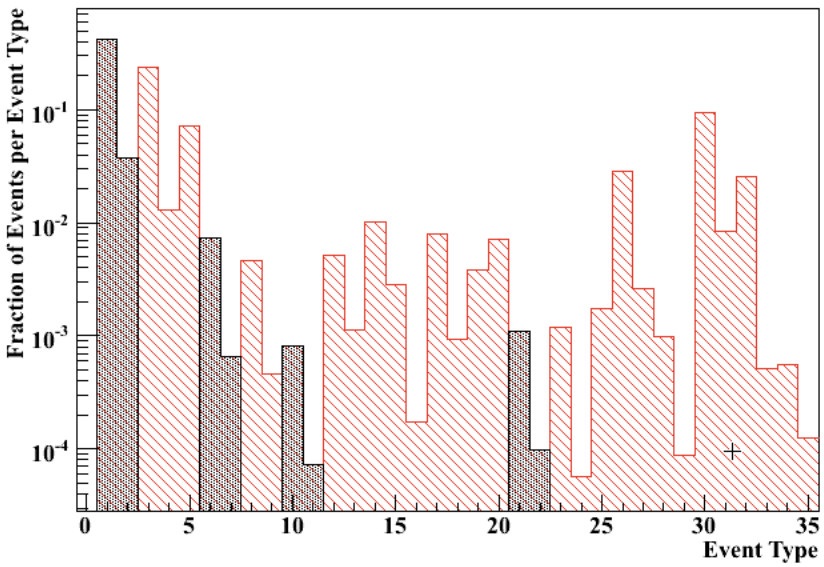

Figure 4.2: Fractional number of events found in each event type for data before event cuts (in red) and after event cuts (in black).

	Event Type	Description	Fraction
1.	Simple, Clean	Muon and decay positron separated by >1050 ns	0.394
2.	Time Clean	Muon, decay positron, and beam positron(s), separated by >1050ns	0.049
3.	Simple DC Overlap	Muon and decay positron separated in time t such that 100 ns $< t <$ 1050 ns.	0.228
4.	Time DC Overlap	Muon, decay positron, and beam positron(s) separated in time t such that 100 ns $< t <$ 1050 ns	0.017
5.	PC Overlap	There is a window with two tracks separated by <100 ns	0.080
6.	Simple Delta Cleaned	Muon, decay positron separated by >1050 ns. Delta ray from positron measured	0.007
7.	Time Delta Cleaned	Muon, decay positron, and beam positron(s), separated by >1050 ns. Delta ray from positron measured	0.0009
10.	Simple Scatter Cleaned	Muon and decay positron are separated by >1050 ns. Positron hits on both sides of muon stop	0.0008
11.	Time Scatter Cleaned	Muon, decay positron, and beam positron(s), separated by >1050ns. Positron hits on both sides of target.	0.00009
21.	Simple Beam Positron Cleaned	Muon and decay positron separated by >1050 ns. Decay positron appears to be within 100 ns of a beam positron.	0.0011
22.	Time Beam Positron Cleaned	Muon, decay positron, and beam positron(s) separated by >1050 ns. Decay positron appears to be within 100 ns of a beam positron	0.0001
26.	Other, Unknown Trigger	Events where the trigger window does not contain a muon or a beam positron	0.011
30.	Simple Clean - too high angle	Simple clean events; the average area of the clustered hits is greater than 12.5 cm and the average hits per plane is greater than 3	0.0939
31.	Time Clean - too high angle	Time clean events; the average area of the clustered hits is greater than 12.5 cm and the average hits per plane is greater than 3	0.0116
	Total Listed Total Accepted		0.894 0.452

Table 4.2: Brief descriptions of the important event types defined in the TWIST analysis. Remaining event types are small contributions to the total number of events and are not considered reliable for the measurement of muon decay events. Numbers shown were taken from set 84.

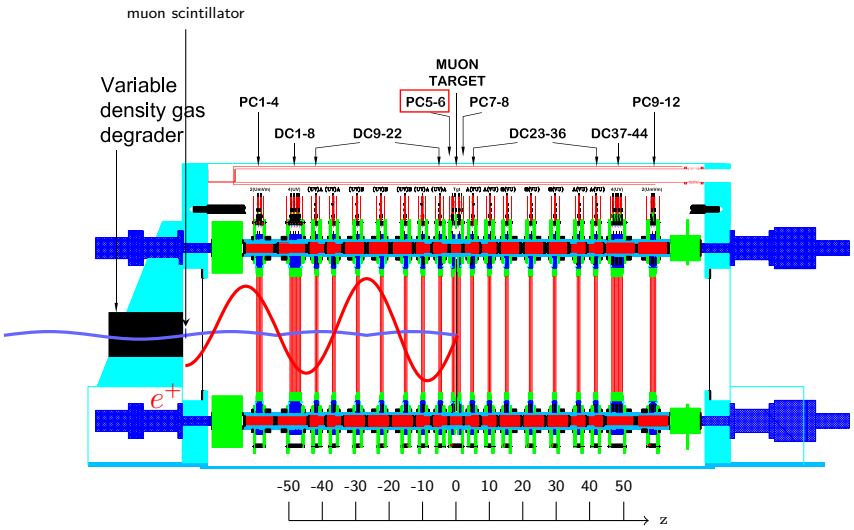

Figure 4.3: An example of a simple upstream decay event.

4.2.2 First Guess

The information from the windows is passed into an intermediate pattern recognition and fitting algorithm called "First-Guess". The wire positions of the DC hits selected by a window are grouped into tracks by finding hits that can be grouped into a circle when projected into the U-V plane. Circles through sets of three successive pairs of u-v hits are tried combinatorially to find the best radius that describes the locus of hits through the drift chambers. The radius of this circle provides an approximate measure of the transverse momentum of the positron track. The pitch of the helical track is found using a combinatorial approach that attempts many different possible pitches to find the one that includes the largest number of DC hits. The flexibility exists in this method to exclude or include particular hits in the windows from the track.

To find the best radius and phase of the potential positron track, a goodness of fit test called a Chebyshev norm is used to compare the positions of the hits on the drift chamber wires to the potential track. If this test fails then it is possible for particular hits to be removed from the track or the track may be broken into two. All of the DC hits used in this procedure as well as the parameters of the estimated positron track are passed to the final stage of the analysis.

4.2.3 Helix Fitting

The final stage of the MOFIA analysis compares the DC hits to a discontinuous helical pathway using a least squares fit. The DC hits passed from the "first guess" algorithm form the data set for the fit while the parameters of the track present a starting point for the fitting procedure. The Helix Fitter tracks the particles between each drift plane hit through the magnetic field map and through the detector material as defined in a pregenerated geometry file.

This fit is completed in two passes. The first uses the wire centre positions of the DC hits as the input data for the helix fits. The second stage uses the DC hit times to produce accurate distances between the ionization site and the drift cell wire. A set of space time relationships (STRs) for the drift cells were calculated using the GARFIELD software package and refined using the data (see Section 4.3.3). The calibrated STRs allow the experiment to accesses the full benefit of the drift chamber resolution. The spatial resolution of the drift cell, σ_{res} varies as a function of the closest distance of approach between the positron hit and the wire. Based on work by Alex Grossheim, the function for the resolution was assumed to be

$$\sigma_{res} = a + b\sinh(q_0 r_{cell}^2), \tag{4.1}$$

where $r_{cell} = \sqrt{u_{cell}^2 + v_{cell}^2}$ is the distance between the position of the hit in the cell, as determined from the STRs and the best match to the measured resolution appears when $a = 120$ μm, $b = 5$ μm, and $q_0 = 100$ cm^{-2}.

A number of corrections are made to the helix path to account for various physical processes that may affect a positron along its path. The first is a correction for multiple scattering processes. This correction takes the form of discontinuities in the helix referred to as kinks. The effective χ^2 of the fit then becomes

$$\chi^2_{HF} = \sum_{i=0}^{N_{hits}} \frac{(y_i - f(\vec{u}_i;\vec{p}))^2}{\sigma^2_{res}} + \sum_{j=0}^{N_{kinks}} \frac{u_j^2}{\sigma_j^2} + \sum_{j=0}^{N_{kinks}} \frac{v_j^2}{\sigma_j^2} \tag{4.2}$$

where y_i is the mean position of the ionization in the DC cells, $f(z_i;\vec{p})$ is the calculated path of the track, u_j is the kink angle in the $v-z$ plane, and v_j is the kink angle in the $u-z$ plane.

The kink resolution is calculated for each track using the Gaussian approximation for the projected angular distribution (see Eq. 27.12 of Ref.[4]). Kinks are located at

the central foil of each UV plane pair in the DC stack and at the midpoint between successive DC modules. No more than 20 kinks are ever allowed for a given track. The kinks are defined so that the total momentum of the track is unchanged.

The kinks are expressed as scattering angles with respect a pair of orthogonal axes. The original implementation by Konstantin Olchanski defined these angles with respect to the U and V axes and added these scattering angles to the positron vector using the direction cosines. Defining these scattering angles using the Euler angle of the positron as a basis vector was suggested to remove a potential bias. If the kinks are added to the tracks as direction cosines then they would introduce weights disproportionate to their size for large kink angles. If the positron track is has a polar angle , θ and an azimuthal angle, ϕ, at the kink plane, the assumed coordinate system uses the following vector basis.

$$\hat{3} = \begin{pmatrix} \cos\phi\sin\theta \\ \sin\phi\sin\theta \\ \cos\theta \end{pmatrix}, \hat{1} \propto \hat{v}\times\hat{3} = \begin{pmatrix} \cos\theta \\ 0 \\ -\sin\theta\cos\phi \end{pmatrix}, \hat{2} = \hat{3}\times\hat{1} \propto \begin{pmatrix} -\sin^2\theta\sin\phi\cos\phi \\ \cos^2\theta + \sin^2\theta\cos^2\phi \\ -\sin\theta\cos\theta\sin\phi \end{pmatrix}. \tag{4.3}$$

After completing the rotation through the (small) scattering angles Δ_1 and Δ_2 about the $\hat{1}$ and $\hat{2}$ axes at a kink, the new unit vector of the positron track becomes,

$$\hat{k} = \sin\Delta_2\hat{1} - \sin\Delta_1\hat{2} + \sqrt{1 - \sin^2\Delta_1 - \sin^2\Delta_2}\hat{3}. \tag{4.4}$$

If the momentum of the track before the kink was $|\vec{p_{tot}}|\hat{3}$, the momentum after the kink becomes $|\vec{p_{tot}}|\hat{k}$

This transformation does not change the measured path of the track compared to the introduction of kinks as direction cosines with respect to U and V. However it does alter the χ^2_{HF} of the track during the fitting procedure. This removes a small number of poorly reconstructed events from the overall analysis due to a sanity check in the fitting code which keeps the effective χ^2 calculated at any point during the fit less than 10000. The net loss is primarily due to events that are poorly reconstructed at the First Guess level.

The positron continuously loses momentum as it passes through the detector. Too little momentum is lost to add this as an additional degree of freedom in the fit, so a correction for the momentum loss is imposed in the Helix Fitter. For a track passing through a material with a thickness Δs and a momentum loss dp/ds, the momentum

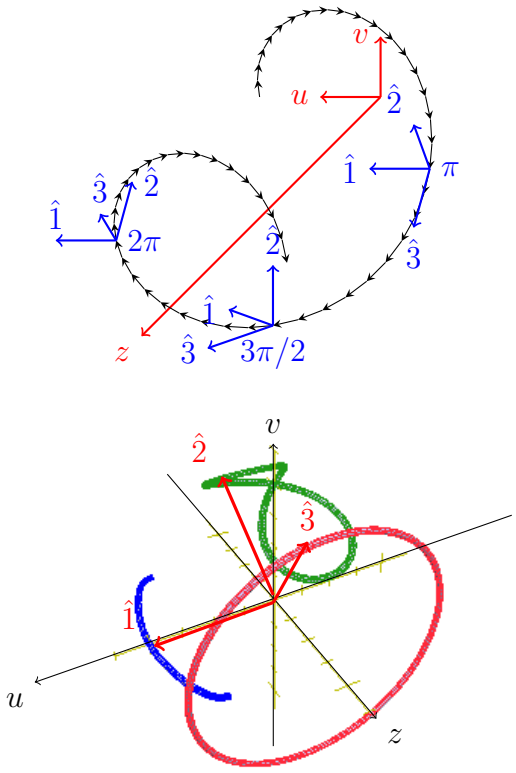

Figure 4.4: The coordinate system defined for the kinks along the positron track. At all times the $\hat{3}$ vector is tangential to the positron path, while the $\hat{1}$ is defined to be mutually perpendicular to the $\hat{v}$ unit vector and the $\hat{3}$ vector. $\hat{2}$ is defined to be mutually perpendicular to $\hat{3}$ and $\hat{1}$. The lower figure shows the paths that the unit vectors trace as the positron progresses through the detector.

of the track after passing through that material over a path length Δs is

$$|\vec{p'}| = |\vec{p}| - \Delta s \frac{dp}{ds} \tag{4.5}$$

The phase of the track after passing through a path length s is $\phi = s \sin\theta / R$. This phase also requires a correction to the phase of the helix as it passes through the detector material.

$$\phi = \frac{\Delta s \sin\theta}{R} \sqrt{1 - \frac{1}{cq|\vec{B}|}\frac{dp}{ds}}. \tag{4.6}$$

The above corrections were applied when tracking positrons through Helium and DME. Momentum loss through the Mylar foils is treated with a different method. Since the cathode foils have a standard thickness, a single energy loss was assumed

for all. An energy loss ΔE_{foil} is subtracted from the fitting track as it passes through the foil;

$$\vec{p'} = \vec{p} - \frac{I_{dir}}{\cos\theta}\Delta E_{foil}\frac{\vec{p}}{|\vec{p}|}. \tag{4.7}$$

The value of I_{dir} is defined to be 1 for downstream going tracks and -1 for upstream going tracks.

Correcting for the momentum loss requires an assumption about the direction of flight of the positron. By default the positron is assumed to travel in the direction away from the target module. The parameters of the helix fitting procedure are the positron momentum vector $\vec{p} = \{p_u, p_v, p_z\}$, at a position in the detector given by $\vec{q} = \{u_0, v_0, z_0\}$. The coordinate z_0 is predefined as 1 cm closer to the target than the closest plane involved in the fit. The helix fitter writes the track information, as well as timing and event classification information, to a tree structure compliant with the ROOT software package.

4.3 Calibrations

4.3.1 Time Zero determination

To use the PC and DC chambers effectively the relative timing of the chamber wires and the scintillators must be determined. This relative timing can be affected by the cable lengths and variations in the electronics, so the timing offsets must be measured during data collection. A method of measuring these timing offsets using the decay positron data was developed to remove systematics due to drift in the timing of the wires. The time zeros were determined separately for each data set.

At each wire, the times between the starting signal (from the muon scintillator) and the arrival of the ionization clusters at the wire appear as a distribution that characterizes the drift of the ions closest to the wire, the number of ions needed to fire the discriminator, the diffusion time of the drift gas, and the time jitter of the electronics. The ion cluster spacing of the gas produces a time variation compared with the drift time from the closest approach of the track to the wire. The behaviour for tracks close to a wire is characterized by a convolution of a nearly instantaneous rise at a time t_0 with an exponential with a parameter λ, that depends on the drift time non-linearity in DME, and a Gaussian peak, with a width, σ, which depends mainly on the ion cluster spacing and electronic jitter. The convolution of these two

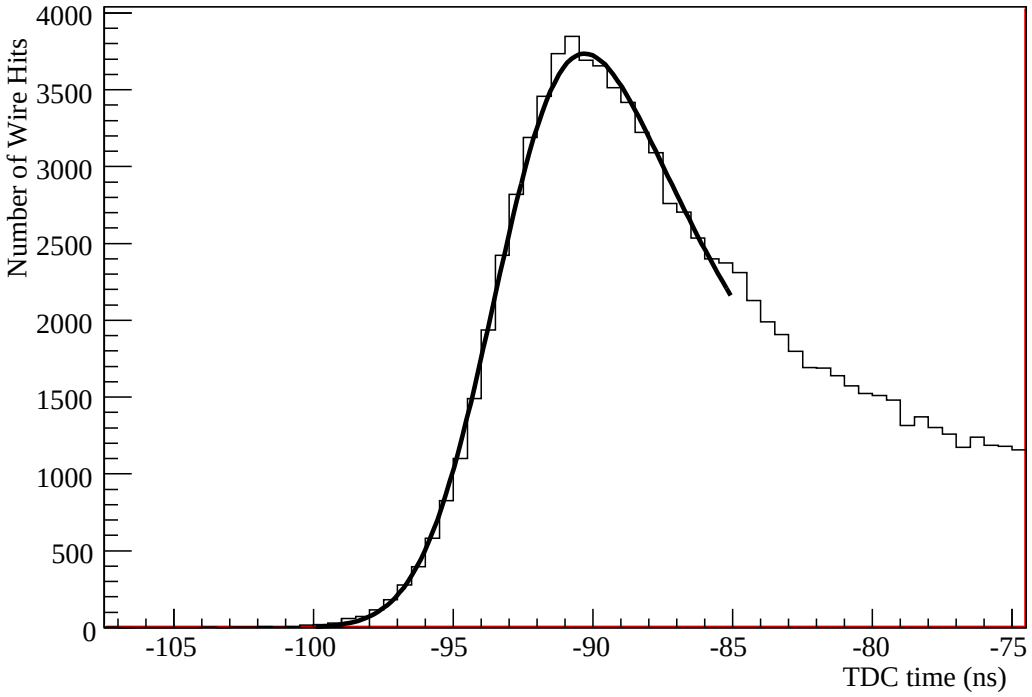

Figure 4.5: TDC time distribution collected by a wire near the middle of DC9. The time zero measured for this wire is -93.06 ns based on the fit of Eq. 4.8 to this distribution.

underlying functional shapes is

$$f(t) = \frac{1}{2} e^{-\lambda(t-t_0-\frac{\lambda\sigma^2}{2})} \left(\mathrm{Erf}\left\{ \frac{t - t_0 - \lambda\sigma^2}{\sqrt{2}\sigma} \right\} + 1 \right). \tag{4.8}$$

This timing of each track was corrected for the time of flight of the positron using an estimate of the angle of the track and assuming that the positron travels at c. In this way the distributions could be integrated over many tracks at a variety of angles without altering the rise time for single tracks. The distribution of charge collected on a single wire is shown in Fig. 4.5.

The results are used to correct the timing of each TDC separately. These corrections are applied to the chamber hit information before the data are used in event classification, when they are first extracted from their files. The time zero corrections for data relative to the PU and DS scintillators are shown in Fig 4.6. The corrections in data show a large amount of structure resulting from variations in the cable

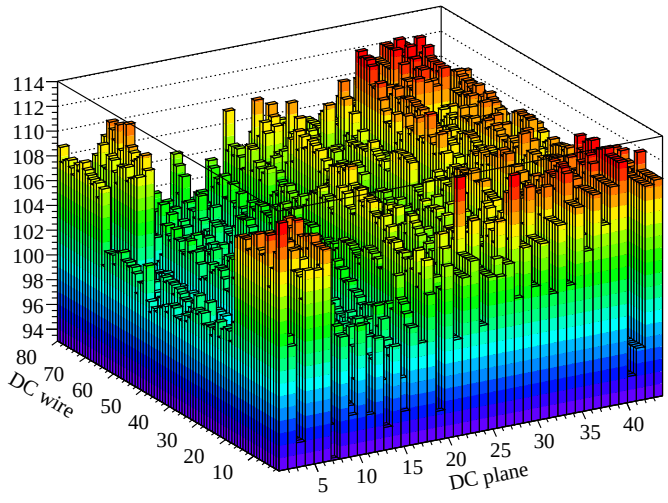

Figure 4.6: Time zeros measured from a nominal data set based on the passage of positrons through the half detector stack from the stopping target. Upstream and downstream positrons use different scintillators for reference times. Some of the structure appears as a result of differences between the reference scintillation triggers. The remaining structure appears as a result of differences in cabling.

lengths, and differences between the geometry of the M12 and downstream scintillators. This structure is mostly absent when this procedure is applied to the Monte Carlo simulation which validates the method, as the simulation is generated with null time zeros.

4.3.2 Alignment

A good alignment of the system is necessary for the proper analysis of the data. The translational positions and the relative rotations of the wire planes must be measured each time the detector is removed from the solenoid. This measurement used a special set of data taken with 120 MeV/c pions and the magnetic field off to produce straight tracks in the detector with a minimum of scattering. Special alignment runs were taken using special collimators at both ends of the yoke to determine the alignment of the detector with the yoke.

These alignments were completed by Anthony Hillairet [32]. The alignment is an iterative process. The pion tracks are fit using straight lines through the detector. The residuals are used to correct the rotation and U-V position each DC plane,

and the fit is repeated. The process converges in 10 iterations or less. The translational alignment of the DC chambers was completed to a precision of 10 μm and the rotational alignments were measured with a precision of 0.002 degrees or 0.03 milliradians.

A further correction was required to match the orientation of the detector as a whole to the magnetic field alignment. This was done by fitting positron tracks in the detector to helices with a z dependence in the position of the centre of the helix. This correction takes the form of shear translations in the u and v positions of the planes. The shear translations of the DC stack with respect to the magnetic field were computed for each data collection period to a precision of 0.03 milliradians.

4.3.3 Space Time Relationships

The space-time relationships (STRs) derived for the TWIST DCs are a significant contribution to the final momentum and angular resolution of the TWIST experiment. These take the form of tables that relate the drift times measured in the detector to the minimum distance between the wire and the positron track in a given drift cell defined by the 4 mm$\times$4 mm region in which a drift wire is expected to detect ionizing particles. These tables were initially calculated using the GARFIELD simulation package. Later analyzes showed that the basic STRs were not sufficient given the variations that might be observed in the chambers both as a function of time and between different chambers. For this reason an approach using the data to calibrate the STRs to better, more appropriate values was adopted. This procedure came from the work of Jingliang Hu and Alex Grossheim.

The method of calibrating the STRs was finalized by Alex Grossheim in 2007. This iterative method minimizes the residuals between the hit positions given to the Helix Fitter and the best fit track using the STR tables themselves as the variable factor. The STRs are smooth so a spline fit is conducted each time the STR tables are regenerated to remove non-linearities that result from the measurement procedure. The calibrated STRs used for data are shown in Fig. 4.7.

The STRs correct for a number of non-uniformities that appear in the drift chambers. The STRs were defined separately for each plane in data, allowing for small variations in the construction and ageing of each chamber. A density correction was implemented to correct changes in the pressure and temperature of the chambers on a run by run basis.

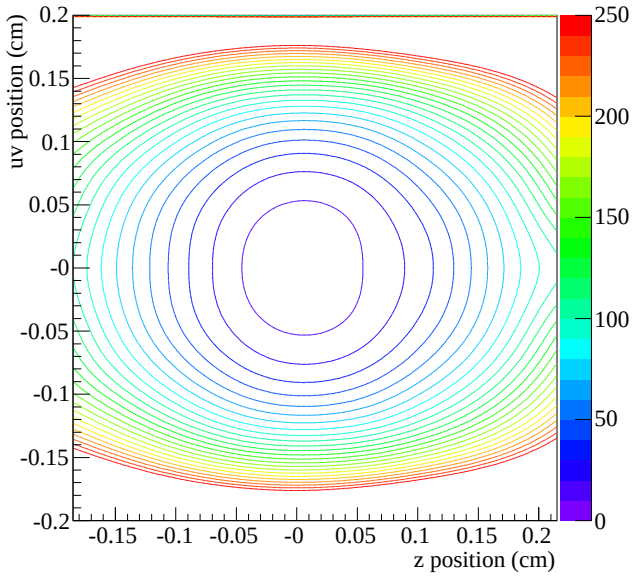

Figure 4.7: The space-time mappings of positions in the drift cell to drift times. The contours show the isochrones of the STRs. Note that the drift wire is the centre, (0,0) position, of the cell. The mapping is the same for both U and V planes.

4.4 Tree Analysis and Event Selection

The results of the `MOFIA` helix fitter analysis were stored in trees compliant with the ROOT software package[33]. A second stage of analysis was applied to the data to select well reconstructed events from the data. No events were cut during the `MOFIA` helix fitter analysis allowing for more flexibility in the creation and tuning of the selection criteria used.

The cuts on the data were chosen to remove events known to present problems in the analysis of the spectrum. These cuts were extensively studied for potential biases that they may introduce both in the shape of the reconstructed muon decay spectrum and differences that they introduce between data and matching simulations. If a cut produces changes in the data spectrum that are not reflected in the simulation, then that cut will make changes in the muon decay parameters that must be evaluated as a systematic as described in Chapter 7. The `MOFIA` analysis may, albeit rarely, generate as many as ten candidate tracks for a single muon decay so the purpose of many of these cuts is to remove unsuitable candidates for the decay positron track.

The following event cuts and selections are used for the nominal decay positron analysis.

- t_{cap}**/m12 width cut**: Selects the surface muons from the data based on the time structure of the beam line, and the scintillator pulse width. In the standard set of cuts the cut on the M12 pulse width is disabled. The selected t_{cap} ranges changed for different collection periods. For silver data this range is 32 ns $< t_{cap} <$ 52 ns, while for aluminum target data this range is 32 ns $< t_{cap} <$ 55 ns.

- **Event type cut**: Selects event types 1, 2, 6, 7, 10, 11, 21, and 22. This removes 53.4% of the selected scintillator triggered events. These event types were selected for their clean event topologies.

- **Muon last plane cut**: Removes events with muons that appear after the stopping target.

- **Muon UV Cut**: If the target PCs indicate that the muon for a particular event enters the stopping target at a position such that $\sqrt{u^2 + v^2} > 2.5$ cm from the centre of the stopping target, then the event is cut from the analysis. This ensures that the muons decay in the target material.

- **PACT cut**: Removes events with muons that stop in PCs 5 and 6. This uses a series of cuts on the PC pulse widths observed in the upstream target PCs. The cut is tuned for each data set by optimizing the asymmetry of the decay positron distributions measured from the decays of the muons that pass the cut. An example of the region allowed by the cut is shown in Fig. 3.11.

- **Track number cut**: Removes the event from consideration if there are no tracks reconstructed.

- **Ierror cut**: Removes any tracks that failed during reconstruction. If no tracks are left the event is cut.

- **Start stop cut**: Removes tracks from the analysis that exist on both sides of the muon stopping target. If no tracks are left then the event is cut from the analysis.

- **Charge cut**: Removes tracks from the analysis if the charge of the track is not positive. If no tracks are left then the event is cut.

- **Pair matching cut**: Checks to see if multiple tracks appear in the event are the result of beam positrons or positron tracks that were broken at the first guess stage. One of the tracks is removed if it is closer than 2 cm from another track in UV or closer in time than 60 ns. The track closest to the target is selected if the track is broken while beam positrons are removed.

- **Muon - positron vertex matching**: Matches the positron track to its source muon vertex. The positron track closest to the muon at the target is kept. Removes secondary tracks that are not correlated in position with the muon stopping position.

- **Selection based on distance to target**: The positron track that is reconstructed closest to the target is kept. Removes secondary tracks that are produced in fits to broken tracks.

- **Decay fit time**: Eliminates events with decay times less than 1050 ns and greater than 9000 ns. The purpose of this cut is to separate muon and positron hits, although there will be an overlap for early positrons. This cut is correlated with the cut on the event type.

The effect of these cuts on the number of events selected by the analysis is shown in Fig. 4.8. The decay positron spectrum reconstructed from data after the event cuts are applied is shown in Fig. 4.9. The gap in the centre of the spectrum is due to event cuts removing poorly reconstructed tracks which appear at high angles ($|\cos\theta| < 0.4$).

4.5 Kinematic Fiducial Region for Data-MC Fits

A kinematic fiducial region must be assumed for measurements of the muon decay parameter fits. The fiducial region is defined by

- 10.0 MeV/c $< p_t <$ 38.0 MeV/c
- $p_z >$ 14.0 MeV/c
- $p_{tot} <$ 52.0 MeV/c
- $0.54 < \cos\theta < 0.96$.

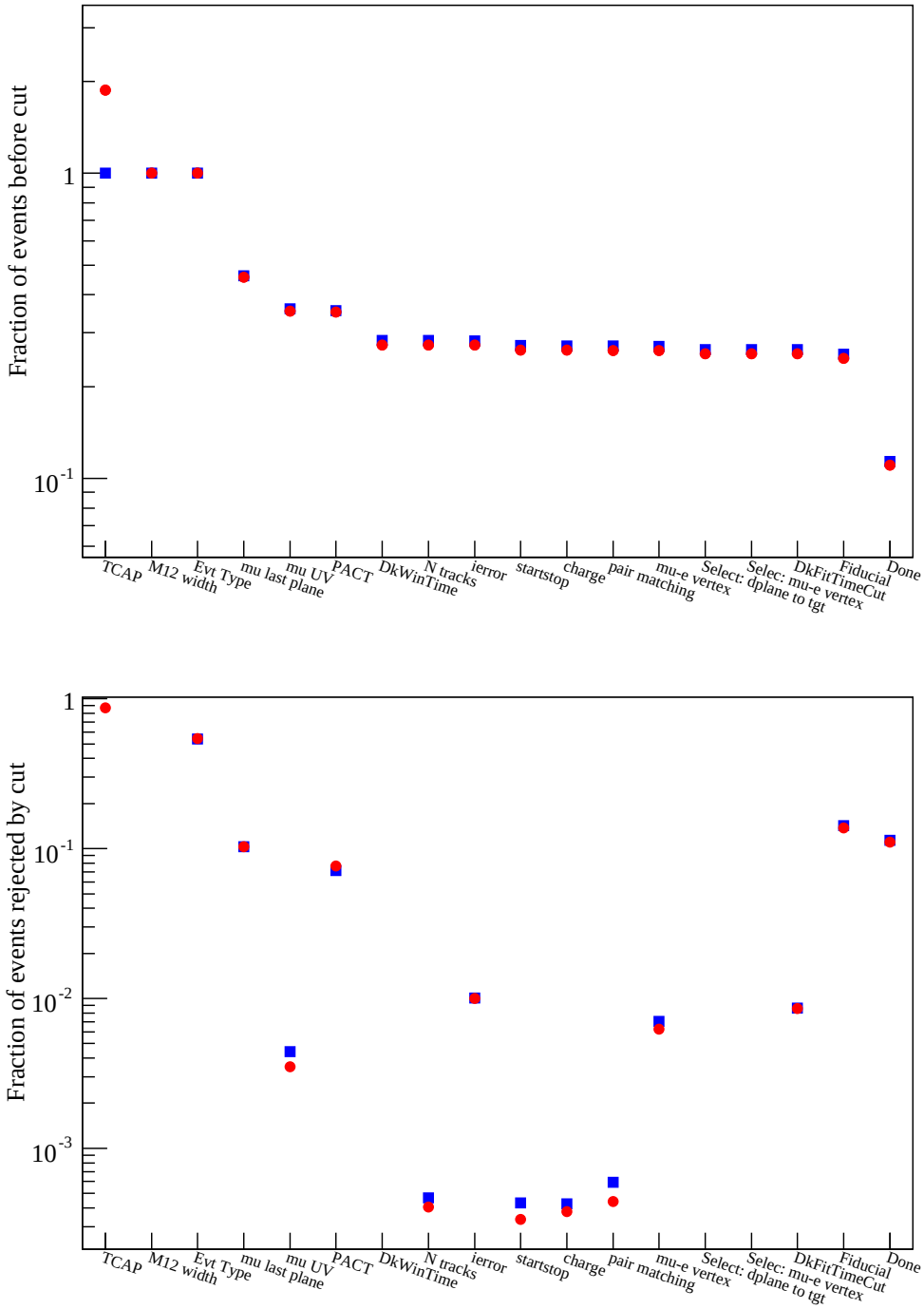

Figure 4.8: The fractional number of events selected (top) and rejected (bottom) by the tree analysis in both data ● and Monte Carlo simulation ■. Data and simulation counts are normalized to the number of events after the t_{cap} cut is applied.

The choice of this fiducial region was based on constraints imposed by the detector and the reconstruction.

The maximum transverse momentum, p_t is dictated by the maximum radius of the positron track. This radius is limited by the physical dimensions of the TWIST detector itself. The inner diameter of the supporting plate for the TWIST drift chamber modules is 33.9 cm. Since the positron must start no more than 2.5 cm from the z-axis, the maximum radius that a positron may possess without hitting the support frame is R_{max} = ((33.9 cm)/2 - 2.5 cm)/2 = 7.22 cm. The maximum transverse momentum of the positron (in MeV/c) contained in the TWIST detector volume is given by $p_t = 300BR_{max}$, where B is the magnetic field in Tesla, and R_{max} is the maximum positron radius in metres. Using the smallest magnetic field used by the TWIST solenoid under data collection is 1.96 T, the maximum transverse momentum of the positron is 42.48 MeV/c. The highly conservative 38.0 MeV/c was chosen to stay well clear of this limit.

The minimum transverse momentum was likewise chosen because of physical limitations of the detector. Tracks with a radius spanning less than a few drift cells cannot

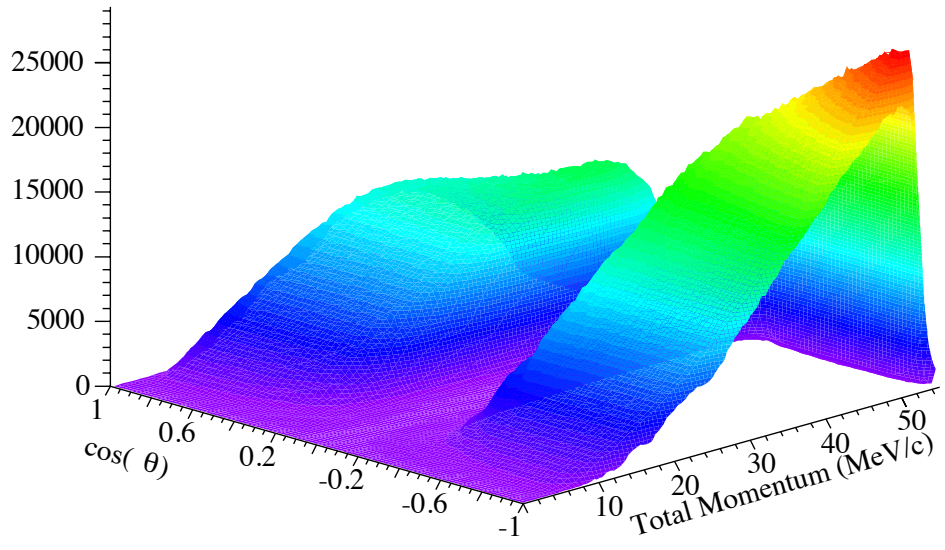

Figure 4.9: A typical positron decay spectrum reconstructed from data

generate a good fit of the positron helix. The chosen limit of 10 MeV/c corresponds to a track with a radius of 1.7 cm.

The fiducial limit on the longitudinal momentum is defined by the periodicity of the detector in the sparse stack. A tracking ambiguity appears for positron longitudinal momenta, p_z, such that the z distance between matching helix phase is equal to fractions of the module spacing. At these longitudinal momenta the positron tracks will produce drift chamber hits at repeating $u-v$ positions, making a good measurement of the track radius unlikely. To minimize this effect, the inter-module spacing alternates between 4.8 cm and 6.8 cm. Tracking ambiguities persist, however. With the current detector configuration positron tracks with wavelengths, λ, equal to 1.9 cm, or longitudinal momenta $p_z = 300B\lambda$ =11.52 MeV/c will produce repeated $u-v$ plane hits. The cut on the longitudinal momentum at 14 MeV/c removed the affected momenta from consideration.

The cuts on the absolute $\cos\theta$ was similarly motivated by reconstruction considerations. At high angles positrons are likely to pass through multiple drift cells which introduces an ambiguity in the determination of the position of the hit nearest to the drift wire. This becomes a problem if the positron approaches enters the drift cell at angles greater than 60° relative to the z-axis of the detector. For this reason the conservative limit of $|\cos\theta| > 0.54$ was adopted. At large $\cos\theta$, or small angles, the resolution becomes very large, due to the combined small radius and large wavelength. A limit of $|\cos\theta| < 0.96$ was assumed to avoid this poor resolution range.

The upper limit on the momentum was defined to avoid the region of the decay spectrum near its endpoint edge of 52.828 MeV/c. The momentum resolution at the momentum edge behaves like $1/\sin\theta$ with values between 70 keV/c and 175 keV/c in the fiducial range of $\cos\theta$. With a momentum loss of 60 keV/c at the endpoint, one can expect the momentum edge to affect the spectrum at up to 600 keV/c below the momentum edge of 52.828 MeV/c. For this reason the upper fiducial limit on the momentum for the purpose of the measurement of the decay parameters was set at 52 MeV/c. The fiducial region is shown in Fig. 4.10.

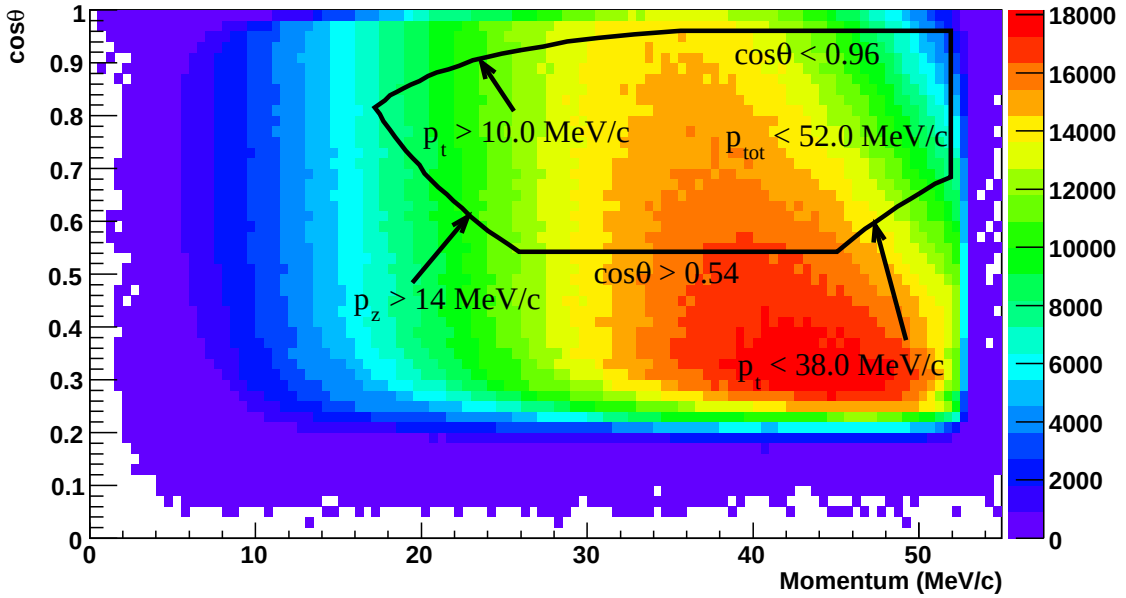

Figure 4.10: Fiducial limits superimposed on the downstream muon decay spectrum.

Chapter 5

Simulation and Validation

TWIST relies heavily on the the simulation of the detector using `GEANT 3` [34]. This simulation reproduces the material and geometry of the TWIST detector to the best of our knowledge. The format of the simulation output reproduces the digitization of the data so that the same analysis process is applied to both the data and the Monte Carlo simulation. By subjecting the simulation to the same reconstruction process and comparing the data directly to the simulation, effects on the decay parameter measurements relating to the reconstruction are eliminated. Only the differences between data and simulation become systematic effects.

It is exceptionally important that the physics in the simulation is validated in the context of the TWIST analysis. This validation takes the form of a direct comparison between the data and the Monte Carlo simulation that does not rely on the underlying physics of the muon decays. The primary way of studying the relationship between data and simulation is done using a special set of data that stops the muons in the far upstream end of the detector. These data were compared to a matching simulation to determine the consistency of the reconstruction.

5.1 The Production of the Simulation

The simulation uses pre-generated $(p, \cos\theta)$ pairs to produce the muon distribution. These pairs are selected in an event generator program external to `GEANT` using an accept-reject method. For some twice differential probability distribution, $\partial^2\Gamma/\partial p\partial\cos\theta = g(p, \cos\theta)$, a uniform random number $y \in \{0, \sup(g(p, \cos\theta))\}$ was generated in conjunction with the random $(p, \cos\theta)$ pair; if $y < g(p, \cos\theta)$ then the

event is included in the sample; otherwise the event is rejected. While the muon decay distribution must be positive definite, the source function $g(p, \cos\theta)$ can assume negative values in this implementation. When $g(p, \cos\theta)$ assumes negative values the function is separated into negative and positive regions for the purpose of the accept-reject method and the y value must be less than the magnitude of the surface in the region. If the event appears in a negative region the sign is carried forward in the analysis and the spectrum generated in the event selection is filled with negative events in the appropriate region. This functionality was required for the definition of the derivative spectra that will be discussed in Section 6.1.

A record is kept of the total number of random $(p, \cos\theta, y)$ triplets generated, N_{thrown}. The total N_{thrown} is scaled by a factor $1/y_{max}$ after the spectrum generation so that the effective selection range for the accept reject method, independent of the properties of $g(p, \cos\theta)$, is $y' \in [0, 1]$. This allows the comparison between spectra generated using different functions for $g(p, \cos\theta)$.

5.1.1 Radiative Corrections

The muon decay spectrum is based on the tree level four fermion interaction as shown in Eq.2.9 with radiative corrections including the logarithmic corrections proportional to orders of $L = \ln(m_e/m_\mu)$, $\mathcal{O}(\alpha^2 L)$ [16], $\mathcal{O}(\alpha^2 L^2)$, and $\mathcal{O}(\alpha^3 L^3)$ [17]. The magnitude of these corrections relative to the tree level spectrum is shown in Table 5.1. The singularity at the endpoint of the NNLO, $\mathcal{O}(\alpha^2)$, correction is thought to cancel with contributions from other terms and so the generated spectrum is considered to be effective up to that order. Radiative corrections were programmed into the TWIST event generator, as part of the $g(p, \cos\theta)$ distribution, using the code used in Arbuzov *et. al.*[17]. These corrections are used to alter the shape of the decay spectrum and do not produce real photons in the simulation. The effect of the radiative corrections on the isotropic spectrum is shown in Fig.5.1, with the higher order corrections are shown in Fig. 5.2.

5.1.2 Selection of Decay Parameters

The muon decay parameters were generated randomly and hidden from the experimenters before the analysis of the 2006 and 2007 data. The blinded parameters were encrypted and stored in a database for later reference. The encryption key was written to a CDROM, which was stored in a safe at TRIUMF. Three of the de-

Correction	Normalized Integral
$\mathcal{O}(\alpha)$	-0.007555
$\mathcal{O}(\alpha^2 L^2)$	-2.667 $\times 10^{-4}$
$\mathcal{O}(\alpha^2 L)$	1.965 $\times 10^{-4}$
$\mathcal{O}(\alpha^3 L^3)$	6.07 $\times 10^{-6}$
ad hoc Exponential	4.228 $\times 10^{-5}$
Virtual Pairs	-5.247$\times 10^{-5}$

Table 5.1: Integrated contribution to the isotropic decay spectrum made by each of the radiative corrections, normalized to the integral of the isotropic Born level spectrum.

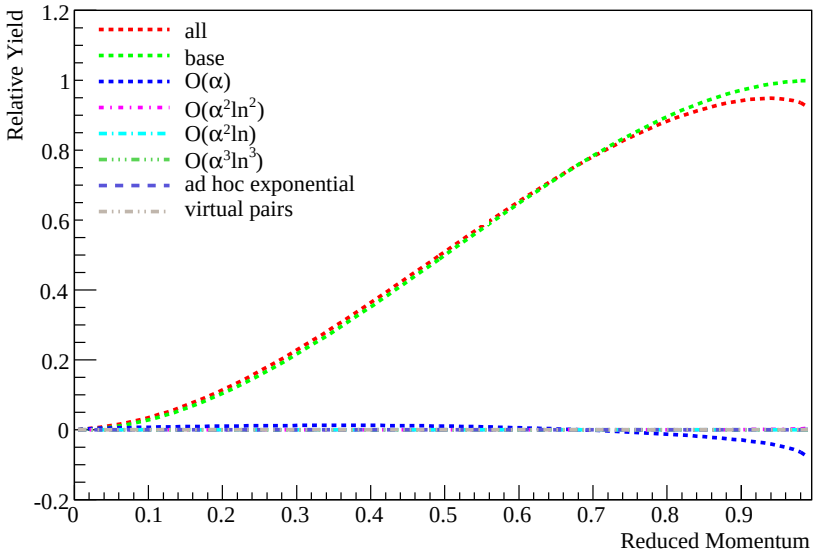

Figure 5.1: The isotropic spectrum used for the generation of the muon decay samples for the simulation. The final spectrum with all corrections is shown along with the base, or Born level, decay spectrum, as well as all radiative corrections. The only correction with a magnitude visible on this scale is the $\mathcal{O}(\alpha)$ correction.

cay parameters were generated using a uniform random number contained by the ranges, $\rho \in [0.74, 0.76]$, $\delta \in [0.74, 0.76]$ and $\xi \in [0.99, 1.01]$. The η parameter was not blinded and was fixed to the central value from the 2005 global analysis [18]; $\eta = -0.0036 \pm 0.0069$. The terms proportional to η are scaled by a factor of $m_e/W_{e\mu} = 0.0097$, which makes a blind four parameter analysis difficult. The decision was made to fix η to the best value known at the time the blind analysis was initialized.

The decay samples were generated long before the full simulation was carried out. The full statistics required for the Monte Carlo generation were planned before the generation was started. It was assumed that a factor of 3 increase over the statistics of an estimated 10 data sets would be more than sufficient to achieve the analysis goals of the experiment. To this end, 4.86×10^4 samples of 5×10^5 random events, for a total of 2.43×10^{10} events were generated prior to the analysis. A simulation for a typical data set used up to 2000 samples meaning that there are typically 1.5×10^9 events in a standard simulation. The samples were stored on a server to which the TWIST experimental group does not have direct access.

5.1.3 TWIST GEANT

TWIST uses a custom modified version of `GEANT 3` for simulations of muon events in the detector. The changes from the base versions of the software were completed by Peter Gumplinger, Denis Wright, and other members of the collaboration as required. Most changes were made to interface `GEANT` with input files containing the geometry, space time relationships, time zeros, etc., and in the digitization of the output so the output may be read by `MOFIA`. No changes were made to the fundamental physics of

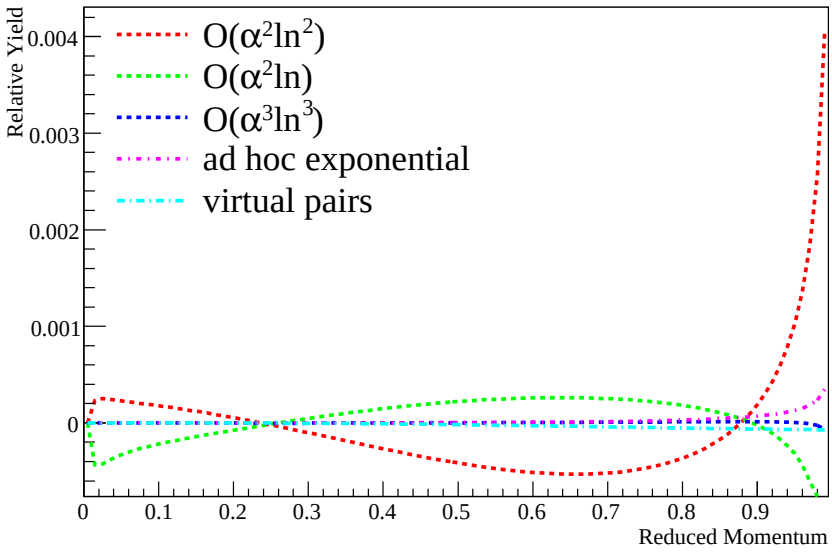

Figure 5.2: The isotropic radiative corrections below $\mathcal{O}(\alpha)$. The magnitude of the spectra in the figure are identical to those in Fig. 5.1 with the scale of the figure expanded.

the simulation.

The decays are simulated in a software reproduction of the TWIST detector. The elements of the TWIST detector are modelled using standard simulation volumes, whose properties are based on the `GEANT 3` material definitions. The simulated detector consists of the drift chambers inside the bore of the solenoid and limited by the yoke. The components of the experimental apparatus are hard coded into the simulation. The geometry of the detector itself, including the thickness and dimensions of the stopping target, the positions of the cathode foils and wire planes, and the positions of the scintillation counters, is defined in a geometry file which is input into the simulation at run time.

The beam line is not simulated. A series of beam profiles which define the trajectories of muons as they enter the magnetic field were extracted from the TEC beam line characterization runs. The muons generated by the simulation start from a position and direction dictated by the probability distributions defined using these input beam profiles. The time structure of the muon beam is not reproduced.

Particles are tracked through the magnetic field region using a fourth order Runge-Kutta integration. The OPERA generated magnetic field is used in the simulation for this tracking process. The integration is completed over finite steps, accounting for continuous momentum loss through the simulated volumes. Random processes such as electron-positron scattering, and bremsstrahlung are generated as a function of these steps; the number of steps between random events is dictated by the cross section of the process in question. Sub-routines were added to `GEANT 3` to allow for the tracking of the muon spin as it passes through the detector.

Simulation conditions are set using an input file called the `ffcards`. Parameters controlled by these files include the mean operation temperature, muon and positron beam rates and momenta, the magnetic field at the centre of the detector, and the density of the material in the muon gas degrader. Many of the ffcard parameters were used for the measurement of systematics by simulating conditions that could not be produced in the real detector. Options also exist which control the presence of physics processes such as "discrete" energy loss processes typified by δ-ray and bremsstrahlung production.

The response of the detector was duplicated as best as possible. The TDC distribution shapes are reproduced for each of the simulated DC chamber hits. This simulation must include the behaviour of the ionization clusters within the chambers as the particles pass through the chambers. By simulating this response the time

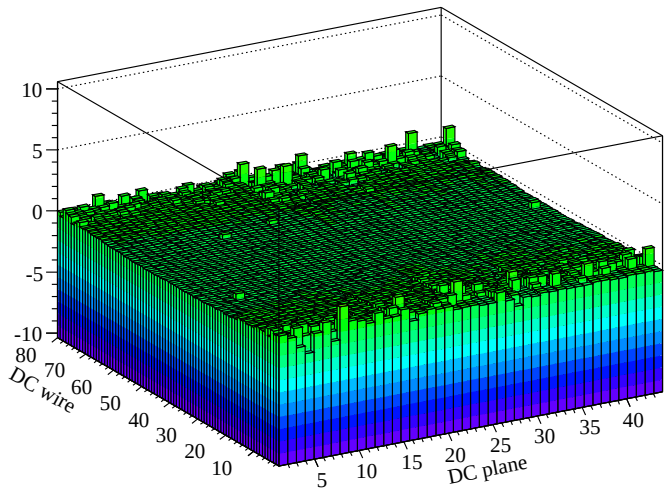

Figure 5.3: Time zeros measured from Monte Carlo simulation. The values are uniformly zero with the exception of a few values at the edges of the chambers where the wire occupancies are low.

zeros can be determined from the TWIST DCs in the same way for both the data and the simulation. Since the simulation must have null time zeros for all of the wires, this functionality of the simulation provides a direct validation of the time zero measurement method. The distribution of time zeros in the simulation is shown in Fig.5.3

The drift properties of the DCs are reproduced using the `GARFIELD` software package. Effectively the results of this simulation are the first order space time relationships used for the analysis without the data derived calibration. It was found quite early on in the experiment that the reconstruction of the Monte Carlo simulation does not work optimally when the simulation is analyzed using the same set of STRs as those used for the generation of the simulation. This motivates generating sets of Monte Carlo calibrated STRs by minimizing time residuals from the helix fitting routine in an analogous procedure to the calibration of the STRs for data, as described in Section 4.3.3.

The Monte Carlo simulation carries the real state of a given event as it passes through the simulation. This information is stored in a substructure of the root trees, generated by the `MOFIA` analysis, called the Monte Carlo truth banks. The truth banks come in two flavours; the space point banks which give the momentum

and angle of the positron at each ionization cluster, and the vertex banks which give the momentum and angle of the positron at a small set of points, or vertexes, in the detector. The space point banks are not usually used because of the huge increase in the file sizes that result. The vertex banks are routinely used for testing and characterizing the detector response. The available vertices are at the muon decay position, the first DC plane hit, the last DC plane hit, and the point when the simulation terminates the positron. Two special vertices were defined at DC 22 and DC 23, for validation studies.

5.1.4 Analysis of Simulation

The calibrations applied to data are also applied to simulation. The analysis used to generate the time zero calibrations, the alignment procedure, and the STR corrections were all applied to the simulation to ensure that biases and noise incidentally introduced by these measurements are reproduced in the simulation. This step was taken to reduce potential systematic errors that may be introduced by the measurement procedures of these calibrations.

There are two changes in the application of the tree analysis of the data versus its application to the simulation. In the real beam this time structure has serious repercussions on the muon polarization, but all muons are generated in the simulation with 100% polarization. As the cut on the particle time of flight, t_{cap}, is applied to identify surface muons, the t_{cap} cut is not applied to the simulation. The PACT cut is specifically tuned in the simulation to remove stops in the PC chamber gas. For the Monte Carlo simulation this optimization is completed to remove the same fraction of events in both data and simulation. This optimizations was completed once for all of the simulations.

5.2 Upstream Stops Data

A special type of data was collected to probe the analysis response of the TWIST detector in a way that can be reproduced equally for both data and Monte Carlo simulation. In these data the muons are stopped in the upstream end of the detector, and are hence called upstream stops data. Decay positrons travelling in the downstream direction are observed as they pass through the entire detector stack. The positron tracks are then fit separately across the upstream and downstream halves

of the detector. The differences in the fitted helices then describe the detector and analysis response across the target module independent of the underlying physics of muon decay. The differences in the momentum or angle across the target module are used to demonstrate the validity of the simulation and its reconstruction in direct comparison with the data. This has some important consequences on the understanding of the simulated positron interactions and the corresponding systematics; the results of the comparison of these difference distributions indicate the degree to which the simulation can be trusted. The disappearance of tracks across the target module is used as a measure of the reconstruction inefficiency across the detector. The upstream stops results were used to determine the scale of systematic effects related to the reconstruction.

5.2.1 Experimental Conditions

To stop the muons in the far upstream end of the detector both the muon momentum and the material in the detector is altered. The beam-line was tuned to a momentum of 27.0 MeV/c to decrease the range of the muons entering the detector. This decrease in the momentum means that muons from deeper in the production target, with lower polarization, will appear in the beam line. A 0.01 inch thick (254 μm) Mylar film degrader was inserted into the beam to further slow the muons. The gas degrader was set to maintain the mean of the muon stopping distribution in the upstream PCs. The stopping distribution of the muons in the chambers is shown in Fig. 5.4.

5.2.2 Analysis

The upstream stops data use the same `MOFIA` analysis as the target stops, with a few exceptions. The upstream and downstream halves of tracks passing through the full detector stack are fit separately. All tracks in the detector are fit, regardless of their classification since the event classification is optimized for muons stopping in the target. In particular the designation of beam positron events is suspect because many of the muons actually stop in the muon scintillators rather than the drift chambers, so no muon will be observed in the chambers.

This mode of analysis requires that both the upstream and downstream positron tracks move in the downstream direction. However, the position tracks are calculated with respect to the DC nearest the target module, as described in Section 4.2.3. Consequently the upstream positron trajectory is "tracked" in the backwards direction,

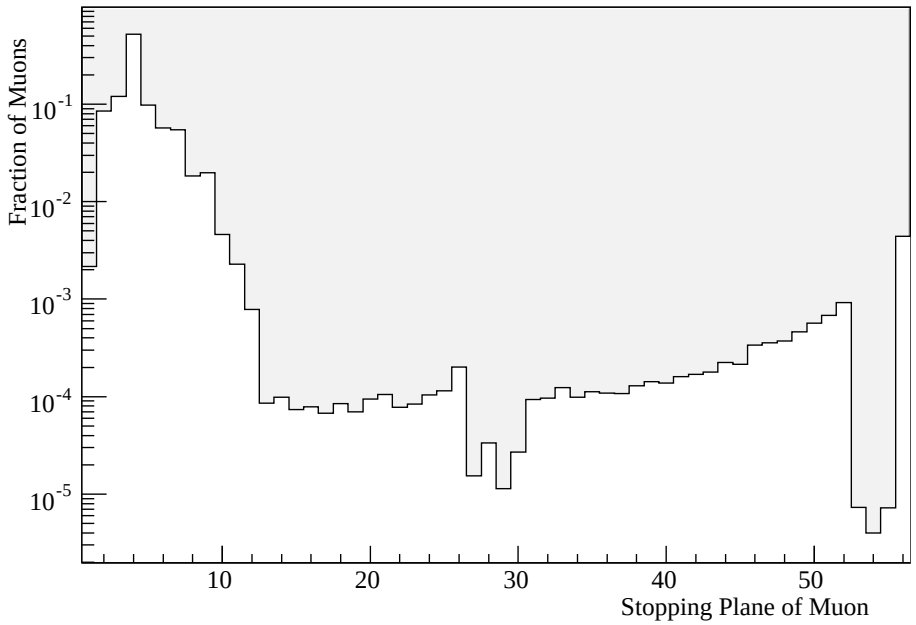

Figure 5.4: Fractional muon stopping distribution from upstream stops data collected with the aluminum stopping target. In this data set 73% of muons stopped in the upstream PCs.

as the energy loss correction must be added to the track relative to the initial point of the track.

The event cuts were applied to the data after the `MOFIA` analysis. The purpose behind these cuts is to produce a pure sample of positrons passing through the stopping target material. The cuts are defined as follows;

- **Decay window (Dkwin)**: Only decay positron windows and beam positron windows are accepted. Overlap windows are removed.
- **Muon stop**: If there is a muon appearing in the event it must stop in the upstream PCs or earlier.
- **Decay time**: The decay time of the muon must be greater than 800 ns.
- **Full detector**: The event must involve PCs at both ends of the detector.
- **Single tracks**: No more than one track can appear in the upstream side and the downstream side of the detector. This decision was made to simplify the

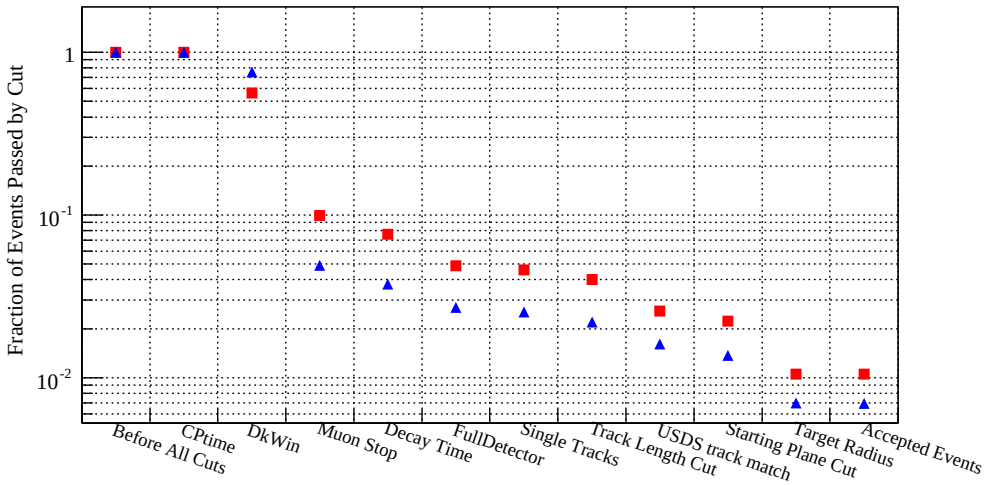

(a) Silver stopping target data and simulation

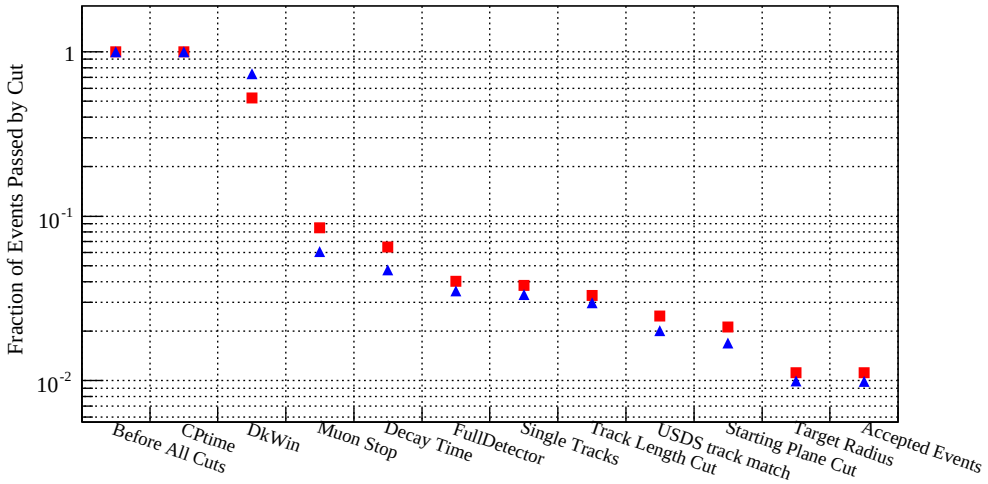

(b) Aluminum stopping target data and simulation

Figure 5.5: The fractional number of events passed by the cuts on data ■ and simulation ▲.

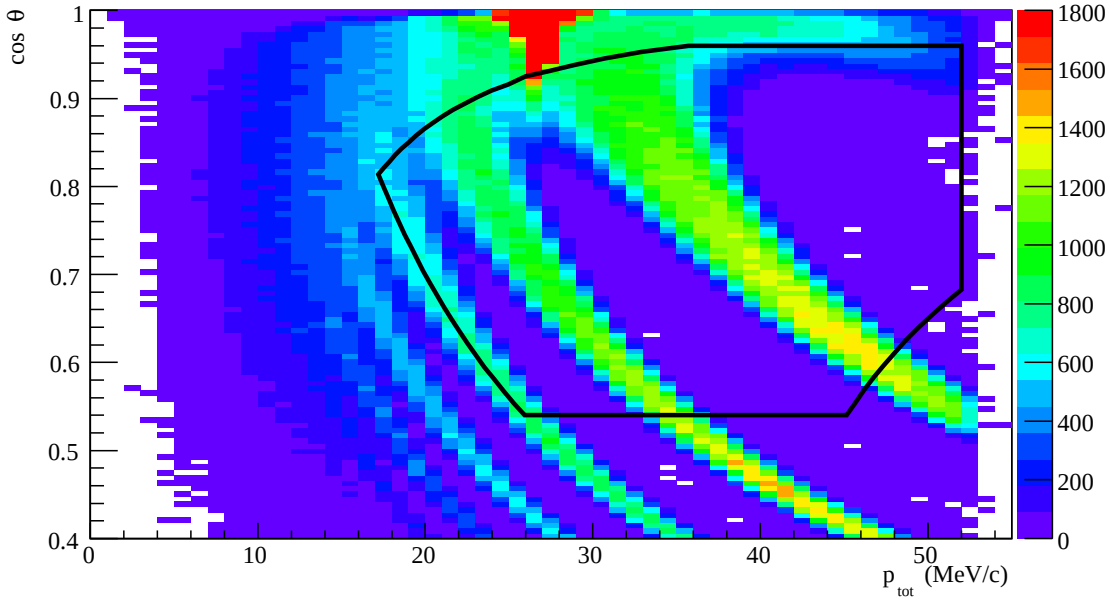

Figure 5.6: Spectrum of positron tracks measured from the upstream half of through-going tracks after the full set of cuts described in Section 5.2.2. Poor occupation of large regions in the plot are due to the 4 cm target radius cut required for the standard aluminum target. These features are reproduced in simulation insofar as the muon stopping distribution is matched between data and simulation. The fiducial region is circumscribed by the black lines. The bright red feature at the top centre of the plot is due to the presence of beam positrons.

analysis so that it probes the positron interactions within the target module. This will suppress events where there are delta raw of bremsstrahlung processes in the detector stack.

- **Track length**: The track must include more than 16 drift planes. Implies that no tracks broken in the sparse stack are considered by the analysis.

- **USDS track match**: There must be one track in both sides of the detector stack.

- **Positron starting/stopping plane**: The upstream track must start after DC plane 21 and stop before DC plane 2, while the downstream track must start before DC plane 24 and end after DC plane 43. This ensures that the helix fits have a common reference point and extend through the full detector stack. If these cuts are relaxed, the distribution of track lengths is different for upstream

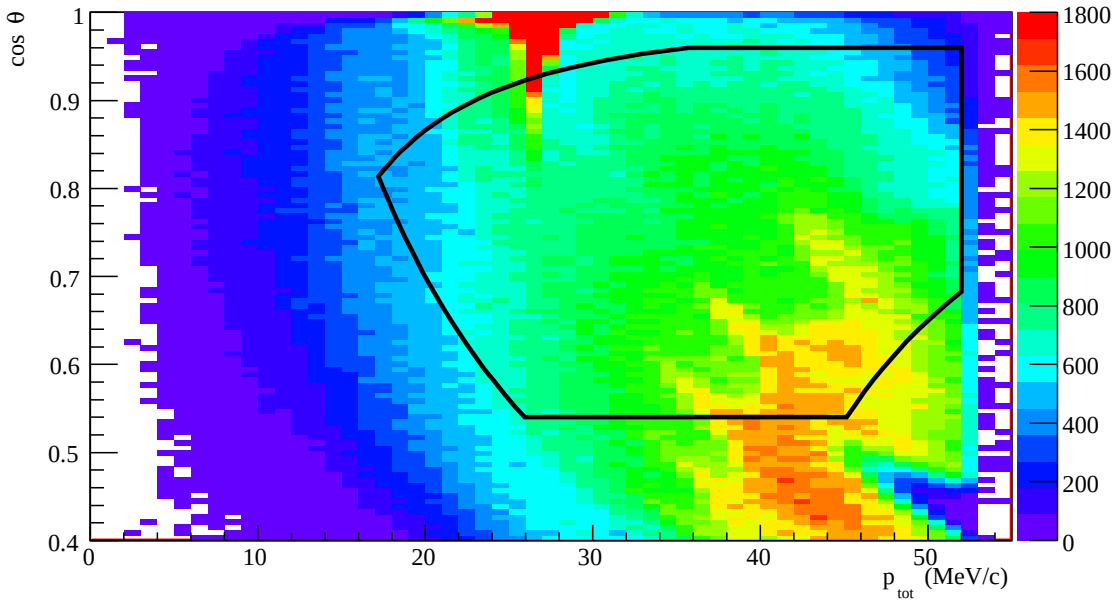

Figure 5.7: Spectrum of positron tracks measured from the upstream half of through-going tracks passing through the large aluminum target. The black lines inscribe the fiducial region. The 12 cm radius cut effectively removes the low occupancy regions shown in Fig. 5.6.

and downstream tracks, which may bias the momentum loss measurement

- **Target radius**: the extrapolation of the positron track to the target intersects with a region 4 cm about the centre of the target. In the large target data this region is extended out to 12 cm. This ensures that no tracks pass through the target support material which was poorly simulated in `GEANT`.

- **Fiducial region**: the momentum and angle of the positron track both upstream and downstream of the stopping target must appear in the kinematic fiducial region, as defined in Section 4.5. This ensures that the positron track is well reconstructed on both sides of the detector

The effect of the cuts on the number of effects in the analysis is shown in Fig. 5.5. The spectra compiled from the positron tracks that pass these cuts is shown in Fig.5.6 for the standard aluminum target and Fig.5.7 for the large aluminum target. These figures show the effect of the target radius cut on the occupancy of the spectrum. Large sections of the spectra collected using the standard stopping target geometry are depleted away from bands of constant p_z at 14 MeV/c, 19 MeV/c, and 28 MeV/c.

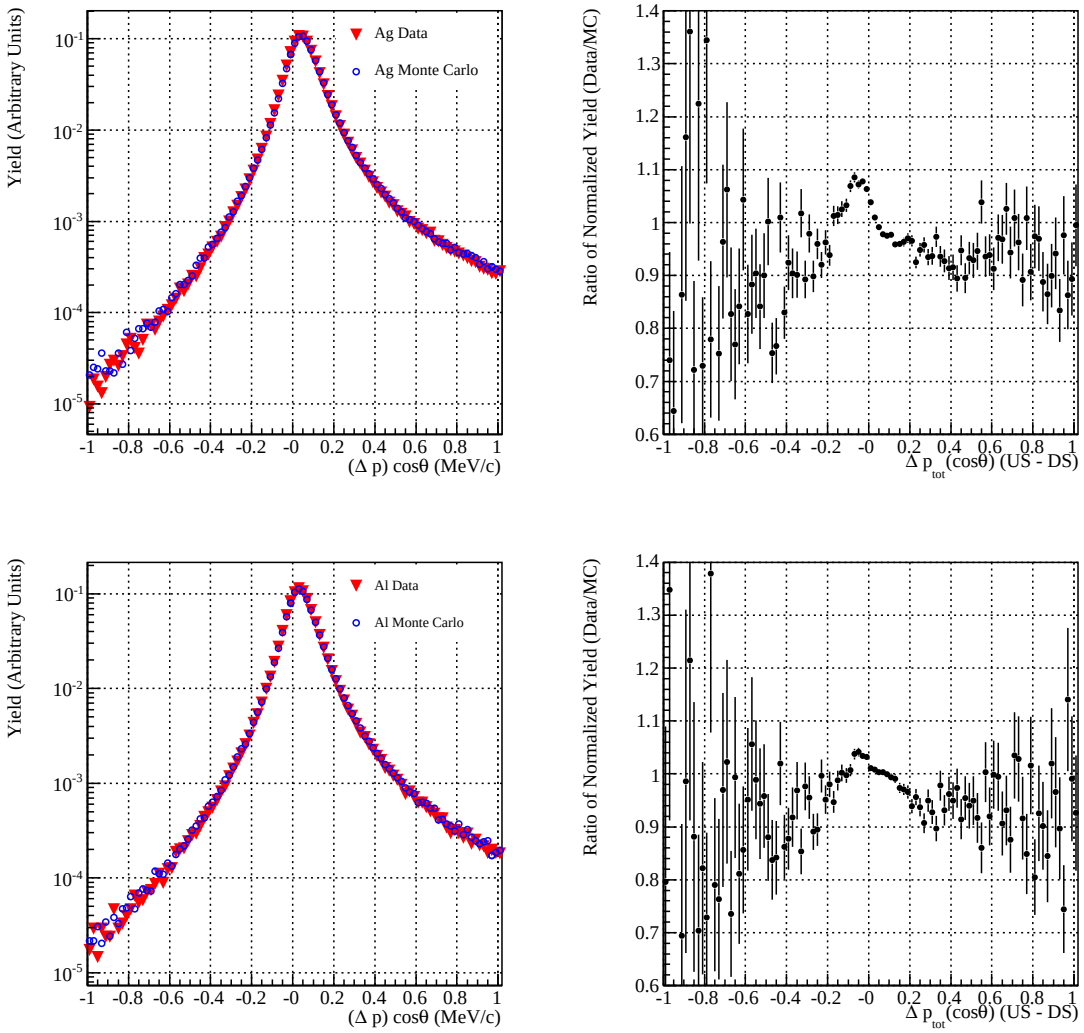

Figure 5.8: Integrated $(\Delta p)\cos\theta$ distributions for silver (top) and aluminum (bottom) data and simulation. The curves on the right show the ratio between the data and simulation curves on the left. The deviation in the ratio is proportional to the difference between the peak momentum loss in data and simulation.

5.2.3 Fiducial Averaged Momentum Loss

The momentum response of the TWIST detector can be characterized using the distribution of the upstream stops results integrated over the entire fiducial region. The primary contributions to the detector response are the momentum loss through the detector and target modules and the helix fitter energy loss correction, which displaces the momentum response distribution according to the estimated momentum loss in

the detector stack. To first order the momentum response then increases linearly with $\sec\theta$ due to the planar geometry of the TWIST detector. The values of Δp_{US-DS}, the difference between the upstream and downstream halves of a positron track, are multiplied by $\cos\theta_{US}$ to remove this natural dependence of the momentum response. The $(\Delta p_{US-DS})\cos\theta_{US}$ distributions for the standard silver and aluminum targets are shown in Fig. 5.8. The $(\Delta p_{US-DS})\cos\theta_{US}$ distribution is highly asymmetric with a long tail of high momentum loss tracks. This tail reflects energy loss fluctuations through the gaseous drift chamber region as well as the target module so it cannot be well described using a Landau-Vavilov distribution. The tail toward $(\Delta p)\cos\theta < 0$ also appears in the distribution because of a combination of the reconstruction resolution and the energy loss correction used in the helix fitter, which alters the zero point of this distribution, does not remove the energy loss fluctuations.

Since the mean momentum loss is a poorly defined quantity, the most probable value (MPV) of the $(\Delta p)\cos\theta$ distribution is used to characterize the behaviour of the momentum response. This poses some problems as the MPV of the momentum loss distribution does not possess a perfect $\sec\theta$ behaviour, but it is close enough for the purpose of the characterization of the difference between data and simulation.

As previously stated, the $(\Delta p_{US-DS})\cos\theta_{US}$ distribution is a poor match for a Landau distribution, so the properties were determined using a truncated Gaussian over a 1 σ range about the mean. The width of the peak is initially estimated by determining the full width at half maximum of the distribution before the first fit is generated. A Gaussian fit is then iterated with an updated fit range at each step. The optimal value of the peak is found when successive fits converge to the same result. A systematic uncertainty for the process is defined by performing the Gaussian fits with the range displaced by one bin above and below the final fitting range. The results of this fitting procedure applied to $(\Delta p_{US-DS})\cos\theta_{US}$ distributions for all TWIST stopping targets are shown in Table 5.2.

The largest difference appears in the silver target data and simulation at 3.0 $\pm$ 0.7; 2% of the 186 keV/c total momentum loss through the detector, with a Gaussian probability of 10^{-9} that the data and the Monte Carlo simulation are consistent. This difference suggests the simulated target is thicker than the real target in the detector by approximately 2.3 μm. A measurement of the silver target thickness, completed by James Bueno[35] showed that the silver target thickness was 30.9 $\pm$ 0.6 μm, while the simulated target was 29.5 μm; opposite of the conclusion from the upstream stops. This suggests that there are uncertainties in the total momentum loss of the detector

Target Material	Data	Simulation	Prediction
Peak	$\Delta p \cos\theta$ (keV/c)	$\Delta p \cos\theta$ (keV/c)	$\Delta p \cos\theta$ (keV/c)
Silver (s73/g473)	40.37 ± 0.46	43.36 ± 0.43	43.26 ± 0.01
Aluminum (s80/g580)	32.25 ± 0.42	32.98 ± 0.57	35.38 ± 0.01
Large Al. (s89/g689)	20.47 ± 0.52	21.44 ± 0.60	25.803 ± 0.002
Width	$\Delta p \cos\theta$ (keV/c)	$\Delta p \cos\theta$ (keV/c)	$\Delta p \cos\theta$ (keV/c)
Silver (s73/g473)	55.46 ± 0.20	54.84 ± 0.26	NA
Aluminum (s80/g580)	53.28 ± 0.26	52.21 ± 0.25	NA
Large Al. (s89/g689)	52.61 ± 0.17	52.29 ± 0.14	NA
Peak	$\Delta\theta$ (mrad)	$\Delta\theta$ (mrad)	$\Delta\theta$ (mrad)
Silver (s73/g473)	-0.00 ± 0.14	-0.20 ± 0.11	0
Aluminum (s80/g580)	0.13 ± 0.15	-0.09 ± 0.12	0
Large Al. (s89/g689)	0.15 ± 0.06	-0.01 ± 0.10	0
Width	$\Delta\theta$ (mrad)	$\Delta\theta$ (mrad)	$\Delta\theta$ (mrad)
Silver (s73/g473)	21.09 ± 0.08	20.65 ± 0.10	NA
Aluminum (s80/g580)	11.43 ± 0.06	11.30 ± 0.05	NA
Large Al. (s89/g689)	9.32 ± 0.03	9.71 ± 0.03	NA

Table 5.2: Properties of integrated momentum loss ($\Delta p \cos\theta$) and scattering ($\Delta\theta$) distributions. The measurements from the reconstructed data and Monte Carlo are shown along with the most probable momentum loss predicted from the Monte Carlo truth banks. The properties of the reconstructed data and simulation momentum difference distributions were determined using a truncated Gaussian to determine the peak and width of the peak independent of the long, asymmetric tails of the momentum difference distributions. The properties of the scattering distributions were determined in the same way. The predicted momentum loss was determined from the most probable value of a Landau function fit to the difference of truth bank momenta at DC 22 and DC 23. The widths of the resulting functions are not comparable.

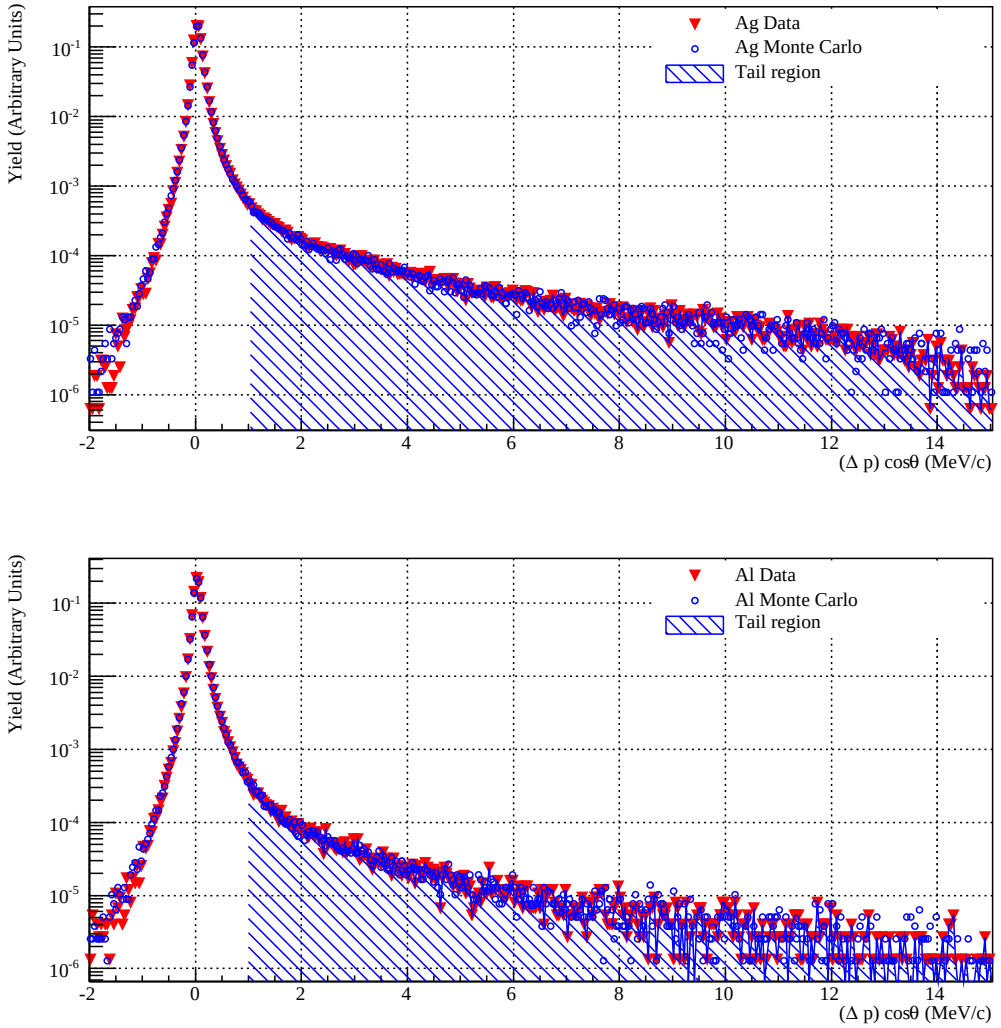

Figure 5.9: The high energy tail of the $(\Delta p)\cos\theta$ distribution for silver (top) and aluminum (bottom) data and simulation. The shaded region is the tail region used for the definition of the bremsstrahlung counting ratios shown in Table 5.3.

that are unrelated to the target thickness.

The difference is less significant for the aluminum target used for the collection of muon target stops data. The integrated data-Monte Carlo difference is 0.73 keV/c, which is less than 1% of the total momentum loss through the detector. This implies a 45% probability that the simulation is consistent with the data.

The high momentum tail of the $(\Delta p_{US-DS})\cos\theta_{US}$ distribution, presented in Fig. 5.9 is related to the rate of bremsstrahlung production in data and simulation. This

	N_{tail}	N_{total}	$R_{tail} = N_{tail}/N_{total}$
Ag. Data	25385	1616581	$(15.70 \pm 0.10)\times10^{-3}$
Ag. MC	14472	916463	$(15.79 \pm 0.13)\times10^{-3}$
Al. Data	5723	754214	$(7.59 \pm 0.10\ )\times10^{-3}$
Al. MC	6179	785173	$(7.87 \pm 0.10)\ \times10^{-3}$

Table 5.3: The ratio of events in the high momentum tails of the $(\Delta p)\cos\theta$ distributions.

allows for a direct test of this class of discrete positron interactions that appear in `GEANT 3` as it relates to the data. The ratio of the number of counts in this high momentum loss tail, N_{tail}, to the total number of counts in the $(\Delta p_{US-DS})\cos\theta_{US}$ distribution N_{total} can be used to characterize the presence of this high energy loss process. N_{tail} is defined as the number of counts that appear 1 MeV/c above the MPV of the distribution. The ratio of counts in the $(\Delta p)\cos\theta$ tails appear in Table 5.3. The relative number counts in the momentum response tail is consistent at for silver target data compared to the simulation. The aluminium tail count ratio in data is separated from the simulated ratio by 3 σ. These results are used to inform the bremsstrahlung rate systematic which will be discussed in Section 7.1.1.

5.2.4 Fiducial Averaged Multiple Scattering

An average scattering angle can be found by considering the MPV of the $\Delta\theta$ distribution integrated over the fiducial region. The MPVs and widths of these distributions for all three target modules are shown in Table. 5.2. The distributions and their differences are shown for data and Monte Carlo simulation in Fig. 5.10.

The width of the scattering distribution is approximated by [4]

$$\theta_0 = \frac{13.6MeV}{\beta cp}\sqrt{\frac{x}{X_0}}\left[1 + 0.038\ln(x/X_0)\right] \tag{5.1}$$

where p and βc are the momentum and velocity of the positron, while x/X_0 is the thickness of the material in radiation lengths. The aluminum target scattering distribution is more narrow than the silver target scattering distribution because of the dependence of the radiation length on the atomic charge Z.

The expectation is that this distribution, which represents the scattering of the positrons through the target module, has a maximum at zero, but again it is the

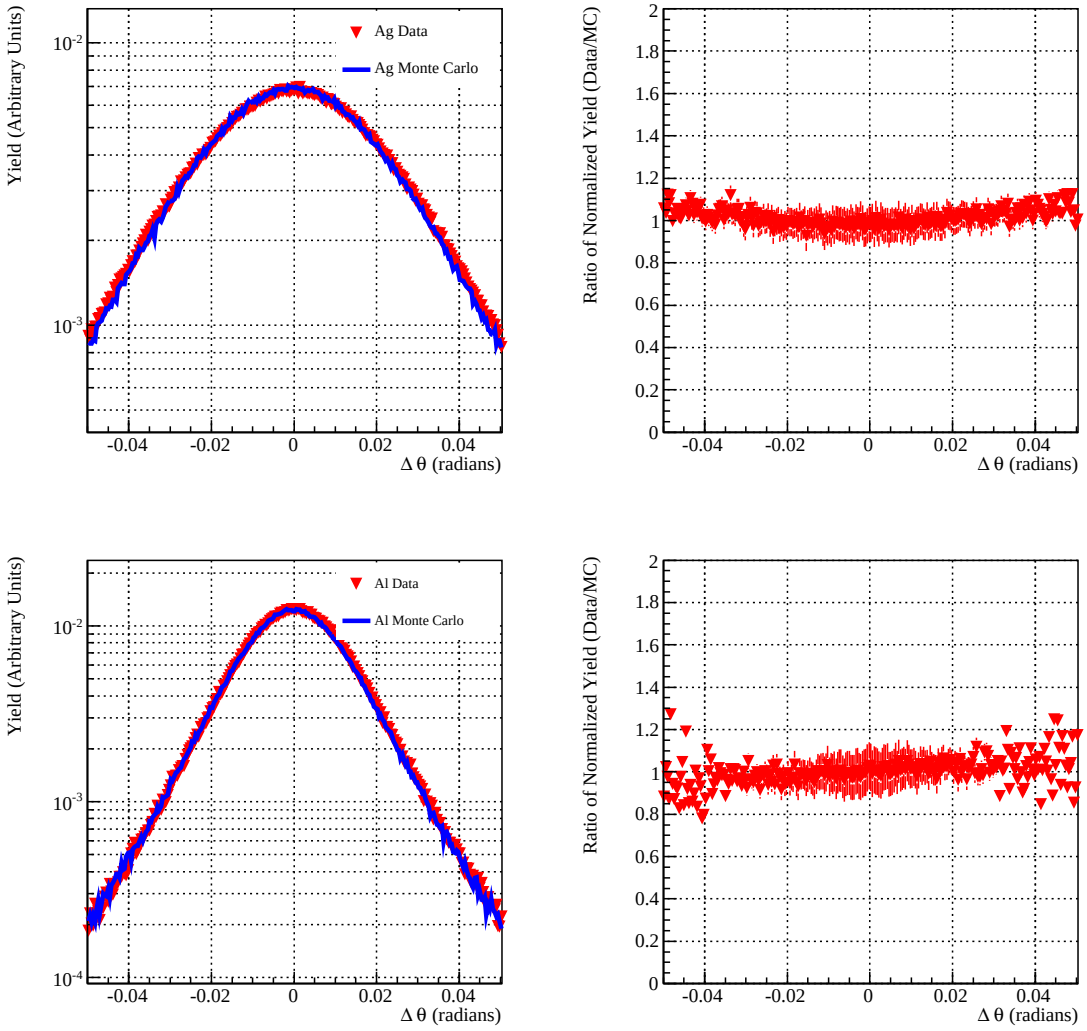

Figure 5.10: Integrated $\Delta\theta$ distributions for silver (top) and aluminum (bottom) data and simulation. The curves on the right show the difference between the data and simulated curves on the left.

difference between data and Monte Carlo simulation that has the foremost consideration. For the silver stopping target the difference in the scattering between data and Monte Carlo simulation is 0.2 mrad or 1.12σ. The difference in the peak scattering for the aluminum target is also 0.22 mrad or 1.14 σ. The simulation of the positron scattering through the target is consistent with the data.

The width of the $\Delta\theta$ distribution does change significantly between data and simulation in silver, but this change is consistent with the existing measurement of

the silver target. The ratio between the measured widths of the $\Delta\theta$ distributions is 1.021 ± 0.006. The prediction for this ratio is roughly the square root of the ratio of the target thickness measured from data over the target thickness used in simulation — that is $\sqrt{30.9\mu\text{m}/29.5\mu\text{m}} = 1.02 \pm 0.02$. This known difference between the data and the simulation is well represented by the difference in the width of then $\Delta\theta$ distribution. Likewise, there is a small known difference in the aluminum target thickness of ((71.6 $\pm$ 5) μm - 71 μm) = 0.6 $\pm$ 5 μm, yielding an expected ratio in scattering widths of 1.004 $\pm$ 0.007. The measured ratio is 1.011 $\pm$ 0.007, again yielding a good agreement between the upstream stops result and the prediction.

5.2.5 Confirmation of Momentum and Angle dependence in Momentum Loss Measurements

The discussion in Section 5.2.3 requires that the momentum response of data and simulation behave in the same way with respect to momentum and angle. This assertion can be confirmed by looking at the momentum response as a function of momentum and $\sec\theta$. The radius cut required for the standard stopping targets results in large sections of the momentum angle phase space where no positron tracks pass the analysis. The large target data were taken with the specific purpose of testing this assumption.

The most probable value of the momentum loss distribution in large target data is shown in Fig. 5.11. In data, the MPV of the momentum response is roughly linear with respect to $\sec\theta$ and effectively independent of momentum. In contrast, a noticeable momentum dependence appears in the simulation of the large target data. The difference between data and Monte Carlo simulation is demonstrated in Fig. 5.12. In this Figure the MC - data difference in the MPV of the momentum response is separated into slices constant in momentum. These slices are fit with a first order polynomial with respect to $\sec\theta$ and the parameters are shown in the bottom panels. The momentum dependence of these parameters is characterized by the function $y = a(p/p_0 - 1) + b$ where p_0=52.828 MeV/c, a describes the momentum dependence of the parameter, in units of momentum, and b is the value of the parameter at p_0.

This analysis shows no appreciable momentum dependence in the offset of the difference between data and Monte Carlo simulation while there is a clear momentum dependence in the $\sec\theta$ slope of the difference in simulation and data MPVs. However, when the standard aluminum target is considered, no significant momentum

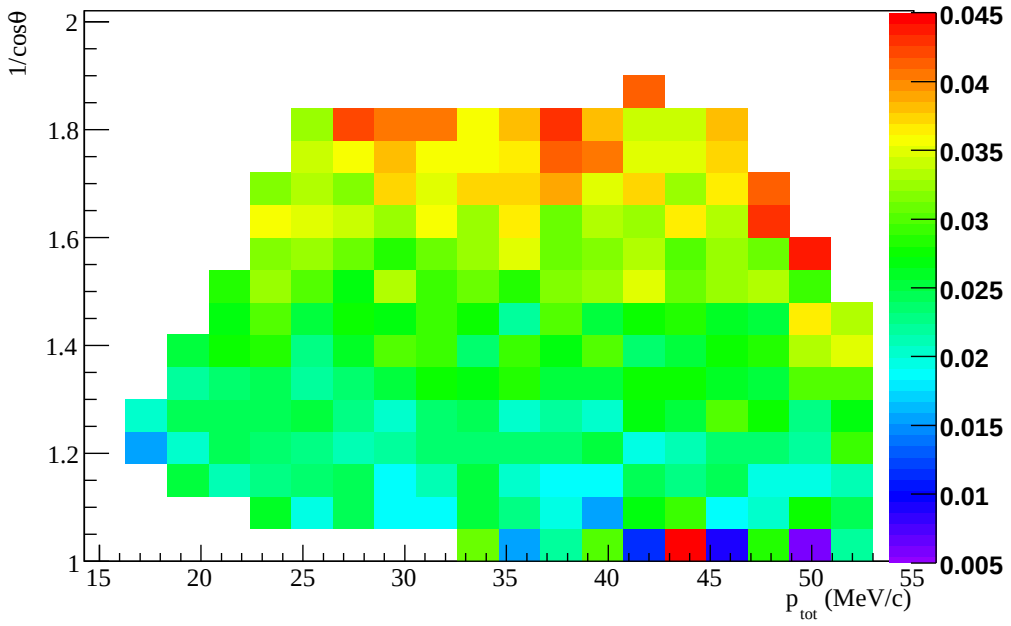

Figure 5.11: The most probable momentum difference between upstream and downstream positron helix fits from large target data. The vertical scale is in MeV/c

behaviour appears in the sec θ slope. The well defined points with momenta less than 35 MeV/c contradict the results from the large target. At best these result can set limits on the possible momentum and angle dependent behaviours of the momentum response. The sec θ slope of the momentum response has a momentum dependence such that -5 keV/c$< a <$10 keV/c. The angle independent difference shows a non-zero value at all momenta for both the large and standard aluminum targets suggesting that a change in the momentum loss between data and the Monte Carlo simulation is not the only contribution to the difference. If the momentum loss was the main contribution to this figure the angle independent contribution should be zero.

There are some very clear differences between data and simulation that appear from the momentum difference distribution integrated over momentum and angle. This difference is much more significant in the data collected with the silver over the aluminum target. The statistics and more importantly the occupancy of the kinematic phase space of the upstream stops makes it difficult to produce a good model for the source of the discrepancy.

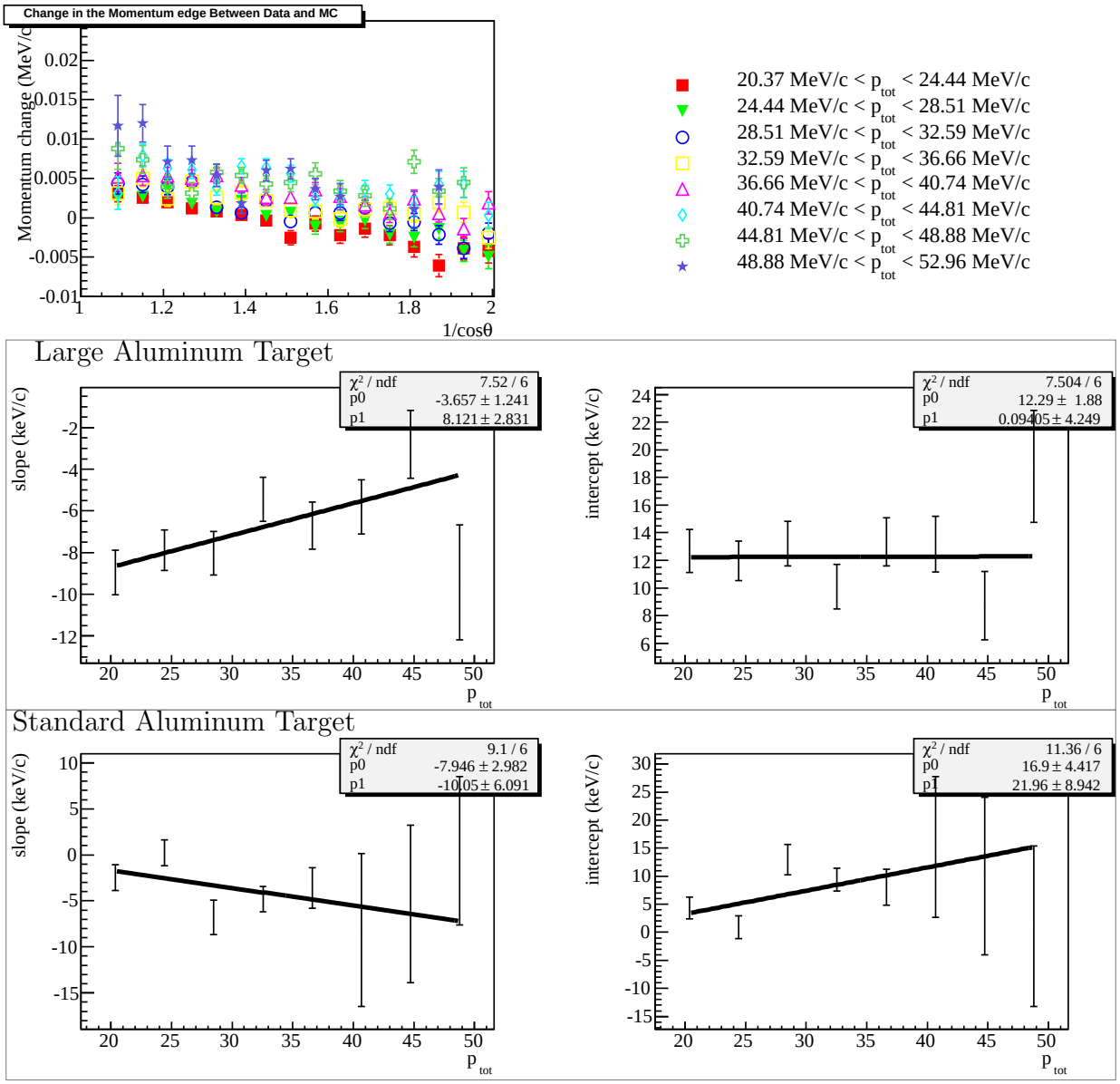

Figure 5.12: The difference of the MPVs of the momentum response distribution between data and the Monte Carlo simulation decomposed to show its behaviour with respect to momentum and angle. The top left panel shows the difference in the most probable values of the data and the Monte Carlo as a function of momentum and angle in the large aluminum target. The middle two panels show the sec θ dependent slope (left) and the angle independent intercept (right) as functions of momentum for the large aluminum target where the effect on the occupancy by the radius cut is minimized. The bottom two panels show the same figures for the standard aluminum target. The difference in the effective momentum loss for data and Monte Carlo simulation has the opposite behaviour with respect to momentum for the two different Aluminum targets. The results for the standard silver target are similar to the standard aluminum target.

5.3 Analysis Inefficiencies

Establishing the relative reconstruction inefficiency between the upstream and downstream inefficiency is important for the measurement of the asymmetry parameter measurements. In simulation this inefficiency can be measured in an absolute sense by comparing the number of reconstructed events directly to the number of events that exist according to the simulation. In data, a comparison between upstream and downstream tracks from upstream stops events must be used because a measure of the number of unreconstructed tracks within the fiducial region does not exist.

5.3.1 Upstream-Downstream Inefficiencies

A reconstruction inefficiency can be defined in upstream stops by counting the number of tracks that are successfully reconstructed on one side of the detector and are not reconstructed on the other. This number can then be normalized by the total number of reconstructed tracks to define a conditional probability for the reconstruction. For example the probability that a track is reconstructed in the upstream detector stack but not reconstructed in the downstream stack is given by,

$$P(d|U) = \frac{N_d}{N_U} \tag{5.2}$$

where N_d is the number of events reconstructed in the upstream detector but not in the downstream detector while N_U is the total number of events reconstructed in the upstream detector. This definition of a downstream inefficiency is attractive because it can be applied to data and the Monte Carlo simulation equally. A similar definition can be made for an upstream inefficiency by counting events reconstructed downstream but not upstream, N_u, and comparing the result to the total number of events reconstructed in the downstream half N_D.

The inefficiencies can be compiled as a function of momentum and angle as shown in Fig.5.13. The standard fiducial region is outlined in black. A weighted average inefficiency was compiled from the events that fall within the fiducial region for both data and the Monte Carlo simulation for each target module. The inefficiency averaged over the upstream and downstream kinematic fiducial regions is shown in Table 5.4. The uncertainty used for a given bin was defined using a ROOT function `TGraphAsymmErrors::BayesDivide`, which uses an application of the Bayes Theorem to define an error for an inefficiency ratio such as Eq.5.2. This is to deal with the

Target/Detector Half	Simulation Ineff. ($\times 10^4$)	Data Ineff. ($\times 10^4$)	averaged Difference (MC - data, $\times 10^4$)
Aluminum US	3.96 ± 0.16	3.74 ± 0.16	0.36 ± 0.23
Aluminum DS	5.71 ± 0.18	6.15 ± 0.19	-0.30 ± 0.28
Silver US	4.54 ± 0.16	3.74 ± 0.11	-030 ± 0.20
Silver DS	7.13 ± 0.18	7.47 ± 0.15	-0.58 ± 0.25

Table 5.4: The weighted average inefficiency within the standard fiducial region measured from the number of tracks that do not appear in the indicated half of the detector but do appear in the opposite half normalized by the total number of tracks that appear on the opposite half of the detector.

	Silver Target	
	Intercept ($\times 10^{-4}$)	Slope ($\times 10^{-4}$)
US ineff. diff.	4.6 ± 1.5	-5.9 ± 2.0
DS ineff. diff.	4.6 ± 1.8	-7.1 ± 2.5
	Aluminum Target	
	Intercept ($\times 10^{-4}$)	Slope ($\times 10^{-4}$)
US ineff. diff.	5.1 ± 1.7	-6.4 ± 2.3
DS ineff. diff.	3.5 ± 2.1	-5.3 ± 2.8

Table 5.5: Linear fits with respect to $\cos\theta$ of the differences in upstream and downstream inefficiencies.

extreme cases when the inefficiency $P(u|D)$ approaches zero or one [36].

The inefficiency serves a dual diagnostic purpose as a test of the systematic significance of upstream-downstream reconstruction differences and as a test of the consistency of data and Monte Carlo. The consistency of the reconstruction is shown by considering the average differences shown in the far right hand column of Table 5.4. The difference in inefficiency in data and the Monte Carlo simulation is on the order of parts in 10^5, which is at the limit of the statistical uncertainty. These differences are also considered as functions of momentum and angle are shown in Fig.5.14. The difference of the inefficiencies of data and simulation show no momentum dependence and a significant dependence on $\cos\theta$. This dependence can be modelled with a straight line; the results of these fit are shown in Table 5.5. These behaviours were used to quantify the scale of the systematic effect of reconstruction inefficiencies on the muon decay parameters, which will be discussed in Chapter 7.

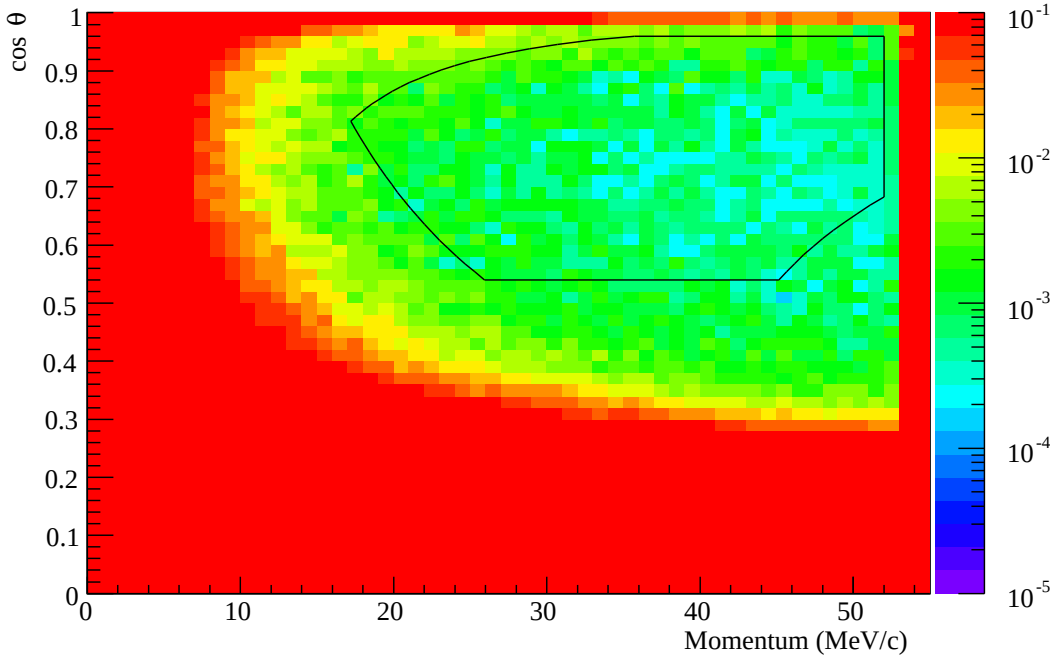

(a) Downstream inefficiency

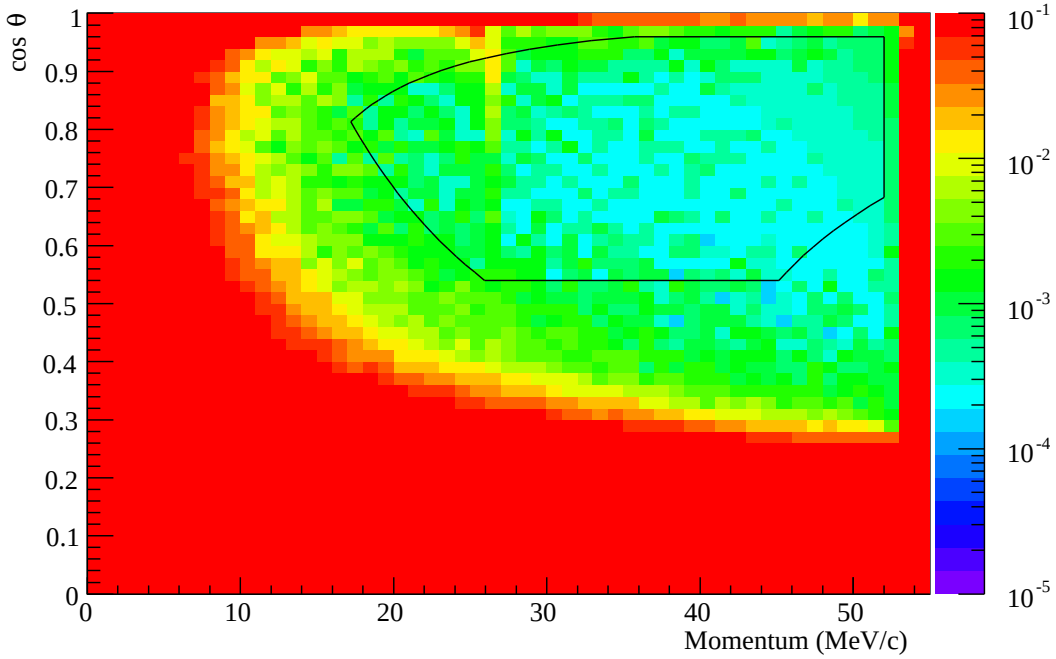

(b) Upstream inefficiency

Figure 5.13: Inefficiency as a function of momentum and angle from upstream stops data taken with the standard aluminum target module installed. The feature that appears at $\cos\theta$ near 1 and momenta between 23 and 27 MeV/c is due to beam positron contamination. These regions are cut out of the average inefficiencies tabulated here.

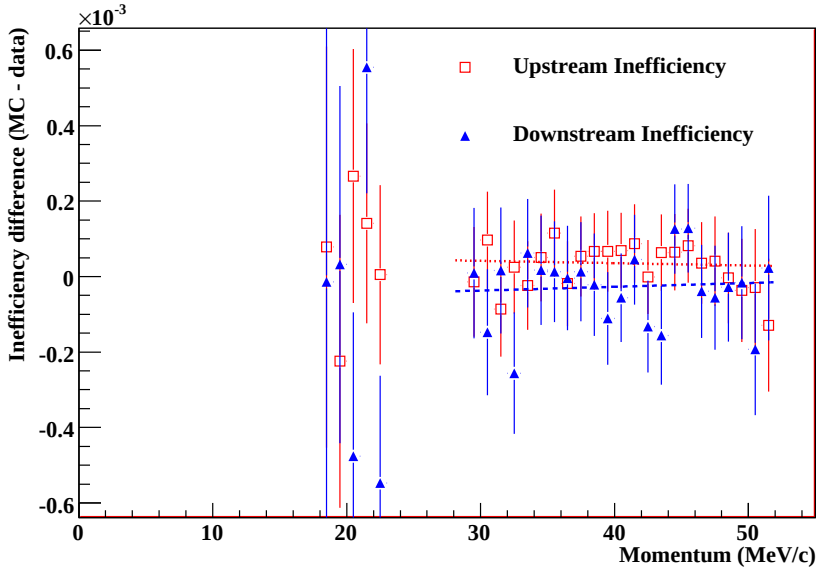

(a) Difference between inefficiencies from data and Monte Carlo averaged with respect to angles over the fiducial region

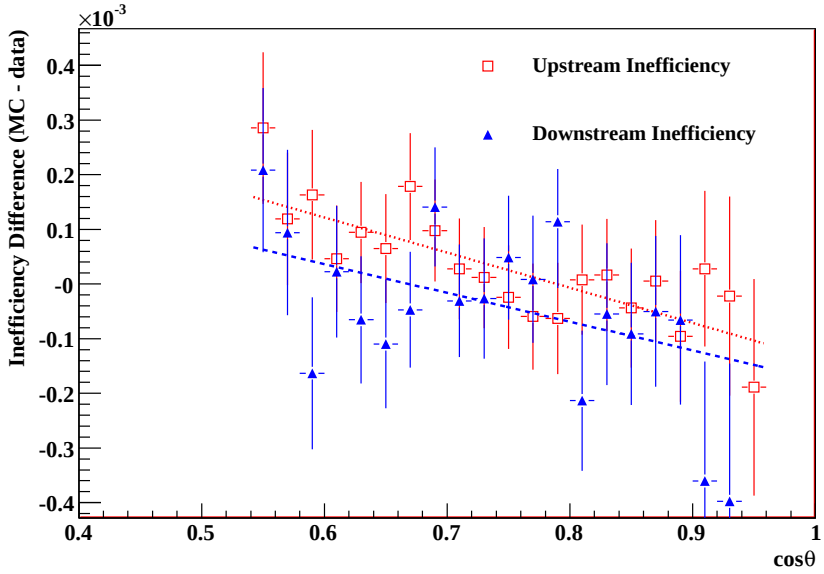

(b) Difference between inefficiencies from data and Monte Carlo simulation averaged with respect to momenta over the fiducial region

Figure 5.14: Differences between data and Monte Carlo simulation inefficiencies integrated with respect to angle and momentum across the fiducial region. Upstream and downstream differences are shown. Linear fits to the differences with respect momentum are consistent with zero, while the linear fits with respect to $\cos\theta$ are shown in Table 5.5.

Chapter 6

Monte Carlo Fitting

The muon decay parameters are measured from the data through a direct comparison between data and a matching Monte Carlo simulation. This is accomplished in a three step process to parametrize the difference of the shape of the spectrum. A comparison of the endpoint of the data and Monte Carlo spectra is completed to determine a relative calibration for the reconstructed momenta. A set of parameters describing the calibration are input to a second event selection analysis of the data. A fit of the shape of the calibrated data spectrum to the Monte Carlo spectrum is completed to find the changes in the decay parameters between the spectra. These two procedures are intimately related as each procedure affects the result of the other.

6.1 Decay Parameter Fit

The decay parameter fit uses a linear expansion of the muon decay spectrum to determine small changes in the decay parameters. This linear expansion is accomplished by adding spectra corresponding the partial derivatives of the full muon decay spectrum with respect to the muon decay parameters. The linear expansion is shown

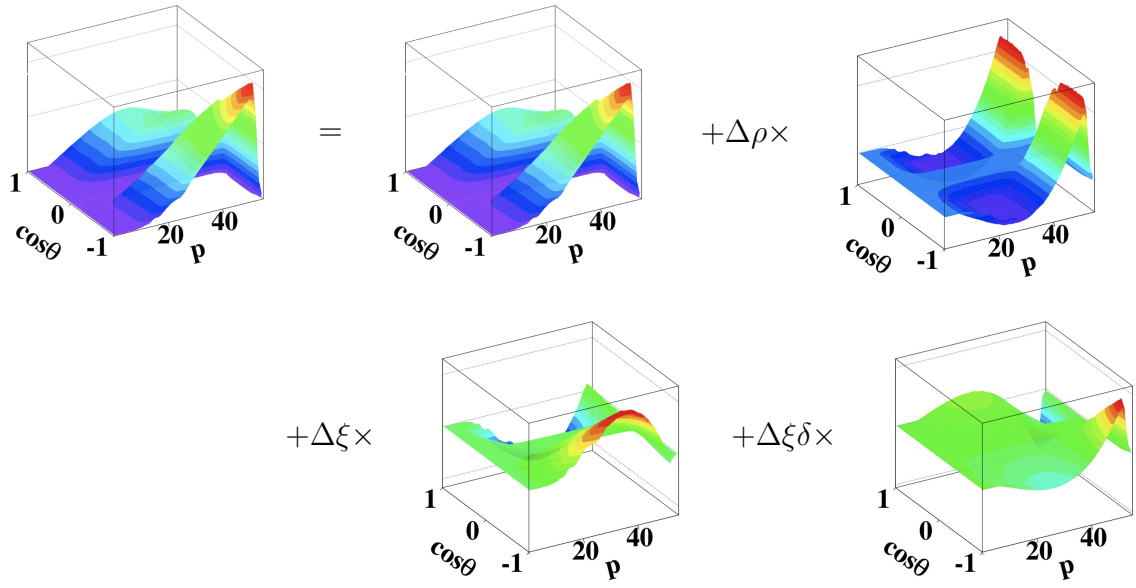

Figure 6.1: Monte Carlo spectra are combined to match the data to the simulation. The weights of the derivative spectra are the changes in the decay parameters between data and simulation.

graphically in Fig. 6.1. Algebraically the derivatives used in this fit are,

$$\frac{\partial S}{\partial \rho} \propto \sqrt{x^2 - x_0^2}(4x^2 - 3x - x_0^2) \tag{6.1}$$

$$\frac{\partial S}{\partial \eta} \propto x_0\sqrt{x^2 - x_0^2}(1 - x) \tag{6.2}$$

$$\frac{\partial S}{\partial \xi} \propto \cos\theta(x^2 - x_0^2)(1 - x) \tag{6.3}$$

$$\frac{\partial S}{\partial \xi\delta} \propto \cos\theta(x^2 - x_0^2)(4x - 3 + (\sqrt{1 - x_0^2} - 1)). \tag{6.4}$$

This notation, where the derivatives of the combination of $\xi\delta$ is held independent of the derivative with respect to ξ, is important to make the decay spectrum linear, and to reduce correlations in the fitting procedure itself. The relative magnitudes of the isotropic derivatives, ρ and η, are shown in Fig. 6.2, while the theoretical shapes of the ξ and $\xi\delta$ derivatives are shown graphically in Figures 6.3 and 6.4. To generate the spectra, these expressions are used as the differential decay distribution, $g(p, \cos\theta)$, in the black box generation described in Section 5.1. The capability of the spectrum generation to handle spectra that are not positive-definite was added to handle the derivative spectra which assume negative values at particular momenta or angles.

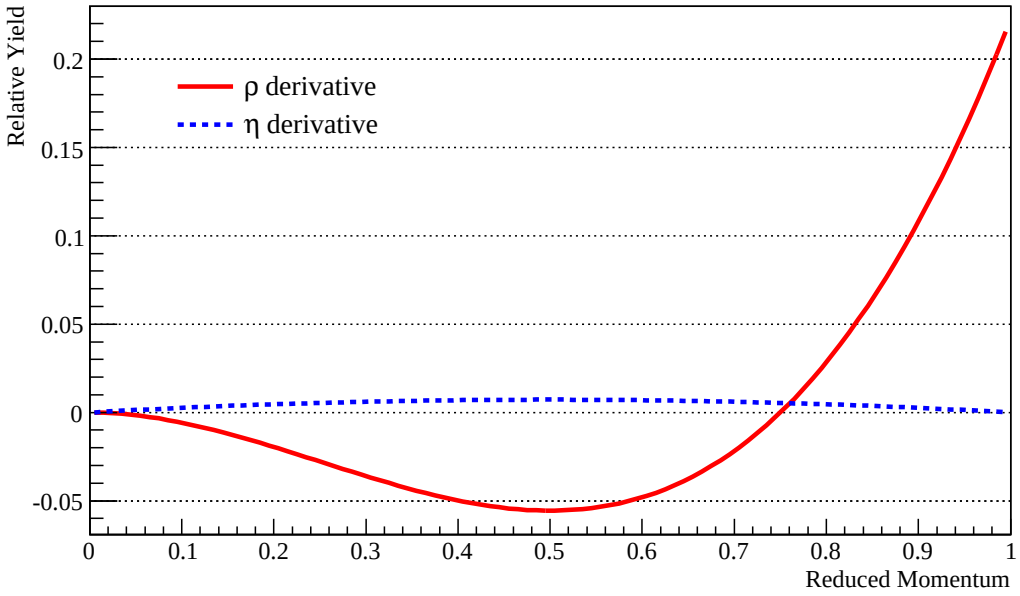

Figure 6.2: A comparison of the relative magnitudes of the ρ and η derivatives.

The resulting samples are used in `GEANT` simulations and analyzed in the same way as the standard muon decay simulation. The positron spectra that are reconstructed from this simulation are called the derivative spectra.

The sum of the derivative spectra and the base decay spectrum are used to define the function used in a linear fit of the decay spectrum. This procedure was developed and coded as the `mcfitter` program by Andrei Gaponenko [37]. For each decay parameter value $\varpi \in \{\rho, \xi\delta, \xi|_{\xi\delta}\}$, the ith bin of the normalized derivative spectrum is,

$$\nu_i = \frac{N_i\left[\frac{\partial S}{\partial \varpi}\right]}{N_{thrown}\left[\frac{\partial S}{\partial \varpi}\right]}, \tag{6.5}$$

where $N_i\left[\frac{\partial S}{\partial \varpi}\right]$ is the ith fiducial bin of the simulated derivative spectrum, and $N_{thrown}\left[\frac{\partial S}{\partial \varpi}\right]$ is the number of events produced during the spectrum generation as described in Section 5.1. To relate this spectrum to the base muon decay spectrum, an efficiency is defined to relate the total number of reconstructed events to the number of events thrown in the generation of the spectrum;

$$\mathcal{E} = \frac{N[S]}{N_{thrown}[S]} \tag{6.6}$$

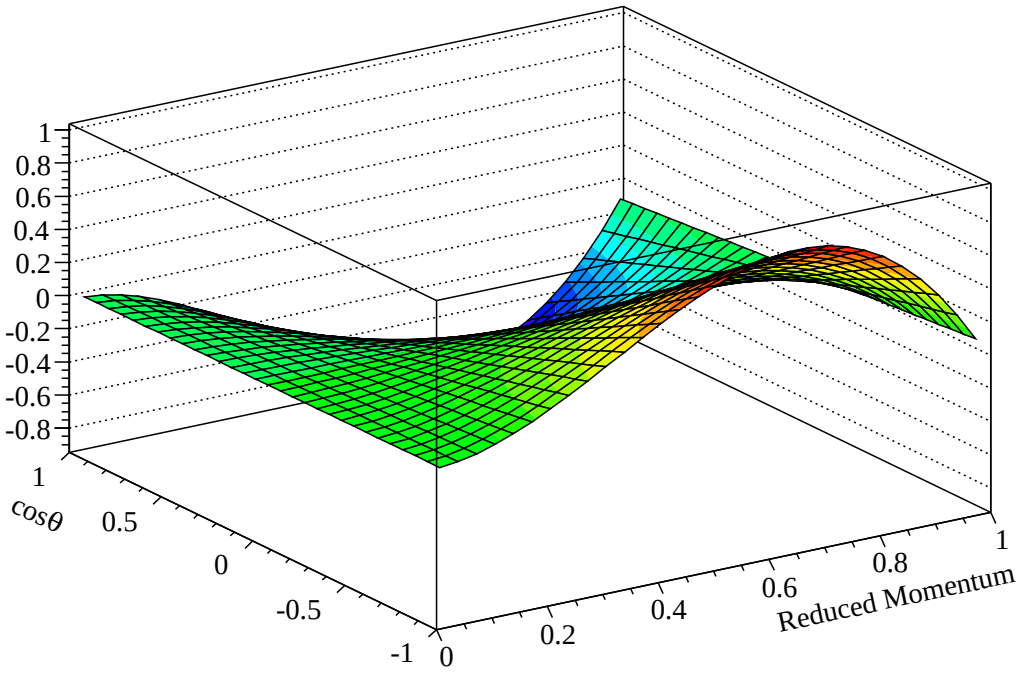

Figure 6.3: The theoretical ξ derivative spectrum in terms of the reduced momentum. The radiative corrections are added to this spectrum alone of the derivative spectra.

where $N[S] = \sum_{i=0}^{J} N_i[\Gamma]$ is the sum of all histogram bins contained within the kinematic fiducial. For small changes in the decay parameters, $\Delta\varpi$, the ith fiducial bin of the normalized spectrum is expanded to,

$$n_i(\varpi + \Delta\varpi) = \left(1 - \sum_{\alpha}^{M} \Delta\varpi_\alpha \mathcal{E}^{-1} \nu^\alpha\right) n_i(\varpi) + \sum_{\alpha}^{M} \Delta\varpi_\alpha \mathcal{E}^{-1} \nu_i^\alpha, \tag{6.7}$$

where, $n_i = N_i[\Gamma]/N[\Gamma]$, and $\nu^\alpha = \sum_{i=0}^{J} \nu_i^\alpha$. This expansion is valid when the spectrum depends on a linear combination of the parameters ϖ.

The normalization is defined so that the sum of all bins in the kinematic fiducial region is 1 for any combination of parameters $\Delta\varpi^\alpha \in \{\Delta\rho, \Delta\eta, \Delta\xi|_{\xi\delta}, \Delta\xi\delta\}$. The data is similarly normalized, and the data and simulation are used to generate the χ^2 statistic

$$\chi^2 = \sum_{i=}^{J} \frac{(n_i^{data} - n_i^{MC}(\varpi^\alpha + \Delta\varpi^\alpha))^2}{(\sigma_i^{data})^2 + (\sigma_i^{MC})^2} \tag{6.8}$$

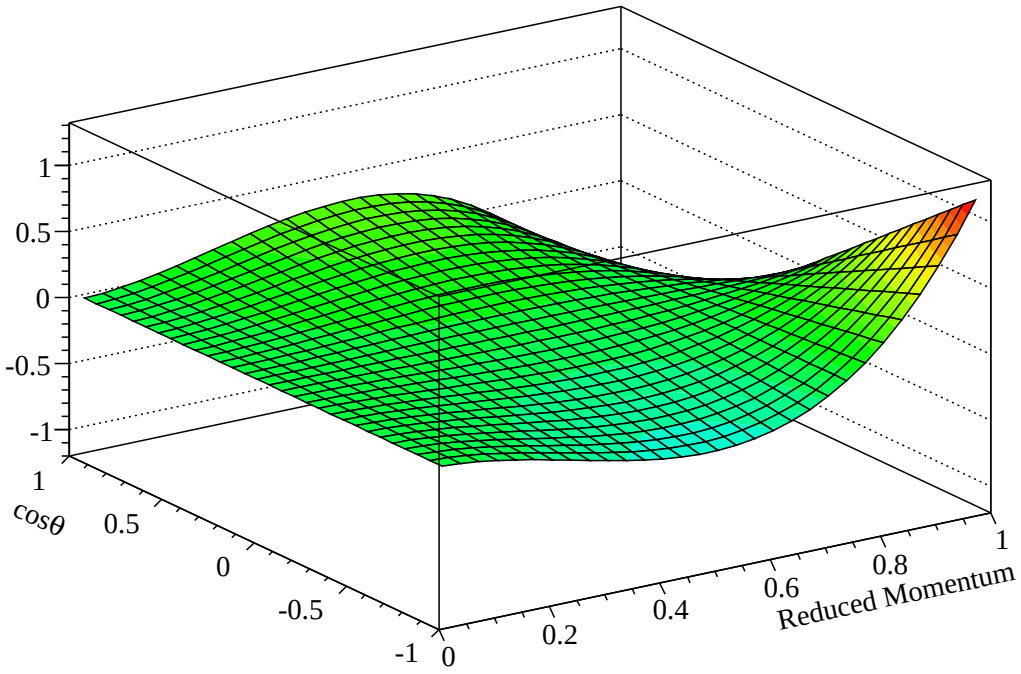

Figure 6.4: The theoretical $\xi\delta$ derivative spectrum in terms of the reduced momentum.

where n_i^{data} is the data contained in the ith fiducial bin, normalized so that the sum of fiducial bins is 1, and $\sigma_i^{data} = \sqrt{n_i^{data}}/N^{data}$ is the statistical uncertainty of the bin content. The chi-squared is minimized by altering the changes in the decay parameters $\Delta\varpi^{\alpha}$.

This fitting method is versatile. Data to data fits can be done if the spectrum expansion uses a data spectrum rather than a simulated spectrum as its base, assuming that a simulated spectrum is available to generate the efficiency, $\mathcal{E}$. Such fits are done for the purpose of determining systematic effects using the data. Systematics can also be determined using Monte Carlo to Monte Carlo fits where a simulation with a single condition altered is used in place of data. The code is optimized for usage with the muon decay parameters but additional derivatives and corresponding parameters can be added if needed if those parameters make a linear contribution to the spectrum. The η parameter is effectively fixed to the value used in the spectrum generation by not including its derivative in the calculation.

6.2 Endpoint Calibration

Although TWIST is a very well calibrated experiment, there are still differences between data and simulation that manifest singularly at the spectrum endpoint. The endpoint of the decay positron spectrum for a small range of angles is shown in Fig. 6.5. If the TWIST detector were perfect, with no momentum loss, and there were no reconstruction distortions, then it is expected that the kinematic endpoint of the muon decay spectrum should occur at a momentum $W_{e\mu} = 52.828$ MeV/c. Momentum loss and reconstruction effects mean that this momentum endpoint occurs at a variety of momenta depending the angle of the positron tracks contributing to the spectrum. Differences between data and the simulation at the endpoint can affect the measurement of the decay parameters by parts in 10^3. The precise effect of the endpoint calibration depends on how the the bulk spectrum is corrected using the endpoint difference.

6.2.1 Fitting method

The endpoint calibration (ECal) is a comparison of the data and Monte Carlo spectra at the endpoint completed in narrow slices of positron angles within the range $\cos\theta \in$

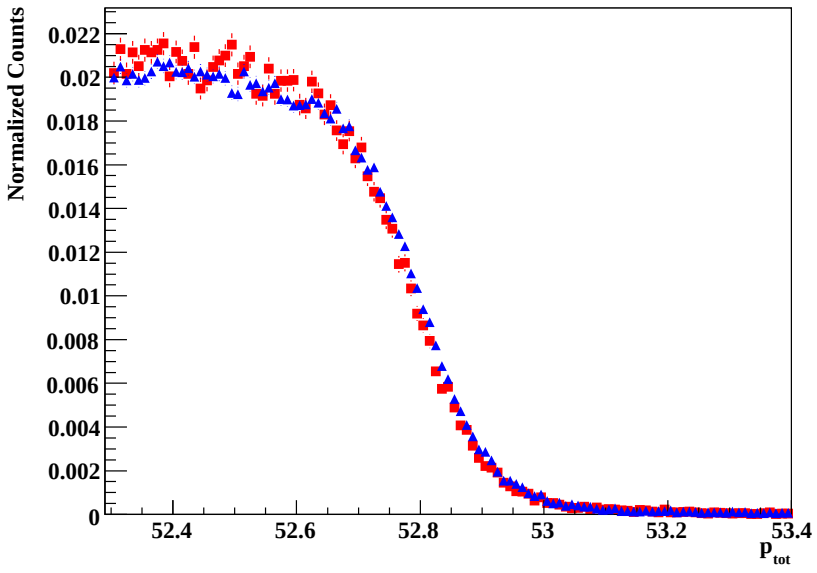

Figure 6.5: Spectra from data ■ and simulation ▲ before the endpoint calibration fit for positron angles such that -0.76 $\leq \cos\theta \leq$ -0.80.

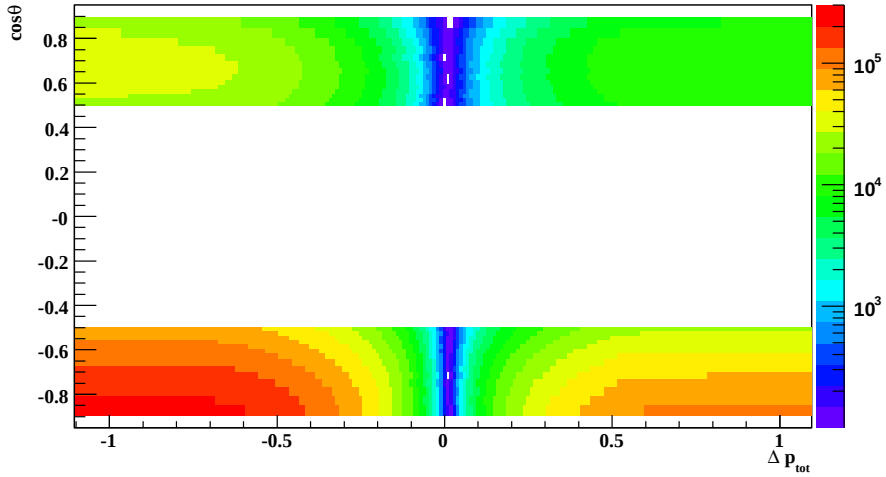

(a) χ^2 for all calculated changes in momentum Δp.

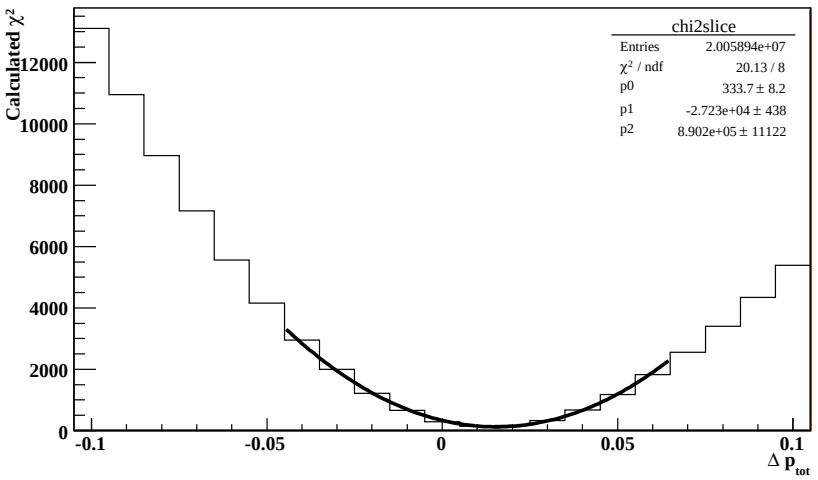

(b) Quadratic fit to the minimum 20 bins of the calculated χ^2.

Figure 6.6: χ^2 calculated from the difference between the data and the simulated momentum edges at angles such that $0.76 \leq \cos\theta \leq 0.80$.

$[0.5, 0.9]$. The momentum of the Monte Carlo spectrum is shifted by Δi discrete steps of 10 keV/c relative to the data spectrum. The difference between the data and the simulation are compiled for each step into a $\chi^2_{\Delta i}$ statistic.

$$\chi^2_{\Delta i} = \sum_i \frac{(n_i^{data} - n_{i+\Delta i}^{MC})^2}{(\sigma_i^{data})^2 + (\sigma_{i+\Delta i}^{MC})^2} \tag{6.9}$$

The surface generated by these calculated χ^2 values, as a function of the momentum change Δp and the positron $\cos\theta$, is shown in Fig 6.6a

The best offset to match the momentum calibration for the given range of angles is found by interpolating the $\chi^2_{\Delta i}$ function to its minimum value. The interpolation is required because the $\chi^2_{\Delta i}$ can only be calculated in discrete steps Δi, while the momentum offset, Δp, is a continuous variable. The interpolation is done in two stages; a quartic polynomial over a 200 keV range centred on the smallest calculated $\chi^2_{\Delta i}$, and a quadratic polynomial fit over a 100 keV range centred on the minimum found using the quartic fit. The momentum difference at the minimum χ^2 is the optimal offset value, while the uncertainty is defined by the region where $\chi^2 < \chi^2_{min}+1$. An illustration of this minimization procedure is shown in Fig 6.6b.

This method is a one parameter fit of the momentum offset. However, both the reconstruction resolution at the momentum edge and the relative normalization of the data and the simulation can affect these results. The resolution of the momentum reconstruction is known to be consistent between data and Monte Carlo simulation, with an uncertainty of 2 keV/c compared to the momentum resolution at the endpoint which is known to behave as $\sigma = \sigma_0/\sin\theta$ where $\sigma_0 = 60keV/c$ so that $\sigma \in [70, 175]$ keV/c in the fiducial region. The normalization on the other hand is different between data and Monte Carlo simulation and must be corrected.

There are two sources of normalization differences between data and simulation at the endpoint; the total number of counts in the source histograms, and the endpoint asymmetry of the spectrum. The endpoint histograms for both data and Monte Carlo simulation are normalized by the total number of counts in the fiducial region of the positron spectrum. Differences in the asymmetry of the positron spectrum change the relative normalization in a given range of angle as a function of $1-(P_\mu\xi\delta/\rho)\cos\theta$. Since the difference in the decay parameters between data and simulation can be as large as 1%, the decay parameters can make significant changes of as much as 2% in the number of counts of the downstream spectrum endpoint. This difference is corrected by running the `mcfitter` code to generate an estimate of $\Delta\rho$, $\Delta\delta$, and $\Delta P_\mu\xi$ before the application of energy calibration. The derivative spectra, weighted by the best fit decay parameters, are added to the base Monte Carlo spectrum used in the endpoint fit. This "raw", or initial, decay parameter fit is sufficient to produce a meaningful endpoint calibration.

Tests were completed which fixed the decay parameters used in the ECal to the values measured after the calibration is applied to the spectrum. The change in the

endpoint parameters was measured to be less than 1 keV/c, which produce changes less than 10^{-5} in the muon decay parameters. This calculation was performed analytically using the sensitivities shown in Table 6.1 and confirmed by applying the corrected ECal to the tree analysis. Because these changes are less than the statistical uncertainties of the decay parameter fits, the uncalibrated approximation of the decay parameters is sufficient for the determination of the final endpoint calibration.

This procedure is repeated for narrow bins with widths constant in $1/\cos\theta$ within the range of $0.5 < |\cos\theta| < 0.9$. The momentum offsets determined by this series of uncorrelated fits are fit with a function linear with respect to $1/\cos\theta$. The upstream and downstream momentum edges are fit separately using the following piecewise expression;

$$p_{data} - p_{MC} = \begin{cases} B_{up} + \dfrac{A_{up}}{\cos\theta} & \text{, if } \cos\theta < 0 \\ B_{dn} - \dfrac{A_{dn}}{\cos\theta} & \text{, if } \cos\theta > 0. \end{cases} \tag{6.10}$$

A subset of these fits are shown in Fig. 6.7.

The ECal parameters A_{up}, A_{dn}, B_{up}, and B_{dn} are used to calibrate the data spectrum to the simulated spectrum in a re-analysis of the root trees. The ECal parameters for all data sets appear in Fig. 6.8.

6.2.2 Application of the ECal to the Spectrum

The linear description of the endpoint provides a good first order approximation of the possible differences in the reconstruction between data and simulation. If there is a change in the total momentum loss between data and simulation an offset in the spectrum is expected with a net slope with respect to $1/|\cos\theta|$. If the simulated muon stopping distribution is significantly different then a net slope with respect to $1/\cos\theta$ might be measured at the endpoint. Both of these behaviours manifest as non-zero values of the endpoint parameters A_{up} and A_{dn}.

The source of the $\sec\theta$ independent difference at the endpoint, B_{up} and B_{dn} is not known but there are a few different models for the propagation of these parameters through the spectrum. One model treats these parameters as an offset in the positron spectrum that is potentially different for the upstream and downstream detectors. In effect this is subtracting Eq.6.10 from the reconstructed momentum in data to get a

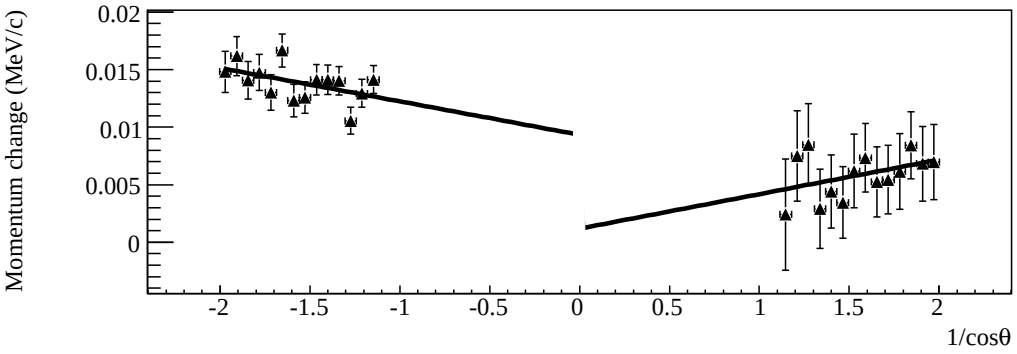

(a) Momentum edge difference from nominal silver data (set74) and simulation

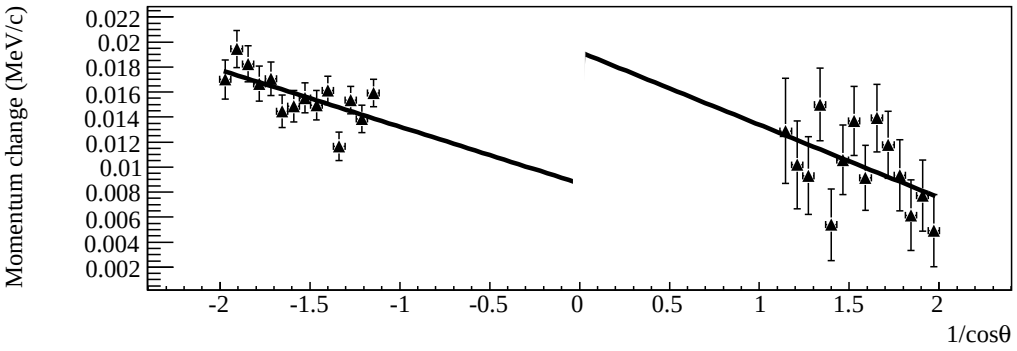

(b) Momentum edge difference from nominal aluminum target data (set84) and simulation

Figure 6.7: Differences in the momenta of the endpoint between data and simulation in silver and aluminum target data. The black solid lined indicate the piece-wise fit used for the calibration of the data to the simulation.

momentum calibration to the Monte Carlo simulation;

$$p_{cal} = \begin{cases} p_{data} - B_{up} - \dfrac{A_{up}}{\cos\theta} & , \text{ if } \cos\theta < 0 \\ p_{data} - B_{dn} + \dfrac{A_{dn}}{\cos\theta} & , \text{ if } \cos\theta > 0. \end{cases} \tag{6.11}$$

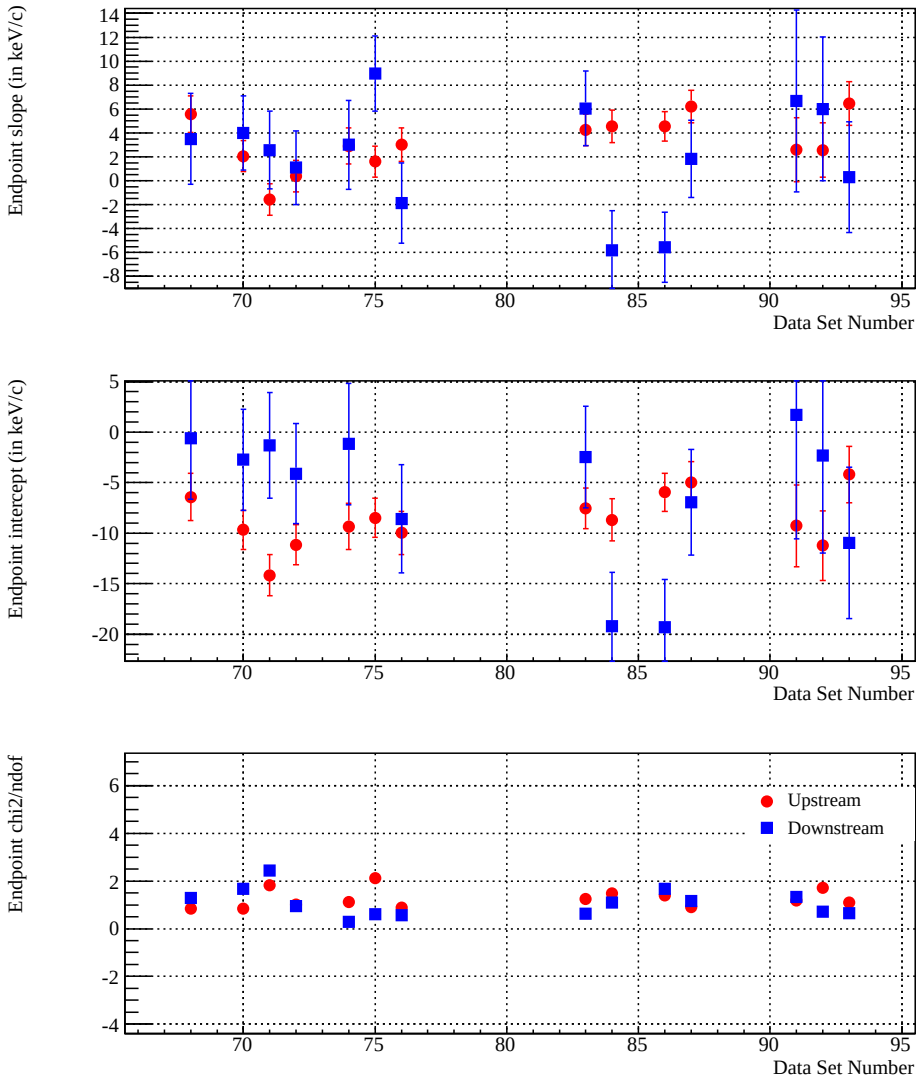

Figure 6.8: ECal parameters determined for the data sets used for the ρ measurement. The parameters, A_{up} and A_{dn} describing the slope with respect to $1/|\cos\theta|$ are shown in the top panel, while the intercepts, B_{up} and B_{dn} are shown in the middle panel. The bottom panel shows the reduced χ^2 for all of the upstream and downstream linear fits. Upstream and downstream parameters are marked using the same symbols for all panels.

This is consistent with a difference in the momentum loss that is constant with respect to momentum and an offset in the spectrum that is an artifact of reconstruction. A source for this artifact has not been found to date.

A second model considers the parameters B_{up} and B_{dn} as differences in the magnetic field or detector geometry. The changes are anticipated to produce a multiplicative change in the reconstructed momentum. The $\sec\theta$ behaviour at the endpoint may be likewise dependent on the momentum. An alternative model to Eq.6.11 for the application of the endpoint calibration to the spectrum was defined;

$$p_{cal} = \begin{cases} \dfrac{p_{data}}{1+\frac{1}{W_{e\mu}}(B_{up}+\frac{A_{up}}{\cos\theta})} & \text{, if } \cos\theta < 0 \\ \dfrac{p_{data}}{1+\frac{1}{W_{e\mu}}(B_{dn}-\frac{A_{dn}}{\cos\theta})} & \text{, if } \cos\theta > 0 \end{cases} \tag{6.12}$$

where $W_{e\mu} = (m_{mu}^2 + m_e^2)/2m_\mu = 52.828$ MeV/c. Eq.6.12 is consistent with Eq.6.11 if one considers the first order Taylor expansion,

$$p_{cal} = p_{rec} - \frac{p_{data}}{W_{e\mu}}\left(B_i - \frac{A_i}{|\cos\theta|}\right). \tag{6.13}$$

At the spectrum endpoint $W_{e\mu} = p_{data}$ and $p_{cal} = p_{rec} - B_i + \frac{A_i}{|\cos\theta|}$ or $p_{cal} = p_{rec} - \Delta p$. This approximation is good to a precision $(B_i/W_{e\mu})^2$, or $(2\times10^{-4})^2 = 4\times10^{-8}$. The typical uncertainties of the endpoint calibration is $\sigma_{B_{up}}/W_{e\mu} = 5\times10^{-5}$ and $\sigma_{B_{dn}}/W_{e\mu} = 1\times10^{-4}$

With a fractional uncertainty in the magnetic field map of 2.5×10^{-5} and a known error in the magnetic field yielding a fractional deviations of 1×10^{-4} it is not reasonable that the magnetic field should be responsible for the typical 10 keV/c values of $B_{up,dn}$. A secondary model for the calibration of the data was assumed where the data spectrum has an overall offset Δp relative to data, or $p_{cal} = p_{data} - B_i + A_i/|\cos\theta|$. Such a constant momentum offset is suggested to be an artifact of the reconstruction differences between data and simulation related to the derivation of the STRs, time zeros, etc., but nothing has been conclusively proved. It is assumed that the real momentum calibration of the positron spectrum is intermediate between an offset of the momentum scale and the correction shown in Eq. 6.12. This is treated as a systematic uncertainty in the analysis.

ECal sensitivities assuming a shifting model			
	ρ (MeV/c^{-1})	δ (MeV/c^{-1})	ξ (MeV/c)$^{-1}$
A_{up}	0.0136	0.0887	-0.1057
B_{up}	-0.0093	-0.0649	0.0800
A_{dn}	0.0309	-0.0400	-0.0020
B_{dn}	-0.0258	0.0306	0.0063

ECal sensitivities assuming a scaling model			
	ρ (MeV/c^{-1})	δ (MeV/c^{-1})	ξ (MeV/c)$^{-1}$
A_{up}	-0.0051	0.0887	-0.1162
B_{up}	0.0049	-0.0649	0.0882
A_{dn}	0.0309	-0.0503	0.0285
B_{dn}	0.0204	0.0306	-0.0145

Table 6.1: Sensitivities of the muon decay parameters to the endpoint calibration parameters assuming two different applications of the momentum calibration to the momentum spectrum. The case where the momentum calibrations is applied as a model independent shift in the momentum spectrum is shown at the top, while the case where the endpoint calibration is applied as a momentum dependent alteration of the momentum scale is shown at the bottom.

6.2.3 Statistical Uncertainties from Fitting Procedure

While the uncertainty in the decay parameter fits is derived directly from the fit, the uncertainty of the muon decay parameters due to statistical error of the endpoint calibration must be calculated separately, as an exercise in error propagation. The two sets of statistical uncertainties must be added in quadrature on a set by set basis before the averaging of the decay parameters is completed. The uncertainty in the energy calibration parameters, $q_\gamma \in \{A_{up}, B_{up}, A_{dn}, B_{dn}\}$, is converted into an uncertainty in the decay parameters, $p_\alpha \in \{\rho, \xi, \delta\}$, using the tensor expression,

$$V_{\alpha\beta}^{MP} = \frac{\partial p_\alpha}{\partial q_\delta}\frac{\partial p_\beta}{\partial q_\gamma}V_{\gamma\epsilon}^{EC} \tag{6.14}$$

where $V_{\alpha\beta}^{MP}$ is the covariance matrix calculated for the muon decay parameters, and $V_{\gamma\epsilon}^{EC}$ is the covariance matrix determined for the endpoint parameters. The decay parameter sensitivities, $\partial p_\alpha/\partial q_\gamma$, are calculated by altering an endpoint calibration parameter by Δq_γ, and measuring the resulting change in the decay parameters, Δp_α.

The endpoint calibration sensitivities are shown in Table 6.1 for the shifted and

(Units of 10^{-4})	Scaled Ecal			Shifted Ecal			Averaged Ecal		
Data set	$\Delta\rho$	$\Delta\delta$	$\Delta\xi$	$\Delta\rho$	$\Delta\delta$	$\Delta\xi$	$\Delta\rho$	$\Delta\delta$	$\Delta\xi$
68	0.27	0.8	0.4	0.28	0.7	0.39	0.27	0.75	0.4
70	0.22	0.67	0.33	0.23	0.58	0.32	0.23	0.62	0.33
71	0.23	0.69	0.34	0.24	0.6	0.33	0.23	0.64	0.34
72	0.22	0.67	0.33	0.23	0.58	0.33	0.23	0.62	0.33
74	0.26	0.79	0.39	0.27	0.68	0.38	0.27	0.74	0.39
75	0.23	0.68	0.33	0.24	0.59	0.33	0.23	0.63	0.33
76	0.24	0.72	0.36	0.25	0.62	0.36	0.25	0.67	0.36
83	0.24	0.71	0.35	0.25	0.61	0.35	0.24	0.66	0.35
84	0.24	0.73	0.36	0.25	0.63	0.36	0.25	0.68	0.36
86	0.22	0.66	0.33	0.23	0.57	0.33	0.23	0.62	0.33
87	0.24	0.73	0.36	0.25	0.63	0.36	0.25	0.68	0.36
91	0.5	1.51	0.66	0.52	1.3	0.67	0.51	1.4	0.66
92	0.4	1.21	0.56	0.42	1.04	0.56	0.41	1.12	0.56
93	0.32	0.95	0.45	0.33	0.82	0.45	0.32	0.88	0.45

Table 6.2: The uncertainties in the muon decay parameters due to the endpoint calibration uncertainties calculated for each data set under the assumption of scaled and shift momentum calibrations. The averaged result is added in quadrature to the mcfitter uncertainties for the decay parameters.

scaled calibrations. The uncertainties calculated using Equation 6.14 are shown in Table 6.2. The total statistical uncertainty is then the quadratic sum of the measured statistical errors and the base statistical uncertainty of the muon decay parameters determined by MINUIT in the `mcfitter`.

The ratio of $\Delta p_\alpha / \Delta q_\gamma$ is shown to be a good estimate of the differential sensitivity by directly testing the propagation of the parameters that result from changes in the ECal parameters. The changes measured in the decay parameters after the ECal is applied to the data spectrum match the changes that can be anticipated from

$$\Delta p_{alpha} = \sum_{\gamma} \frac{\partial p_\alpha}{\partial q_\gamma} \Delta q_\gamma. \tag{6.15}$$

The fractional deviation between the predicted changes in the decay parameters and the measured changes in the parameters are on the order of 1% for the shifted calibration and 10% for the scaled calibration. The averaged results are summarized in Table 6.3, demonstrating the strength of the assumption of linearity in the decay parameter sensitivities. The larger deviation in the scaled calibration can be understood

Dk. Par.	Meas. Change			Calc. Change	Abs. Dev.	Rel. Dev.
Units of 10^{-4}	Shifted Calibration					
ρ	3.32	$\pm$	0.89	3.29	-0.03	-0.01
δ	6.04	$\pm$	1.60	6.03	-0.0082	-0.0013
ξ	-10.66	$\pm$	3.50	-10.69	-0.031	0.003
	Scaled Calibration					
ρ	1.34	$\pm$	0.89	1.13	-0.20	-0.15
δ	3.84	$\pm$	1.60	4.14	0.302	0.10
ξ	-9.83	$\pm$	3.50	-10.01	-0.176	0.017

Table 6.3: The average differences of the decay parameters before and after the ECal is applied using both calibration modes. These numbers were compared to the average difference predicted from Equation 6.15, to produce an average absolute deviation and the relative deviation (absolute deviation divided by the average change in the decay parameters). This shows the linearity of the measured ECal sensitivities stated in Table 6.1.

in terms of the larger non-linearity of that mode of the ECal.

6.3 A Potential Bias in the Fitting Technique

The endpoint calibration and the `mcfitter` procedures both suffer from a bias due to the assumption of a χ^2 statistic for the comparison of two histograms. The uncertainties of the input for the fitting procedures are derived using Poisson statistics which are bound at the lower limit by zero. This bound introduces a potential bias in the χ^2 calculation as the joint distribution that results from the difference of two Poisson generated random variables will approximate a Gaussian with a skew which depends on the relative number of counts between data and simulation. The bias manifests so that the χ^2 minimization under-weights low statistics bins, which will create a positive bias in the measurement of ρ and $P_\mu\xi$ when there are less counts in the data than the Monte Carlo simulation. Evidence for this bias is shown in Fig. 6.9.

A likelihood approach to find the optimum values of the decay parameter differences is not viable as the effective fitting function is a binned distribution generated from the simulation and not a smooth distribution. This means that the probability function must treat the simulation as a random variable as well as the data. Such an extended likelihood function has been described by Barlow and Beeston[38], but

	MCfit bias (Units of 10^{-4})			ECal fit bias (Units of 10^{-4})		
Set Number	ρ	δ	$P_\mu\xi$	ρ	δ	$P_\mu\xi$
68	-0.21	-0.06	-0.54	-1.2	-0.5	2.16
70	-0.12	-0.03	-0.31	-1.07	-0.45	1.93
71	-0.14	-0.04	-0.36	-1.11	-0.46	1.99
72	-0.11	-0.03	-0.29	-0.99	-0.41	1.77
74	-0.22	-0.06	-0.57	-1.27	-0.53	2.27
75	-0.12	-0.03	-0.31	-1.04	-0.43	1.87
76	-0.17	-0.04	-0.43	-1.16	-0.48	2.07
83	-0.11	-0.03	-0.28	-0.93	-0.39	1.67
84	-0.13	-0.04	-0.34	-1.01	-0.42	1.81
86	-0.07	-0.02	-0.18	-0.73	-0.31	1.32
87	-0.12	-0.03	-0.32	-0.98	-0.41	1.77
91	-0.59	-0.16	-1.53	-1.19	-0.5	2.13
92	-0.47	-0.13	-1.23	-1.25	-0.52	2.24
93	-0.20	-0.05	-0.52	-0.92	-0.38	1.65
Average	-0.20	-0.05	-0.52	-1.06	-0.44	1.9

Table 6.4: The biases in the decay parameters due to unequal statistics in data and simulation determined for all data sets. These biases were used to correct the decay parameters.

was not known before the box opening. It was decided, at that time, that the best approach was to use the available method and quantify the bias.

To estimate the magnitude of this bias, a series of fits were done between two uncorrelated simulations. Subsets of one of the simulations was used in place of the data set for the `mcfitter`. As the fraction of counts in the data decreases relative to the Monte Carlo simulation, the measured decay parameters increase. A similar trend has been observed in the endpoint calibration.

These behaviours were quantified with the effort of Anthony Hillairet. The bias in the decay parameters resulting from unequal statistics in the ECal input is shown in Table 6.4. The bias in the endpoint calibration is much more significant and was used to correct the decay parameters for the final reported measurement.

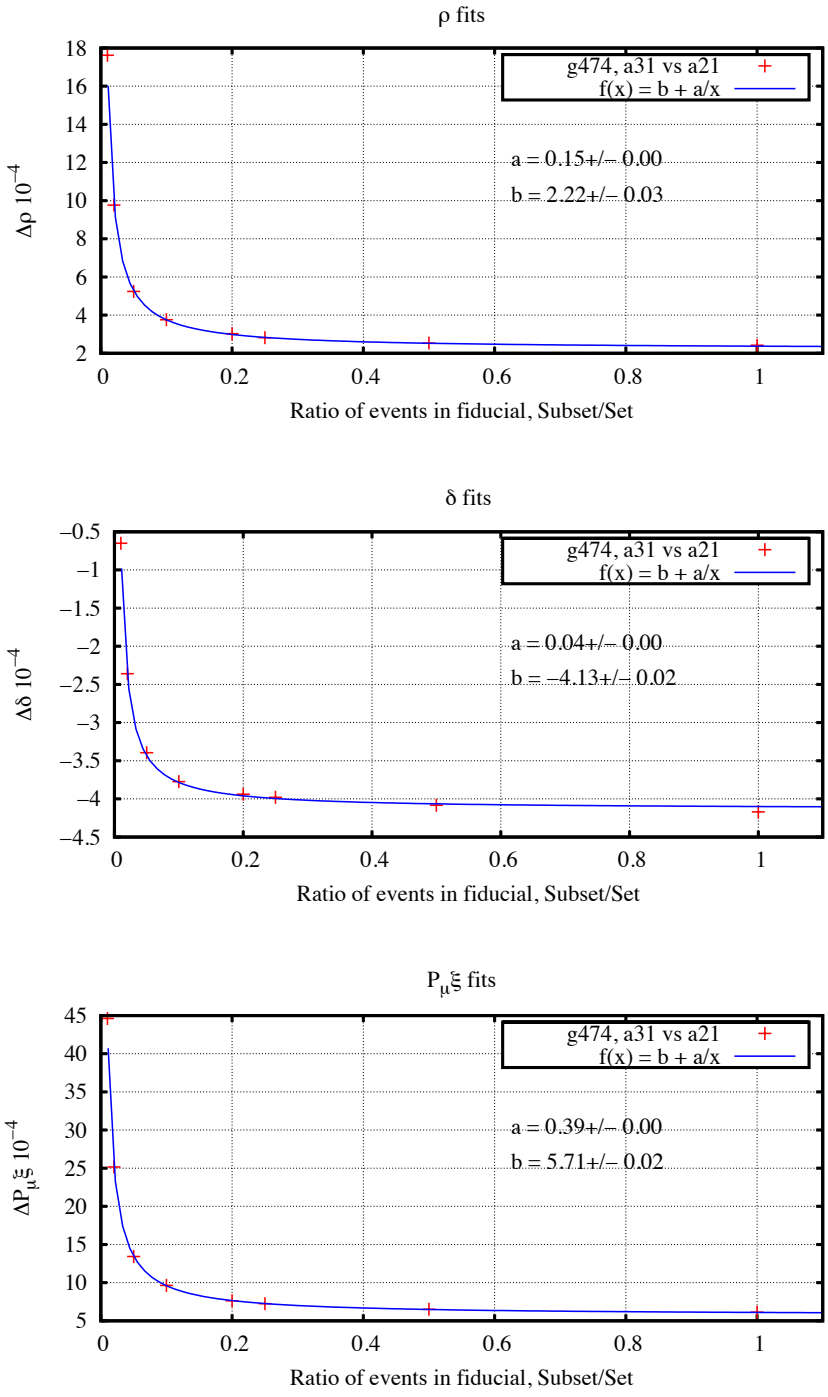

Figure 6.9: The bias in the muon decay parameters produced by repeated fitting subsets of a simulation of increasing size to an uncorrelated simulation. The abscissa is the number of counts in the subset divided by the number of counts in the uncorrelated simulation.

Chapter 7

Systematics

TWIST is a systematics limited experiment. The systematics were determined, in general, by altering a condition in the analysis of data or simulation, or in the generation of the simulation, and fitting the altered spectrum to a spectrum under nominal conditions. The sensitivity to the systematic effect is defined to be the change in the muon decay parameters that results from the exaggerated condition. The factor by which the condition is exaggerated compared to the expected uncertainty is the scaling factor for the sensitivity. The final systematic is the decay parameter sensitivity divided by the scaling factor.

An issue in the measurement of the systematics is that very few have sensitivities that are significant with respect to their base statistical uncertainties. The impact of this problem is minimized by using correlated data (or Monte Carlo simulation) sets; that is two sets of events where the decay momentum vectors are the same for all events. Correlation is achieved in data by analyzing the same data using two different sets of analysis conditions. In Monte Carlo this is achieved by using the same sets of randomly generated samples of events under different simulation conditions. This reduces the uncertainty related to statistical scatter from the parameter uncertainties so that only the changes in the spectrum introduced by the systematic effect itself alter the decay parameters. To correct the measured uncertainties, which are severely overestimated due to the correlations, the uncertainties were renormalized by noting that the statistical uncertainty of the muon decay parameters is defined by the parameter values that make $\chi^2 = \chi^2_{min} + 1$ when the reduced χ^2 is near 1. When the reduced χ^2 is much less than 1 this standard assumption for the parameter uncertainties is not valid and may be corrected by renormalizing the uncertainties by a factor of $\sqrt{\chi^2/ndf}$. Table 7.1 shows a summary of the systematic uncertainties for

ρ Systematics Category	Systematic Uncertainty ($\times 10^{-4}$)
Positron interactions	
Bremsstrahlung rate	-1.78
Delta ray rate	-0.07
Outside material	-0.48
Resolution	
Energy	-0.56
Angle	-0.06
Momentum calibration	
"ecmc" Model Uncertainty	0.58
Field Map	0.09
Energy Loss Dependence	1.02
Spectrometer alignment	
U/V width scale	-0.10
Z length scale	-0.18
Chamber response	
STRs (time-independent)	-0.31
Foil position (geometric effect)	0.80
US-DS Efficiency Asymmetry	0.20
cross talk	-0.50
t0 variations	0.09
Beam Stability	
Muon Beam Intensity	0.16
External Uncertainties	
Radiative Corrections	-0.81
Uncertainty in η	1.05
Polarization	
PsPact cut	0.22
Total Systematic	2.78

Table 7.1: Main systematics for the Michel parameter ρ.

ρ. These systematics will be described in the remainder of this chapter.

7.1 Positron Interactions

The difference of the positron interactions between data and simulation represent an important systematic in the measurement of the muon decay parameters. Because these interactions are written as part of the `GEANT 3` framework[34], which was not altered for the sake of this experiment, the uncertainties of these interactions must

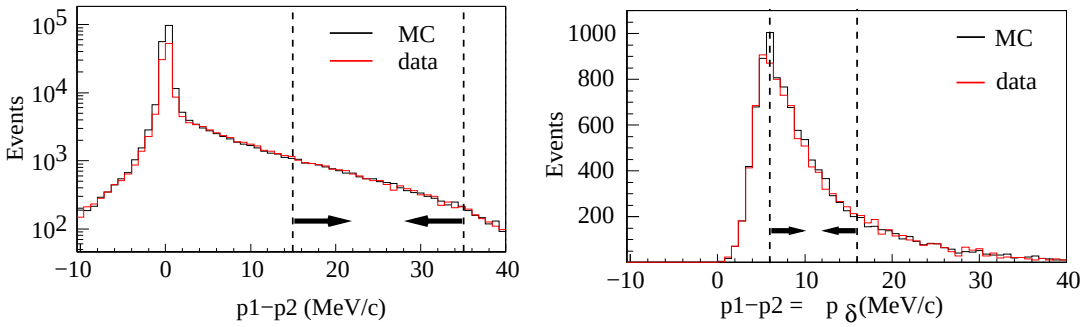

(a) Momentum lost by broken tracks.

(b) Momentum lost by events where there is a reconstructed delta ray present

Figure 7.1: Histograms of the momentum difference between two halves of a track broken by the First Guess pattern recognition algorithm. The accumulated counts in these histograms are used to quantify the positron interaction systematic. The ranges used to define the bremsstrahlung rate (on the left) and the delta ray production rate (on the right) is shown. The figures are normalized so that the number of muons is the same in data and simulation.

be accepted in the total error budget.

The positron interactions can be separated into three categories; the soft continuous EM interactions of the positrons with the detector material, the production of gamma rays in bremsstrahlung processes, and the production of "knock on" electrons or delta rays that result from electron-positron scattering. The soft interactions are considered in the endpoint calibration, while uncertainties in the discrete energy loss processes of delta ray production and bremsstrahlung must be treated separately. In principle, variations in the material thickness are subsumed by the endpoint calibration, on the part of the soft energy loss effects, and by the scaling factors used for the hard energy loss systematics. The discrete interaction processes could be probed using the upstream stops, as discussed in Section 5.2, or by using the First Guess algorithm's ability to break positron tracks into two when the momentum loss between planes becomes too large. Distributions of momentum differences of momenta of broken tracks fit from decay positrons that originate in the target are shown in Fig. 7.1. These histograms show the momentum loss distributions on logarithmic and linear scales with the ranges from which the bremsstrahlung and delta ray rates were measured.

7.1.1 Bremsstrahlung Rates

Uncertainties in bremsstrahlung rates can cause deformations in the muon decay spectrum due to differing contributions from the high momentum loss tracks. This would cause changes in the muon decay spectrum that cannot be corrected by the momentum calibration as it does not strongly manifest at the endpoint edge of the momentum spectrum.

To test this effect the bremsstrahlung production cross section in GEANT was modified to vary the probability of generating a bremsstrahlung event at some point along the track. There is no direct method for making this change in the standard e614 GEANT other than turning off the bremsstrahlung production completely. However, a method of changing cross section by altering the GEANT code was found by altering the distance between the generation of successive bremsstrahlung event. This interaction distance is inversely proportional to the bremsstrahlung production cross section.

The sensitivity of the muon decay parameters to bremsstrahlung rates was measured by exaggerating the cross section by a factor of 3 in a simulation of muons stopping in silver. This assumption of linearity has been validated in the silver simulation by exaggerating the cross section by a factor of 2. This test indicated that the effect on the decay parameters does increase linearly as the cross section is increased. The change in the muon decay parameters between the exaggerated simulation and the standard simulation are shown in Table 7.2. There is minimal correlation between the exaggerated and the standard simulation in this case because the change in the bremsstrahlung rate alters the path of the simulated positron track to the extent that reconstructed spectra are no longer related in spite of using the same spectrum samples.

The scale of the systematic was measured by counting the number of tracks broken in their progress through the detector. Reconstructed tracks are known to be separated into two tracks if the momentum lost between consecutive U-V pairs exceeds 6 MeV/c. The difference between the momenta of the two reconstructed tracks appears in Fig.7.2. Only broken tracks with changes in momentum between 15 and 35 MeV/c were counted to determine the change in the bremsstrahlung rate to avoid contamination from delta ray events. The production rate is then defined to be, $R = N|_{p\in[15\text{ MeV/c},35\text{ MeV/c}]}/N_{total}$; the number of broken track events in the chosen range divided by the number of all broken track events. The scale factor was ob-

tained using the rate of bremsstrahlung in the boosted simulation, R_{boost}, the rate of bremsstrahlung in the standard simulation, R_{MC}, and the rate of bremsstrahlung in the data;

$$S_{brem} = \frac{R_{boost} - R_{MC}}{R_{data} - R_{MC}} \tag{7.1}$$

The scale factor, S_{brem}, was determined separately for silver and aluminum target data. The scale factor used for the systematic is the average between the two measurements since the data - Monte Carlo difference should be independent of the target material. The scale factors and the final systematic uncertainties are shown in Table 7.2.

An alternative method of determining the systematic scale is to use the ratio of counts in the momentum loss tails as measured from the upstream stops to determine changes in the bremsstrahlung rate. The tail count rate for the upstream stops data and simulation was shown in Table 5.3. A simulation of 500000 upstream stopping muons was generated to find the number of counts in the momentum loss tail when the

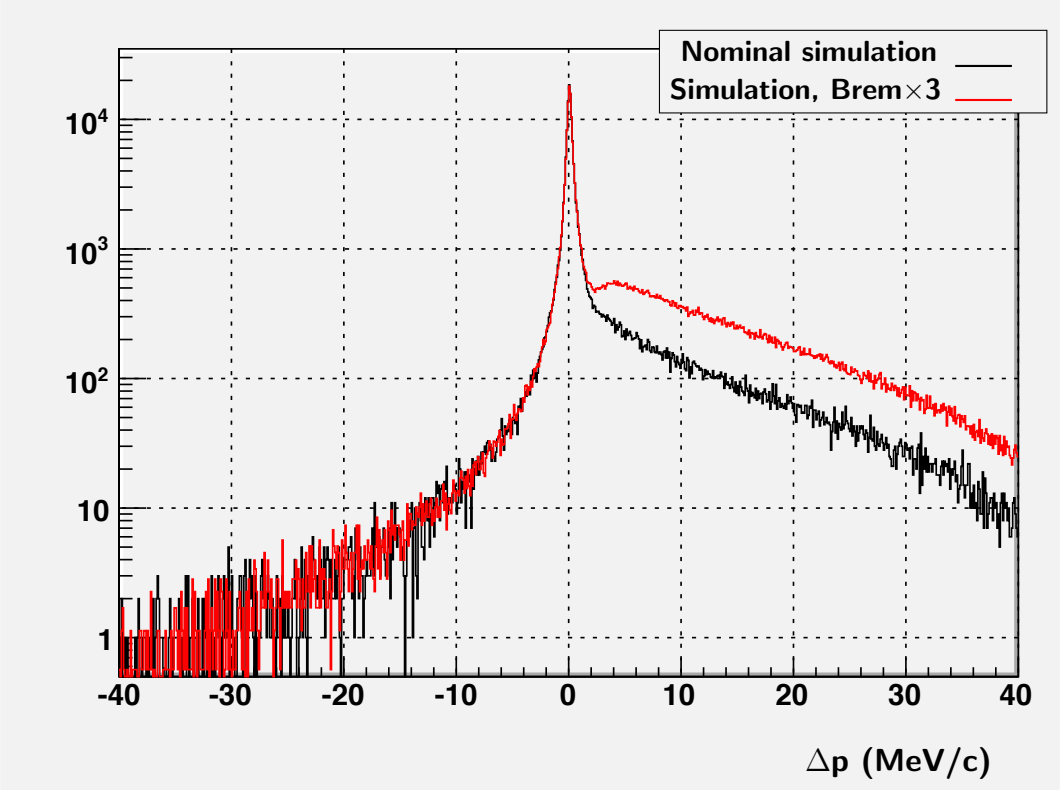

Figure 7.2: Momentum difference measured from broken tracks in MC. A simulation with the bremsstrahlung production enhanced by a factor of three is overlaid.

Raw Sensitivities ($\times 10^{-4}$)	
$\Delta\rho$	-148.1 $\pm$ 3.3
$\Delta\delta$	-132.8 $\pm$ 5.7
$\Delta\xi$	43.5 $\pm$ 7.0
Scale Factor	83.00
Scaled Fit Result ($\times 10^{-4}$)	
$\Delta\rho$	-1.78 $\pm$ 0.03
$\Delta\delta$	-1.60 $\pm$ 0.06
$\Delta\xi$	0.52 $\pm$ 0.07

Table 7.2: The raw and scaled results of the bremsstrahlung rate systematic.

	Broken Tracks		
	Silver	Aluminum	Average
R_{boost}/R_{MC}	3	3	3
R_{data}/R_{MC}	1.010 ± 0.012	1.035 ± 0.012	1.024 ± 0.008
$1/S_{brem}$	0.005	0.017	0.012
	Upstream Stops		
R_{boost}/R_{MC}	2.54 ± 0.02	2.66 ± 0.02	2.60 ± 0.014
R_{data}/R_{MC}	0.99 ± 0.01	0.96 ± 0.02	0.98 ± 0.01
$1/S_{brem}$	-0.0036	-0.023	-0.015

Table 7.3: Derivation of the bremsstrahlung scale factors from the accumulated target stops data via broken tracks and the upstream stops data.

$R_{\delta\times3}/R_{MC}$	3
R_{Data}/R_{MC}	1.007 ± 0.009
S_δ	286

Table 7.4: Counts identified as delta rays in the range 6 MeV/c $< p_\delta <$ 26 MeV/c for the two positron interaction exaggerated simulations divided by the delta ray counts identified in the nominal simulation.

bremsstrahlung rate was increased by a factor of 3. The results are basically identical to that found using the broken tracks, although this counting method considers effects from momentum loss across the target as well as across the active volume of the detector. The tail count ratios and their related scale factors are shown in Table 7.3

7.1.2 Delta ray Production

The production of delta rays is controlled in the same way as the bremsstrahlung production rate, and so the measurement of the decay parameter sensitivities to delta ray production is also completed in the same way. The effective cross section of delta ray production is increased by dividing the number of tracking steps between the production of consecutive delta ray events by a known boost factor. The delta ray production was exaggerated by a factor of 3 in a dedicated simulation, and the sensitivities were measured from the decay parameter fit between the dedicated simulation and a matching standard simulation.

The scale for the systematic was determined by searching for extra tracks in the reconstruction. When a delta ray is produced in the detector the electron can produce a track that may be reconstructed. Electron tracks can be identified as left handed

reconstructed helices. Only delta ray tracks with momenta greater than 6 keV can be reasonably reconstructed. This is a sufficient change in the track momentum to break the positron track in the event at the first guess level, yielding another method of identifying the event. To simplify the analysis, only events of type 1 and 2, described in Table 4.2 are considered. The momentum distribution of identified delta ray tracks are shown in Fig.7.3 for the standard simulation and the delta ray exaggerated simulation. The ratios of the number of identified delta tracks with momenta between 6 MeV/c and 26 MeV/c are shown in Table 7.4. The delta production rate in data was averaged over 7 data sets to reduce the uncertainty in the ratio between the data and Monte Carlo rates. In spite of this the delta ray production rates in data and simulation are consistent so the final systematic after scaling is very small. The raw fit of the exaggerated simulation to the standard simulation and the final uncertainties after scaling is shown in Table 7.5.

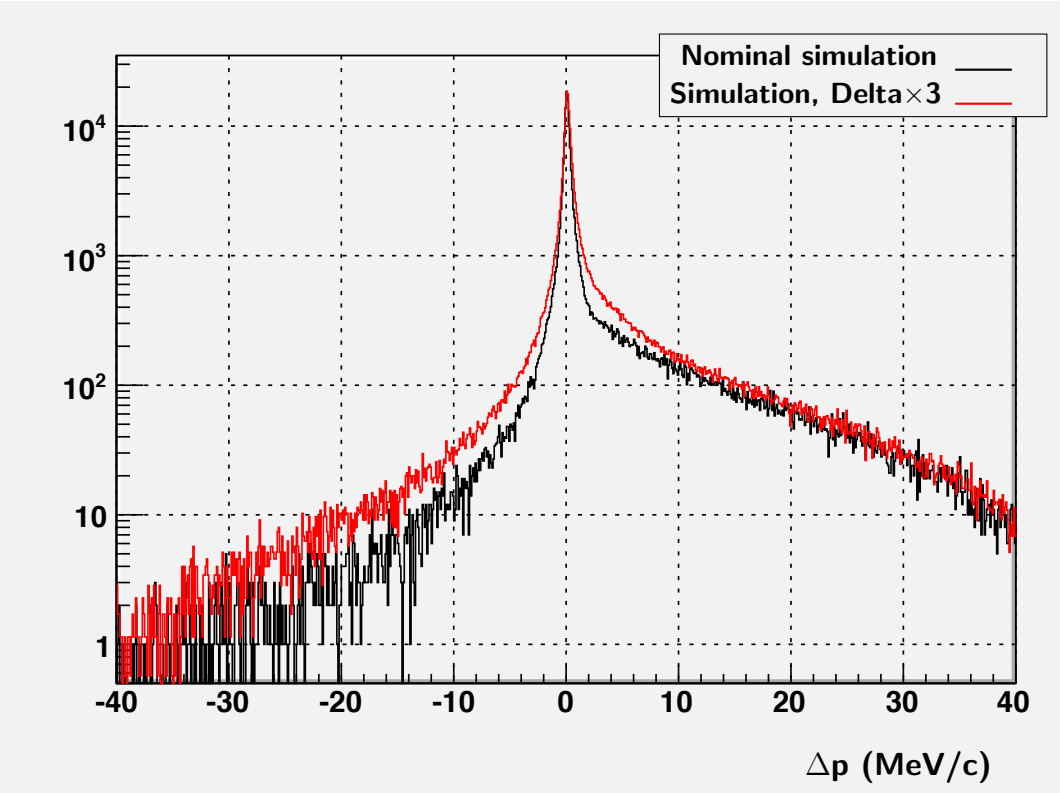

Figure 7.3: Momentum difference measured from broken tracks from MC. A simulation with the delta ray production enhanced by a factor of three is overlaid.

Raw Sensitivities ($\times 10^{-4}$)	
$\Delta\rho$	-19.7 ± 2.8
$\Delta\delta$	-16.3 ± 4.9
$\Delta\xi$	19.9 ± 6.0
Scale Factor	286.00
Scaled Fit Result ($\times 10^{-4}$)	
$\Delta\rho$	-0.07 ± 0.01
$\Delta\delta$	-0.06 ± 0.02
$\Delta\xi$	0.07 ± 0.02

Table 7.5: Systematic uncertainties for the production of delta rays as measured from a fit of a simulation with the delta ray production rate exaggerated by a factor of three to a standard Monte Carlo simulation. The results before and after the scaling factor is applied are shown.

7.1.3 Outside Material

Material immediately outside of the detector can scatter positrons back into the detector volume. This is a potential concern because such events can potentially alter the event classification as events that scatter off of material upstream of the detector stack will look like beam positron events. The tracks are terminated when they enter the yoke in the simulation preventing the production of particles back-scattering off of the yoke in simulation. This choice was made to address concerns that electromagnetic cascades in the steel would inflate the size of the output files. These cascades turned out to not be an issue, but this was found out after the full analysis was completed.

An estimate of the systematic effect was completed by Anthony Hillairet. The sensitivity was obtained by comparing simulations with and without the downstream beam package. Since both the upstream and downstream beam packages are properly simulated this estimate is valid in spite of the termination of the simulation at the yoke. To define the scale of the systematic the number of back-scattering particles was determined using the PC time of flight information of tracks with windows identified to contain beam positrons and decay positrons. Since the back-scatters should appear as beam positrons in the event classification, the rates of these event types will also be exaggerated by the introduction of the yoke. The results of this systematic are shown in Table 7.6.

Raw Sensitivities ($\times 10^{-4}$)	
$\Delta\rho$	-3.0 ± 2.0
$\Delta\delta$	0.8 ± 3.2
$\Delta\xi$	-2.4 ± 4.2
Scale Factor	6.3
Scaled Fit Result ($\times 10^{-4}$)	
$\Delta\rho$	-0.48 ± 0.32
$\Delta\delta$	0.13 ± 0.54
$\Delta\xi$	-0.38 ± 0.67

Table 7.6: The systematic results measured from the outside materials systematic.

7.2 Momentum Calibration

Small errors in the reconstruction of the spectrum can make significant changes in all of the muon decay parameters. Changes in the average calibration of the spectrum will preferentially alter the values of ρ while changes that affect one side of the detector over the other will affect the values in the asymmetry parameters, ξ and δ.

7.2.1 Calibration Model Uncertainties

The momentum calibration, described in Section 6.2 relies on the assumption that the simulation provides a good model for the shape of the spectrum at the endpoint. It further assumes that the behaviour of the differences between data and simulation are modelled as linear functions with respect to $1/\cos\theta$ upstream and downstream of the target. Both of these assumptions are potential sources of uncertainties for the momentum calibration. This systematic is not defined in the same way as the majority of the systematics. Instead a penalty on the ECal is assessed based on the poor χ^2 and the result is propagated into the decay parameters using the methods described in Section 6.2.3.

The averaged χ^2/ndf in the upstream ECal fit is 1.27. This was used to estimate an inflation of the uncertainties of the upstream momentum offsets of 1.6 keV/c assuming that there is a non-linearity in the endpoint difference that is not otherwise reflected by the systematics. The uncertainty is introduced as an uncorrelated uncertainty of both the upstream and downstream momentum edge, in addition to the statistical uncertainty on the ECal described in Section 6.2.3. The statistical uncertainties are roughly 2 keV/c for the upstream spectrum and 5 keV/c for downstream tracks.

Propagation of this expansion of the uncertainty to the muon decay parameters can be completed using the sensitivities in Table 6.1 using Eq.6.14, although a more precise determination was generated using a toy Monte Carlo model of the endpoint. These inflated uncertainties make a change in the value of $\sigma_\rho = 0.58 \times 10^{-4}$, $\sigma_\delta = 0.54 \times 10^{-4}$, and $\sigma_\xi = 1.38 \times 10^{-4}$. The larger uncertainty for ξ is understandable as the inflation of the uncertainty is proportionately larger for the upstream endpoint than the downstream endpoint.

7.2.2 Field Map Uncertainties

The magnetic field alters the overall momentum scale of the positron spectrum. Errors in the magnetic field can result from differences between the shape of the real and simulated magnetic fields, or differences in the scaling of the magnetic field. Deviations in the shape of the magnetic field are considered the more serious as errors in the magnetic field scale should be corrected by the ECal.

As stated in section 3.3.1 the difference of the shape of the measured magnetic field compared to the OPERA field map was parametrized in terms of corrections to the longitudinal magnetic field, B_z, and the radial field B_r using the parameters C_2, C_3, and C_r (see Eq. 3.1 and 3.2). The best fit parameters to the magnetic field differences are $C_2 = -1.7 \times 10^{-4}$, $C_3 = -8 \times 10^{-6}$, and $C_r = -0.0833$ [39]. The sensitivity of the muon decay parameters to the magnetic field shape was determined by analyzing a nominal data set (set84) with a magnetic field map corrected using Eq. 3.1 and 3.2 with the best fit parameters were multiplied by a factor of -19. This exaggerated set was then fit using the nominal analysis of the data as the base spectrum in the determination of the change in the decay parameters. The systematic scale factor is 20 for the measurement. The effect on the decay parameters for this systematic test are shown in Table 7.7.

Shape effects in the magnetic field produce changes in the endpoint calibration. The relative endpoint fit was carried out to calibrate the analysis using the standard magnetic field. This procedure removes effects from the systematic that are corrected by the endpoint calibration to avoid double counting systematic effects.

7.2.3 Momentum Dependence of Calibration

The propagation of the momentum calibration to the bulk of the muon decay spectrum cannot be determined a priori from the information available at the endpoint.

The method of propagating the momentum calibration into the data spectrum can make significant changes to the overall shape of the spectrum, which affect significant changes to the measurement of the muon decay parameters.

The behaviour of the upstream stops with respect to momentum was thought to be an indicator of this behaviour, as described in the 2006 thesis by Blair Jamieson [40]. However, the upstream stops can only determine the difference in the momentum scale between the upstream and downstream halves of the detector. Furthermore to relate this to the method of endpoint calibration, the difference between data and simulation extrapolated to the endpoint must be considered. This is described in Section 5.2.5. However these results should be compared with the most likely causes of a momentum dependence. For example the differences between the measured and OPERA field maps, this difference of upstream and downstream differences should be less than 2 keV/c at the endpoint; much less than the 5-10 keV/c observed in the upstream stops.

Since there is no known way of positively identifying the relationship of the endpoint calibration to the spectrum the average between the two limiting cases described in Section 6.2.2 are assumed for the application of the endpoint calibration. The endpoint calibration is applied to the data once for each of the two models. The reported decay parameters are assumed to be the average of the two results.

The systematic uncertainty for the effect is defined to be half of the average difference between the muon decay parameters measured from the different applications of the endpoint calibration. These differences are shown graphically in Fig.7.4. The systematic errors, derived from half of the average difference, are shown in Table 7.8.

Raw Sensitivities ($\times 10^{-4}$)	
$\Delta\rho$	1.8 ± 3.7
$\Delta\delta$	1.2 ± 6.4
$\Delta\xi$	5.0 ± 7.9
Scale Factor	20
$\sqrt{\chi^2/ndf}$	0.18
Scaled Fit Result ($\times 10^{-4}$)	
$\Delta\rho$	0.09 ± 0.03
$\Delta\delta$	0.06 ± 0.06
$\Delta\xi$	0.25 ± 0.07

Table 7.7: Systematic uncertainties in all three decay parameters that result from changes in the magnetic field shape.

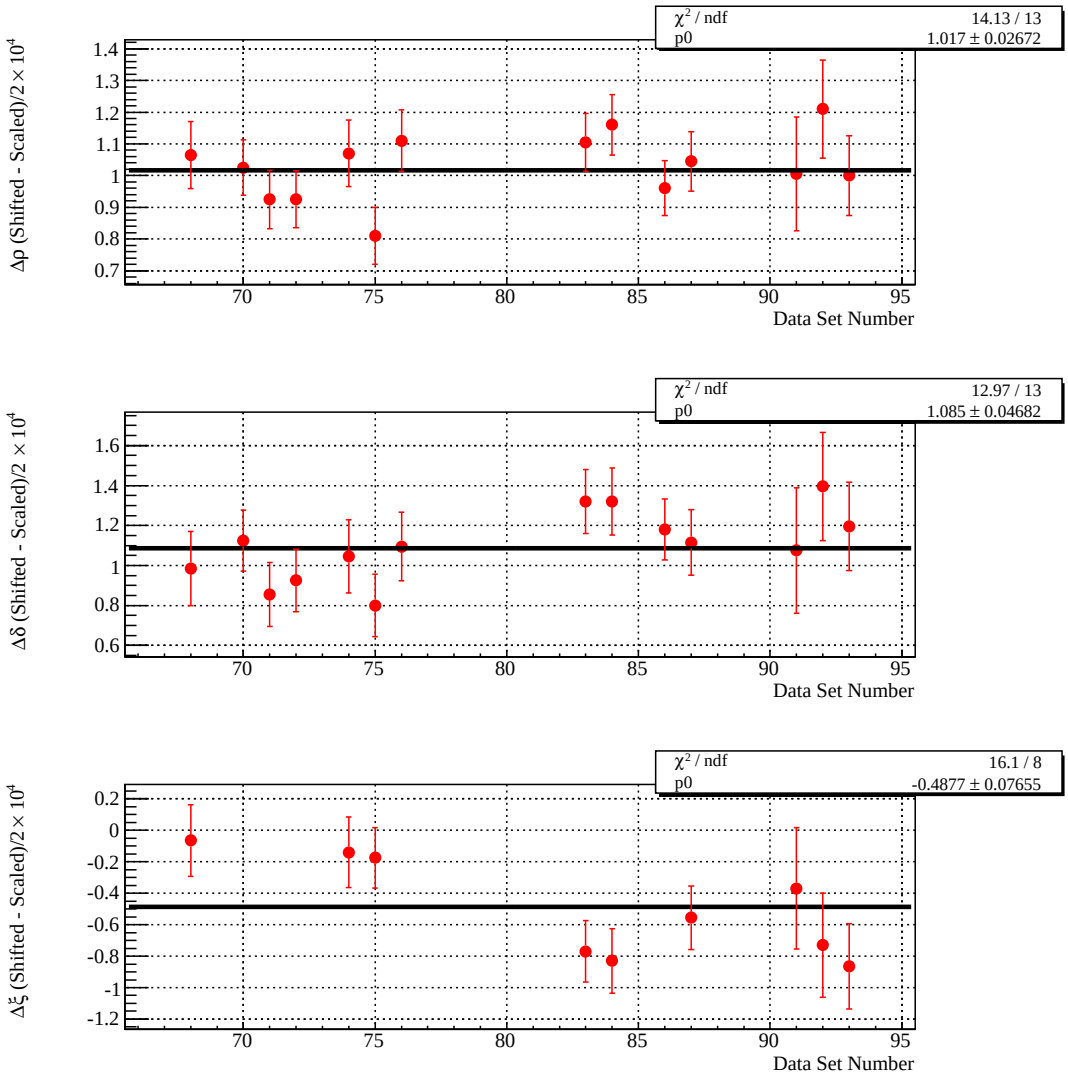

Figure 7.4: Half the difference in the muon decay parameters that result from changing the momentum dependence of the momentum calibration. The average over all data sets is shown by the black line. The error bars are reduced from the measured statistical uncertainties of the muon decay parameters to reflect the correlations between the decay parameters measured with the two different calibration modes by multiplying the errors bars by a factor of 1 minus the correlation.

If the source of the endpoint difference between data and simulation can be determined and quantified then this systematic can be reduced or eliminated. Attempts to do this in the context of the muons stopping in the target have failed due to the lack of a physical model that explains the observed behaviour of the detector system. One possible explanation that has not been fully explored is the relationship between the momentum calibration and the data calibrated STRs. It is not known how the STR calibration procedure biases the momentum scale in data and if the bias is different in data and simulation. If there had been more time to conduct experiments and perform computations, the relationship would have been investigated more fully.

7.3 Reconstruction Resolution

Differences in the resolution of the detector between data and Monte Carlo alter the results of the decay parameter fit by changing the endpoint calibration. The effect of the momentum resolution on the decay parameters is relatively small because the positron spectrum is very smooth with respect to momentum everywhere except at the endpoint where the momentum resolution becomes the defining feature. Similarly the fiducial cuts remove large angle positron tracks where the angular resolution becomes the defining feature.

Differences in momentum resolution between data and Monte Carlo simulation introduce biases in the momentum offsets determined by the endpoint calibration[41][42]. Any bias in the endpoint calibration is propagated through the decay spectrum when the momentum scale is calibrated. The momentum resolution difference between

Averaged Difference $\times 10^{-4}$	
$\langle \Delta\rho \rangle$	2.04
$\langle \Delta\delta \rangle$	2.16
$\langle \Delta P_\mu \xi \rangle$	-0.98
Scale Factor	2
$\sqrt{\chi^2/ndf}$	1
Scaled Fit Result ($\times 10^{-4}$)	
$\Delta\rho$	1.02
$\Delta\delta$	1.08
$\Delta P_\mu \xi$	-0.49

Table 7.8: Half of the average difference of the decay parameters between the shifted and scaled momentum calibrations.

modern data and simulation is less than the uncertainty in the existing measurements, so it was considered unnecessary to alter the endpoint calibration to match the resolution between the input spectra. The resolution of data and Monte Carlo as a function of $1/\sin\theta$ for various momenta are shown in Fig. 7.5. This is in contrast to the analysis of the 2004 data where there were significant differences between the data and Monte Carlo resolution, on the order of 5 keV/c, which necessitated a significant correction to the muon decay parameters.

The detector resolution must be determined from upstream stops data and simulation. The Δp and $\Delta\theta$ distributions were fit using a Gaussian function at a variety of momenta and angles. Because of the radius cut, some extrapolation must be done over the regions of poor occupancy.

The difference of resolution between data and simulation is consistent with zero so a limit on the squared difference of the momentum resolution, is set using

$$\delta\sigma = \begin{cases} \sqrt{\sigma_{data}^2 - \sigma_{MC}^2} & \text{if } \sigma_{data} > \sigma_{MC} \\ \sqrt{\sigma_{MC}^2 - \sigma_{data}^2} & \text{if } \sigma_{data} < \sigma_{MC} \end{cases} \tag{7.2}$$

such that $\delta\sigma < 11.5$ keV/c independent of angle. To exaggerate this difference, a random number X, sampled from a Gaussian distribution with a width of 5(11.5 keV/c) = 57.5 keV/c was added to the momentum of each track in the data during a special tree analysis. The resolution was similarly exaggerated for the angular resolution, where the difference is less than 1 milliradian, by a factor of five. The output spectrum was fit to the standard data spectrum to measure the sensitivity of the effect. The decay parameter sensitivities and the final systematic uncertainties are shown in Table 7.9.

7.4 Spectrometer Alignment

TWIST depends heavily upon the alignment of its components. The uncertainties in the decay parameters that result from the mechanical tolerances of the apparatus yield a negligible contribution to the total systematic error. Sensitivities of the translational and rotational misalignments were parts in 10^6 for all three decay parameters, with the largest uncertainty being for rho at 3×10^{-6}. For this reason these uncertainties were left off of the systematics table. However, sensitivities the detector length scale did make a significant contribution to the total systematic error.

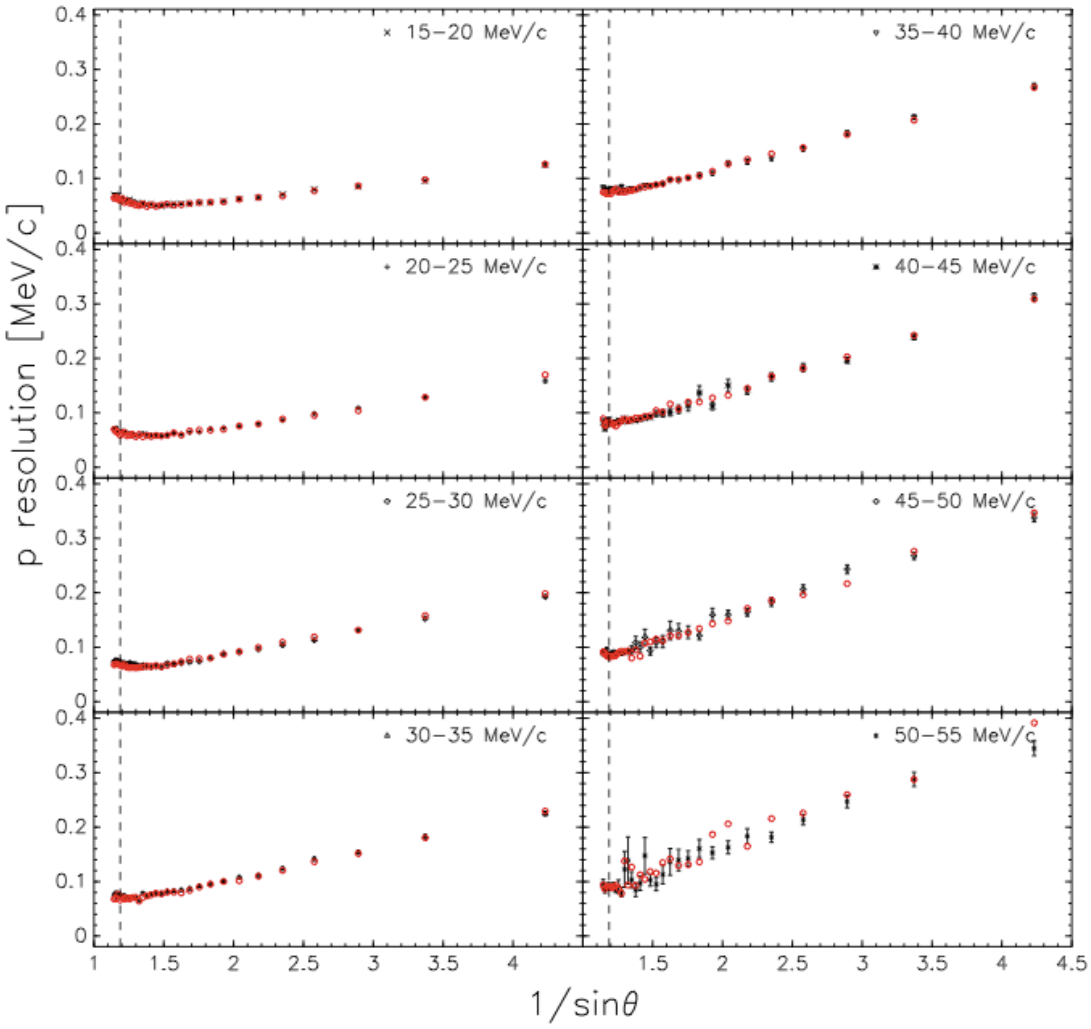

Figure 7.5: Momentum resolution measured from upstream stop in data and Monte Carlo simulation as a function of $\sin\theta$ for various momenta in silver data. The simulated points are shown in read and data points are shown in black.

	Raw Sensitivities ($\times 10^{-4}$)	
	Mom. Res.	Angle Res.
$\Delta\rho$	-2.8 ± 3.7	-0.3 ± 3.7
$\Delta\delta$	-3.5 ± 6.4	0.6 ± 6.4
$\Delta\xi$	7.6 ± 7.9	0.02 ± 7.9
Scale Factor	5	5
$\sqrt{\chi^2/ndf}$	0.30	0.38
	Scaled Uncertainties ($\times 10^{-4}$)	
$\Delta\rho$	-0.56 ± 0.22	-0.06 ± 0.28
$\Delta\delta$	-0.70 ± 0.39	0.12 ± 0.48
$\Delta\xi$	1.52 ± 0.48	0.04 ± 0.60

Table 7.9: Sensitivities and final systematic uncertainties in the muon decay parameters due to potential uncertainties of the momentum and angle resolution.

7.4.1 Detector Length Scales

One place where the alignment of the detector can produce changes in the positron spectrum is in the unlikely case that there are correlated errors in the length scales of the detector. The correlated uncertainties in the lengths in the U or V axes could be due to uncertainties in the ruler used to set the wire positions while uncertainties in the z-axis would come from uncertainties in the Sitall spacer thickness. Significant, correlated, errors in the relative positions of the drift planes along the z-axis will alter the measured longitudinal momenta of decay positrons, while correlated errors in the wire positions will alter the measured transverse momentum.

The sensitivity of this effect is measured by scaling p_z and p_t in a special tree analysis. To exaggerate the effect of potential correlated errors in the UV wire positions the transverse momenta were multiplied by a factor reflecting 50 times the fractional uncertainty of 2×10^{-5} or 1.001 [43]. The effect of poor positioning of the wire planes in z was duplicated by multiplying the longitudinal momentum of all decay positrons by a factor of 1.001, or one plus the fractional uncertainty of the accumulated Sitall ceramic spacer lengths, 5×10^{-5} multiplied by a factor of 20. The sensitivities of the muon decay parameters to this exaggeration are shown in Table 7.10.

	Raw Sensitivities ($\times 10^{-4}$)	
	UV scale	Z scale
$\Delta\rho$	-4.9 ± 2.4	-3.5 ± 2.4
$\Delta\delta$	-5.0 ± 4.2	-6.7 ± 4.2
$\Delta\xi$	7.8 ± 5.2	0.5 ± 5.2
Scale Factor	50	20
$\sqrt{\chi^2/ndf}$	0.19	0.20
	Scaled Uncertainties ($\times 10^{-4}$)	
$\Delta\rho$	-0.10 ± 0.01	-0.18 ± 0.02
$\Delta\delta$	-0.10 ± 0.02	-0.34 ± 0.04
$\Delta\xi$	0.16 ± 0.02	0.03 ± 0.05

Table 7.10: Sensitivities and scaled systematic uncertainties of the decay parameters to the changes in the length scales of the TWIST detector

7.5 Chamber Response

7.5.1 Cross talk

Cross talk is the appearance of false hits in the chambers produced by the appearance of a TDC pulse on one wire when the real hit took place on an adjacent wire. A correction is made in the analysis to reduce the influence of false hits in the detector at the MOFIA stage of the analysis. Cross talk hits are defined to be wire hits with a narrow TDC pulse width adjacent to wires with significant pulse widths. Cross talk does not exist in the Monte Carlo simulation, so its efficacy in the data must be evaluated and tested for distortions in the shape of the decay spectrum.

The effect that the cross talk has on the spectrum was measured by turning the cross talk correction off in the analysis and re-running it on a nominal data set. The raw results are shown in Table 7.11. The scaling factor was assigned to be 1 because the cross talk correction can only be on or off in the analysis. This systematic is poorly determined because there is no way of exaggerating the effect. In spite of the poor precision of this systematic measurement the central value of the systematic effect is assumed for the uncertainty to maintain consistency with the other systematic measurements. An improvement in the systematic uncertainty could be made if the cross talk removal can be reliably mimicked in the simulation. If this were so then the systematic effect of the false removal of cross talk hits would be reduced and the existence of cross talk hits could be exaggerated for a systematic measurement.

Renormalized Fit Result ($\times 10^{-4}$)	
$\Delta\rho$	-0.50 $\pm$ 0.71
$\Delta\delta$	0.10 $\pm$ 1.22
$\Delta\xi$	0.50 $\pm$ 1.51
$\sqrt{\chi^2/ndf}$	0.19

Table 7.11: The results of the decay parameter fit between an analysis of nominal aluminum target data with cross talk off and the standard analysis of the same data set. The uncertainties are renormalized according to the measured χ^2/ndf of the fit.

7.5.2 Time Independent Space Time Relationships

The systematic effect due to uncertainty in the time independent space time relationships was the leading systematic uncertainty for ρ in the previous measurement. The adoption of calibrated STRs for this experiment, as described in Section 4.3.3, has greatly reduced this contribution. The STRs used in data and those used in simulation are quite different as shown in Fig. 7.6. A difference in the time residuals used to derive the STRs averaged over all planes was considered to parametrize this change.

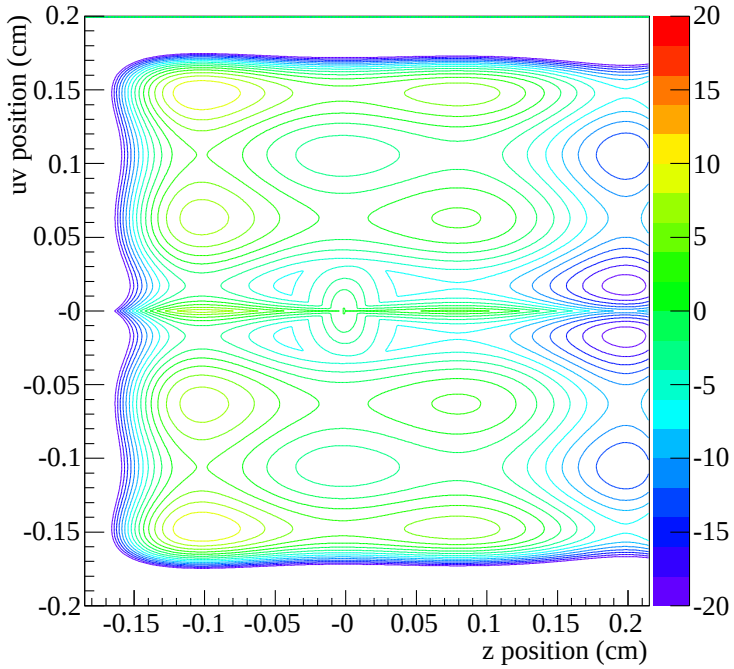

Figure 7.6: Difference between the STRs used for the exaggerated simulation and the standard simulation. Colour scale given in nanoseconds.

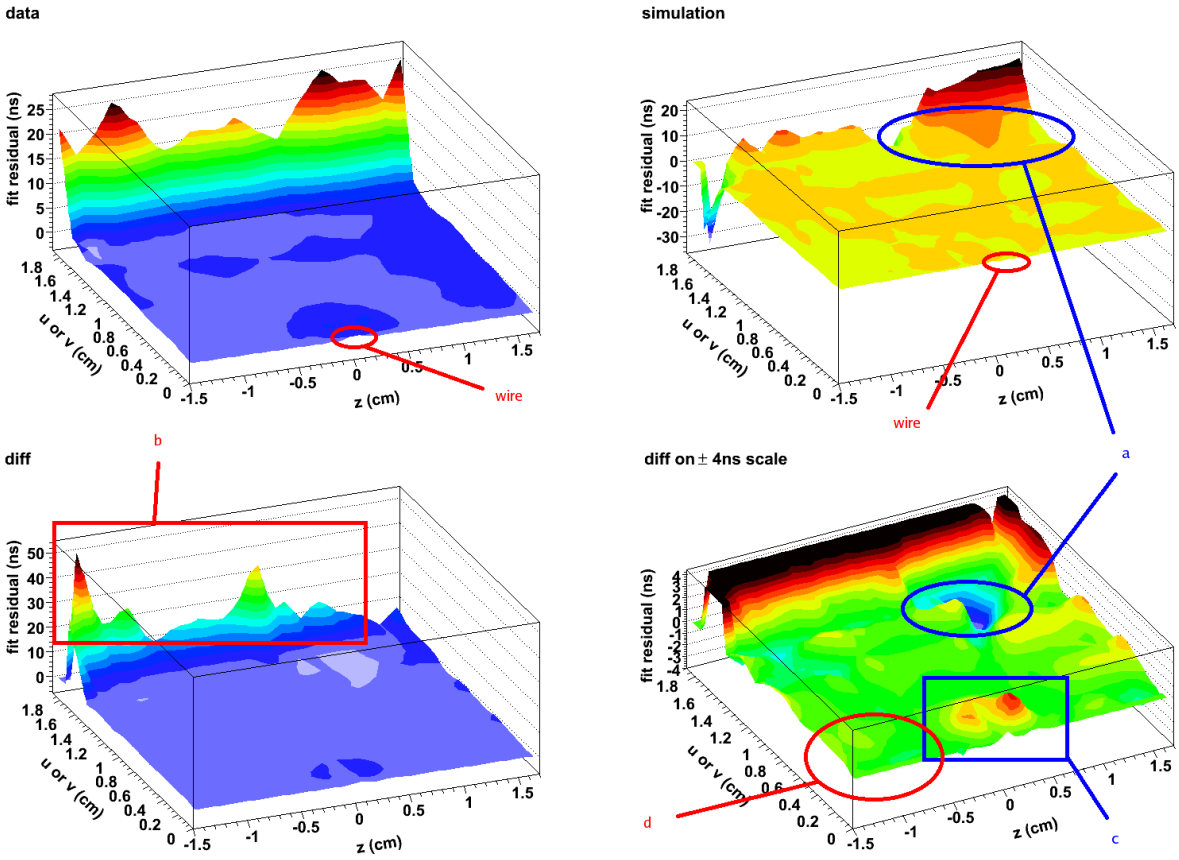

Figure 7.7: The time residuals of data and MC used to derive the STRs averaged over the drift chamber sub-cell and their difference. Marked in the figure are a number of persistent features; a) a "ridge" in the simulation b) a poor statistics region that receives a poor weight in the determination of the STRs c) bumps next to the wire that appear in data because the wire is not exactly at (0,0) d) a "dimple region where there are no hits.

The sensitivity of the muon decay parameters to the STRs was determined by using this difference to distort the STRs used to analyze the Monte Carlo simulation.

The differences between the data and Monte Carlo simulation time residuals are shown in Fig. 7.7. The time residual difference was approximated using a fifth order polynomial. The coefficients of the fit were multiplied by a factor of 10 and the resulting function was added to standard MC calibrated STR to simulate an exaggerated difference between data and simulation. The sensitivities to this change in the analysis is shown in Table 7.12.

This systematic is no longer a leading systematic for ρ with the adoption of the data and Monte Carlo calibrated STRs. The uncertainty for ρ due to the choice of STRs is now 3×10^{-5}, which is nearly an order of magnitude improvement over the previous ρ analysis.

Raw Sensitivities ($\times 10^{-4}$)	
$\Delta\rho$	-3.1 ± 3.4
$\Delta\delta$	-10.3 ± 5.9
$\Delta\xi$	8.8 ± 7.3
Scale Factor	10.00
$\sqrt{\chi^2/ndf}$	0.50
Scaled Fit Result ($\times 10^{-4}$)	
$\Delta\rho$	-0.31 ± 0.17
$\Delta\delta$	-1.03 ± 0.29
$\Delta\xi$	0.88 ± 0.36

Table 7.12: Sensitivities and systematic uncertainties of the muon decay parameters to differences between the calibrated STRs used in data and simulation.

7.5.3 Chamber Foil Positions

The cathode foils of the TWIST DCs have an uncertainty in their positioning due to the Sitall thicknesses used in the construction of the planes and the tension of the foils. The total uncertainty of the foil positions can be as big as 100 μm[44]. This is much larger than the potential uncertainty of the wire positions along the z-axis, which is only a function of the variations in the Sitall thicknesses. The relative position between the wire and the cathode foil can alter the number of tracks that cross a drift cell at large angles, changing the measured track angle.

The sensitivity of this effect was measured by first preparing a special simulation

with the drift chamber foils displaced inward from their nominal positions by 500 μm. This exaggerates the expected uncertainty by a factor to 5. This systematic test was carried out by Anthony Hillairet [44]. The special simulation was compared to a simulation using the nominal geometry files but is otherwise identical. The difference in the muon decay parameters are shown in Table 7.13. After scaling the results by the exaggeration factor this gives us an uncertainty of 0.8 $\times 10^{-4}$ in ρ. Improvement in this systematic may have been made in this experiment with better control of the foil tensions and relative pressures across foils.

Raw Sensitivities ($\times 10^{-4}$)	
$\Delta\rho$	4.0 ± 2.5
$\Delta\delta$	5.9 ± 4.4
$\Delta\xi$	-0.67 ± 5.4
Scale Factor	5
$\sqrt{\chi^2/ndf}$	1
Scaled Fit Result ($\times 10^{-4}$)	
$\Delta\rho$	0.80 ± 0.50
$\Delta\delta$	1.18 ± 0.88
$\Delta\xi$	-1.34 ± 1.08

Table 7.13: Changes in the muon decay parameters measured by changing the foil positions in the simulated TWIST detector.

7.5.4 Time Zero Variations

Uncertainties in the time zeros can arise from two sources. The time zeros are determined based on the time of flight of positrons with respect to two different scintillators. The DS scintillator is used to determine the time of flight for downstream positrons, while the PU scintillator is used to define this information for upstream positrons. The uncertainty on the relative timing of the scintillators was identified as the leading contribution of the time zero uncertainties. The time of flight information measured from the passage of beam positrons through the detector system was used to determine the relative timing and its uncertainty.

The position of the downstream scintillator is known to a precision of ±2.5 mm. Since the full length of the positron tracks through the tracking region is 50 cm so the potential uncertainty of the position of the DS scintillator relative to the position of the PU scintillator is less than 1 %. To be conservative the potential uncertainty

of the timing of upstream tracks relative to downstream tracks is taken as 100 ps. To exaggerate the effect and determine its sensitivity, an analysis of nominal simulation was conducted with the downstream time zeros shifted by 10 ns. The sensitivities measured from this exaggerated simulation could then be scaled by a factor of 100 to get the final uncertainties as shown in Table 7.14. A factor of this magnitude was necessary to produce a measurable change for this systematic effect. Even so, the uncertainty for the ρ parameter is less than 10^{-5} because this time zero asymmetry does not effect the momentum scale of the measured positrons.

7.5.5 Upstream Downstream Efficiency

To set an uncertainty in the decay parameters due to the reconstruction efficiency the results of Table 5.5 were used to alter the relative number of counts upstream and downstream ends of the detector stack. The sensitivities of the decay parameters was determined by altering the contents of a Monte Carlo spectrum by scaling the spectrum by a factor which exaggerates the differences in the reconstruction inefficiencies of data and simulation. The efficiencies used were 10 times the values shown in Table 5.5 using the same linear behaviour with respect to $\cos\theta$. The sensitivities of the decay parameters to the upstream downstream efficiencies and the associated systematic uncertainties are shown in Table 7.15. The efficiency affects the asymmetry parameters $P_\mu\xi$ and δ more than the Michel parameter ρ because the inefficiency is effectively constant with respect to momentum. The (small) change in the relative normalization between upstream and downstream tracks alters the value of rho with a systematic uncertainty of 2 $\times 10^{-5}$.

Raw Sensitivities ($\times 10^{-4}$)	
$\Delta\rho$	9.0 ± 3.2
$\Delta\delta$	-44.3 ± 5.4
$\Delta\xi$	81.8 ± 6.8
Scale Factor	100
$\sqrt{\chi^2/ndf}$	0.07
Scaled Fit Result ($\times 10^{-4}$)	
$\Delta\rho$	0.09 ± 0.22
$\Delta\delta$	-0.44 ± 0.39
$\Delta\xi$	0.82± 0.48

Table 7.14: Systematic uncertainties from the asymmetries of the time zeros.

Raw Sensitivities ($\times 10^{-4}$)	
$\Delta\rho$	2.0 $\pm$ 1.6
$\Delta\delta$	7.5 $\pm$ 2.8
$\Delta\xi$	13.5 $\pm$ 3.5
Scale Factor	10.00
$\sqrt{\chi^2/ndf}$	0.15
Scaled Fit Result ($\times 10^{-4}$)	
$\Delta\rho$	-0.20 $\pm$ 0.02
$\Delta\delta$	-0.75 $\pm$ 0.04
$\Delta\xi$	1.35$\pm$ 0.05

Table 7.15: The uncertainties in the decay parameters related to the measured positron track reconstruction efficiency.

7.6 External Uncertainties

7.6.1 Radiative Corrections

A finite set of radiative correction were included in the simulations, as described in Section 5.1.1, so some level of theoretical uncertainty in the spectrum is expected. Corrections of $\mathcal{O}(\alpha^2)$ and higher were not included because the final calculations were

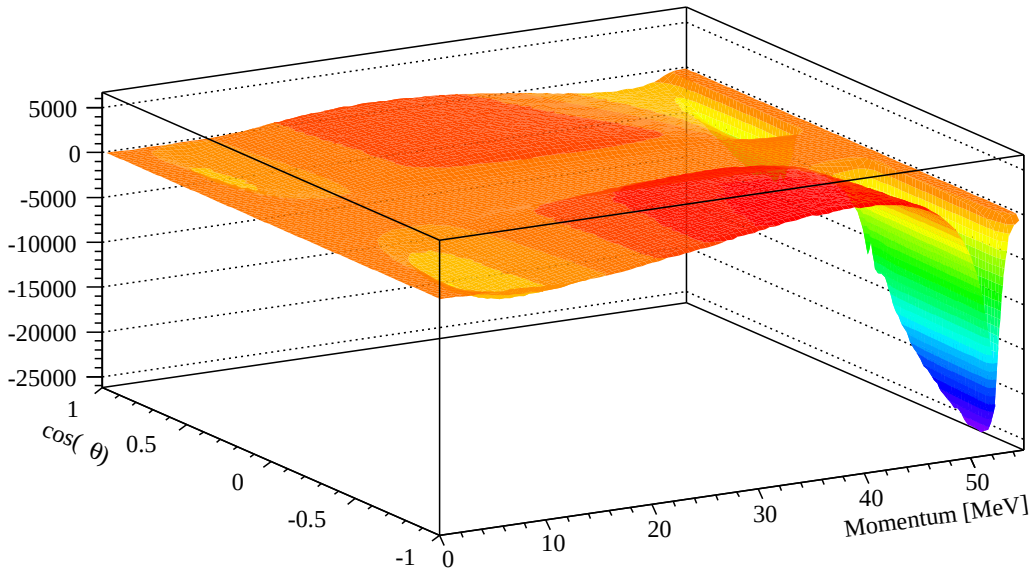

Figure 7.8: Spectrum generated from the $\mathcal{O}(\alpha^2 L)$ correction alone.

not complete when the final black box generation was prepared. The lack of higher order corrections is a systematic uncertainty that must be evaluated in terms of the muon decay parameters.

To evaluate the sensitivity to the lack of the $\mathcal{O}(\alpha^2)$ correction a known spectrum with a shape that approximates the expected behaviour of this higher order correction was introduced in the simulated spectrum to determine the effect on the decay parameters. The $\mathcal{O}(\alpha^2 L)$ correction was used because the shape of the spectrum approximates the expected shape of the $\mathcal{O}(\alpha^2)$ correction. A spectrum containing only the $\mathcal{O}(\alpha^2 L)$ correction was generated using `GEANT` and analyzed in the standard way. The spectrum generated by the simulation of the $\mathcal{O}(\alpha^2 L)$ spectrum is shown in Fig.7.8. This spectrum was added to a nominal simulation (gen584), weighted by a factor of 200 to roughly match the N_{thrown} in the $\mathcal{O}(\alpha^2 L)$ spectrum to the N_{thrown} of the nominal decay spectrum. The combination of the two spectra can then be fit to the nominal MC set to determine the change in the decay parameters.

A scale factor was established by considering the relative amplitude of the radiative corrections under consideration. The $\mathcal{O}(\alpha^2 L)$ term has 5 times more counts at the endpoint relative to the number of counts expected in the $\mathcal{O}(\alpha^2)$ radiative correction. This is further corrected by taking the true ratio between the N_{thrown} of the radiative correction spectrum and the nominal muon decay spectrum multiplied by the scale factor;

$$S = \frac{N_{thrown}^{\mathcal{O}(\alpha^2 L)}}{200 N_{thrown}} \times 5. \tag{7.3}$$

With $N_{thrown} = 994611882$ and $N_{thrown}^{\mathcal{O}(\alpha^2 L} = 221476682610$, $S = 5.57$. The raw sensitivities and the scaled and renormalized systematic uncertainties appear in Table 7.16. This analysis was completed without the application of momentum calibration to the altered spectrum because the edge fits show that the shape of the endpoint spectrum is effectively identical after the addition of the $\mathcal{O}(\alpha^2 L)$ spectrum. The systematic uncertainty of ρ to the radiative correction is $(-0.81 \pm 0.01) \times 10^{-4}$. This systematic can be reduced through the completion of the $\mathcal{O}(\alpha^2)$ radiative correction and the calculation of higher order corrections.

7.6.2 Uncertainties in η Parameter

The decay parameter η cannot be optimally measured from the momentum spectrum of the muon decay due to its suppression by m_e/m_μ. Attempting to measure η directly

Raw Sensitivities ($\times 10^{-4}$)	
$\Delta\rho$	-4.5 ± 3.1
$\Delta\delta$	-3.5 ± 5.5
$\Delta\xi$	2.9 ± 6.7
Scale Factor	5.57
$\sqrt{\chi^2/ndf}$	0.01
Scaled Fit Result ($\times 10^{-4}$)	
$\Delta\rho$	-0.81 ± 0.01
$\Delta\delta$	-0.63 ± 0.01
$\Delta\xi$	0.52 ± 0.01

Table 7.16: The uncertainties in the decay parameters resulting from uncertainties in the radiative corrections used in the generation of the simulation.

in a simultaneous fit results in large uncertainties for ρ because of the correlations between the parameters. At this time the uncertainty in the η parameter represents a leading systematic on ρ that cannot be removed by any further improvements in this experiment. Improvements in the measured value of ρ are then partially dependent on improvements in the measurement of η. These increases in the precision of η are best accomplished by using a separate measurement of the polarization of the decay positrons.

The uncertainty in ρ resulting from potential changes in the η parameter was measured by adding a fixed contribution of the η spectrum to a standard fit between data and MC. The best modern results for η = -0.0036 ± 0.0069 is derived from recent global fits [18] [1]. To determine the effect of η on the other decay parameters, fits between a nominal muon decay spectrum (set84) and its simulation were composed which fix the contribution of the η parameter to values ±0.0036 about what exists in the black box spectrum. The uncertainties in all three decay parameters due to η are shown in Table 7.17.

7.7 Discarded Systematics

During the analysis a number of systematics were considered that were smaller than the 5×10^{-5} threshold assumed for significant systematics. These systematics are

- Hard scattering: the change in the muon decay parameters due to large changes in the reconstructed angle θ.

Raw Sensitivities ($\times 10^{-4}$)	
$\Delta\rho$	1.1 ± 3.1
$\Delta\delta$	0.013 ± 5.4
$\Delta\xi$	1.1 ± 6.6
Imposed $\Delta\eta$	0.0072
σ_η from [18]	0.0069
$\sqrt{\chi^2/ndf}$	0.0142
Scaled Fit Result ($\times 10^{-4}$)	
$\Delta\rho$	1.05 ± 0.04
$\Delta\delta$	0.12 ± 0.07
$\Delta\xi$	1.05 ± 0.09

Table 7.17: Systematic sensitivities and scaled uncertainties determined for the sensitivity to changes in the η parameter.

- Dead zone: the effect on the decay spectrum due to the potential bias introduced in the reconstruction by the passage of muons through the drift chambers.
- Translations: Uncertainty of decay parameters due to changes in the translational alignment of the drift chamber planes.
- Rotations: Uncertainty of decay parameters due to changes in the rotational alignment of the drift chamber planes.
- STR (density variations): Effect on the reconstructed decay spectrum due to changing the density in the STRs.
- t0 - shape distortions: Changes in the decay parameters that result from using time zeros multiplied by a uniform factor of 10.
- Positron Beam Intensity: Change in the decay spectrum determined from increasing the positron beam rate by a factor of 10.
- Translated B field: Change in the decay spectrum measured from translating the magnetic field map by 2 cm in the u-direction and 2 cm in the v-direction.

These systematics were discarded from the main systematics are shown in Table 7.18.

$\times 10^{-4}$	ρ	δ	ξ
Hard scattering	0.02	0.01	0
Dead zone	0.05	0.13	-0.23
Translations	-0.03	-0.01	0.01
Rotations	0.01	0.01	-0.02
STRs (density variations)	0.07	-0.12	0.15
t0 - shape distortions	0.06	0.11	-0.04
Positron Beam Intensity	0.12	0.34	-0.16
Translated B Field	0.03	0.05	-0.11

Table 7.18: The discarded systematic uncertainties for the measurement of all three muon decay parameters.

Chapter 8

Results of Michel Parameter Measurement

8.1 Blind Analysis Results for ρ

The black box values of the muon decay parameters were revealed to the experimental group on January 29, 2010. Prior to box opening it was agreed that the results would be published regardless of the central values. When these initial values are added to the measured $\Delta\rho$ the average value of ρ is 0.749913 $\pm$ 0.00009(stat) $\pm$ 0.00028(sys). The values of $\Delta\rho$ measured from all of the data sets are shown in Table 8.2. The decay parameters after opening the black box are summarized in Table 8.1. All of the parameters are consistent with the standard model results at the 2 σ (99.5% confidence) level. The results are in excellent agreement with the previous results from the TWIST experiment.

The measured values of the decay parameters are shown in Fig. 8.1 for all of the data sets used in this analysis. Not all of the data sets used for the measurement of

	Hidden Value	Average Difference	Final Values
ρ	0.7404	$(95.1 \pm 2.9) \times 10^{-4}$	$0.74991 \pm 0.000089 \pm 0.00028$
δ	0.745592	$(51.3 \pm 3.3) \times 10^{-4}$	$0.75072 \pm 0.00016 \pm 0.00029$
ξ	0.992808	$(80.26^{+16.9}_{-7.2}) \times 10^{-4}$	$1.00089 \pm 0.00035^{+0.00165}_{-0.00063}$

Table 8.1: The final results of the TWIST experiment. Black box values of the decay parameters are added to the average measured difference in the parameters between data and simulation to produce the final results.

	Shifted ECal.				Scaled ECal.					
Set	$\Delta\rho \times 10^4$			Corr.	$\Delta\rho \times 10^4$			Corr.	EC Err.	Total $\Delta\rho \times 10^4$		
68	98.47	±	3.53	-1.2	96.43	±	3.53	-1.29	0.28	96.21	±	3.54
70	99.84	±	2.91	-1.07	97.87	±	2.91	-1.15	0.23	97.75	±	2.92
71	96.14	±	3.06	-1.11	94.37	±	3.06	-1.19	0.25	94.11	±	3.07
72	96.08	±	2.99	-0.99	94.3	±	2.99	-1.06	0.23	94.17	±	3
74	100.76	±	3.48	-1.27	98.71	±	3.48	-1.36	0.28	98.42	±	3.49
75	95.04	±	2.97	-1.04	93.49	±	2.97	-1.11	0.24	93.19	±	2.98
76	101.33	±	3.24	-1.16	99.19	±	3.24	-1.24	0.25	99.06	±	3.25
83	97.25	±	3.04	-0.93	95.11	±	3.04	-1	0.24	95.22	±	3.05
84	98.31	±	3.18	-1.01	96.06	±	3.18	-1.08	0.25	96.14	±	3.19
86	94.96	±	2.88	-0.73	93.1	±	2.89	-0.79	0.22	93.27	±	2.89
87	98.8	±	3.13	-0.98	96.78	±	3.13	-1.05	0.25	96.78	±	3.14
91	80.13	±	5.98	-1.19	78.2	±	5.98	-1.27	0.58	77.94	±	6.01
92	94.72	±	5.15	-1.25	92.39	±	5.15	-1.34	0.46	92.26	±	5.17
93	100.24	±	4.2	-0.92	98.31	±	4.2	-0.99	0.35	98.32	±	4.21
									Correction For mcfitter Bias	-0.20		
									Weighted Average	95.13	±	0.89

Table 8.2: The collected muon decay fit results for all data sets with their corrections and uncertainties. The "Total $\Delta\rho$" are the averaged values between measurements using the shifted and scaled ECal after including the unequal statistics correction, which were described in Section 6.3. The total uncertainties are the quadratic sum of the statistical uncertainties with the uncertainties from the ECal measurement described in Section 6.2.3. The averaged mcfitter bias was subtracted after completing the weighted average over all data sets.

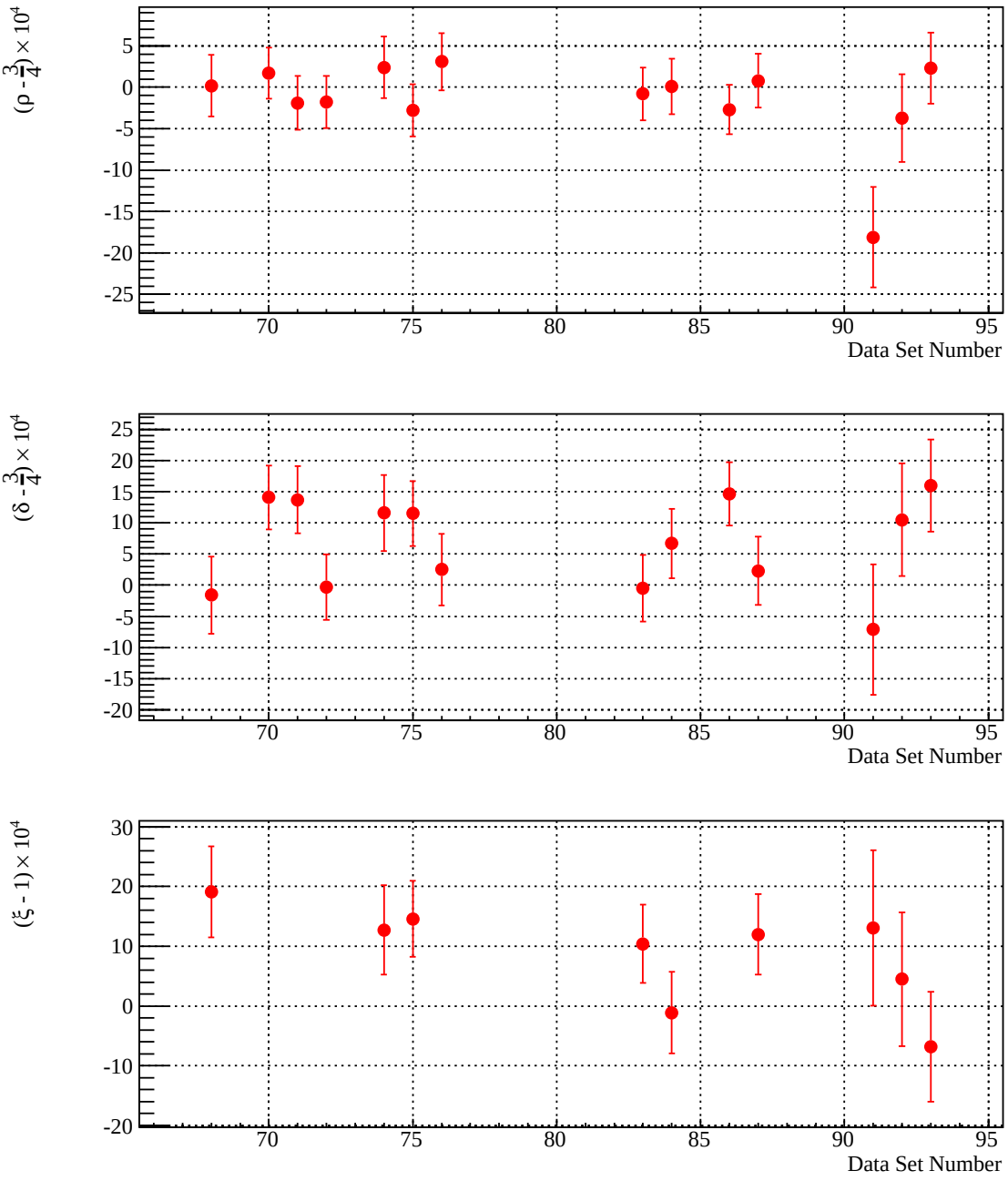

Figure 8.1: The measured decay parameters for all data sets, including those that were excluded in the $P_\mu\xi$ average. All corrections and statistical uncertainties are included in the data points.

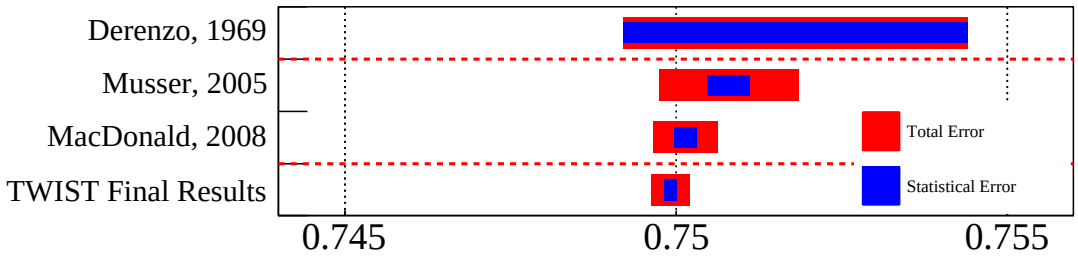

Figure 8.2: Improvements in the uncertainty of the ρ parameter of the current measurement compared to previous measurements.

ρ and δ were used for the measurement of $P_\mu\xi$ because a the polarization systematics for a few of the data sets are poorly understood. The systematics particular to δ and $P_\mu\xi$ are treated elsewhere and these choices will not be justified here.

The average for ρ is shown in the context of recent historical results in Fig. 8.2. The last, best, measurement of ρ was described in a review by Derenzo in 1969[12]. Other measurements of ρ from positive muon decay were not completed until the previous rounds of the TWIST experiment. The results of this latest measurement are completely consistent with the previous measurements of the ρ parameter as well as the Standard Model value of 0.75.

No particular anomalies appear in the fits of the decay spectra. Examples of the fit residuals for silver data appear in Fig. 8.3 and for aluminum data in Fig. 8.4. These figures show the residuals for each histogram bin normalized by the error on that bin. The projections do not show any strong trends within the fiducial region. The residuals are very nearly distributed as a Gaussian as shown by the consideration of the integrated residuals.

Significant improvement in the uncertainties of the muon decay parameters have been achieved by this experiment. The total uncertainty in ρ is a factor of 8.78 smaller than the best measurement previous to TWIST [12]. The other decay parameters, δ and $P_\mu\xi$, have seen similarly significant improvements in their uncertainties.

A particularly important result is the value of the parameter combination, $P_\mu\xi\delta/\rho$, which is required to be less than zero by the positivity constraints of the muon decay spectrum. This measurement indicates that $P_\mu\xi\delta/\rho = 1.00192^{+0.00167}_{-0.00066}$; a deviation of 2.9 σ from the physical region. The 90% confidence lower limit on the possible values assumed by this combination is $P_\mu\xi\delta/\rho > 0.999564$ based on this measured central value. This limit has serious repercussions in the discussion of models applicable to the experiment such as left-right symmetric models.

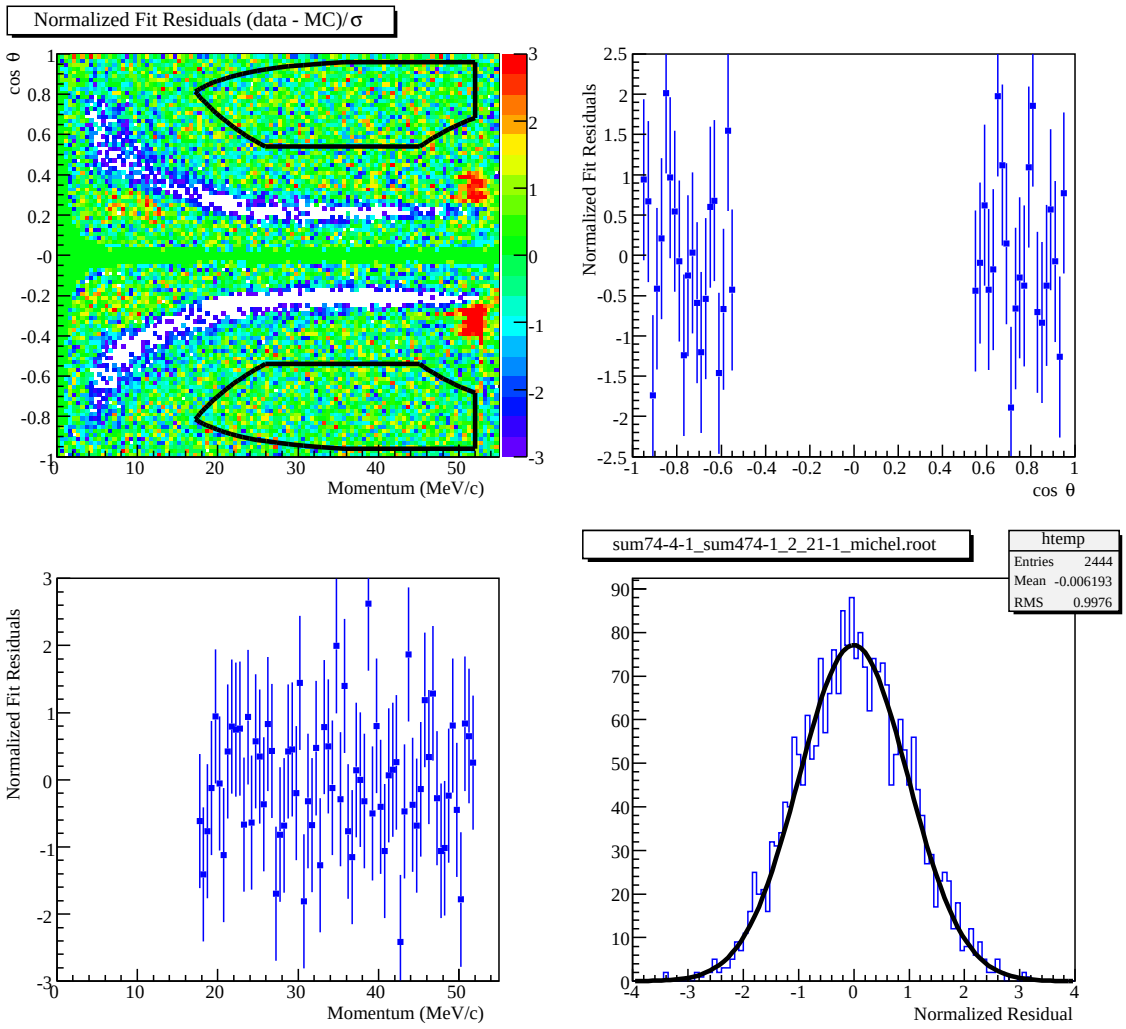

Figure 8.3: The normalized residuals of the data to simulation fit for the nominal silver data set (74). The top right and bottom left plots show the projections onto the cos θ and momentum axes, respectively. Only events contained in the fiducial region, inscribed by the black lines in the 2-d plot on the top left, were used for the projections. The bottom right plot shows the accumulated normalized residuals through the fiducial region with a Gaussian fit superimposed.

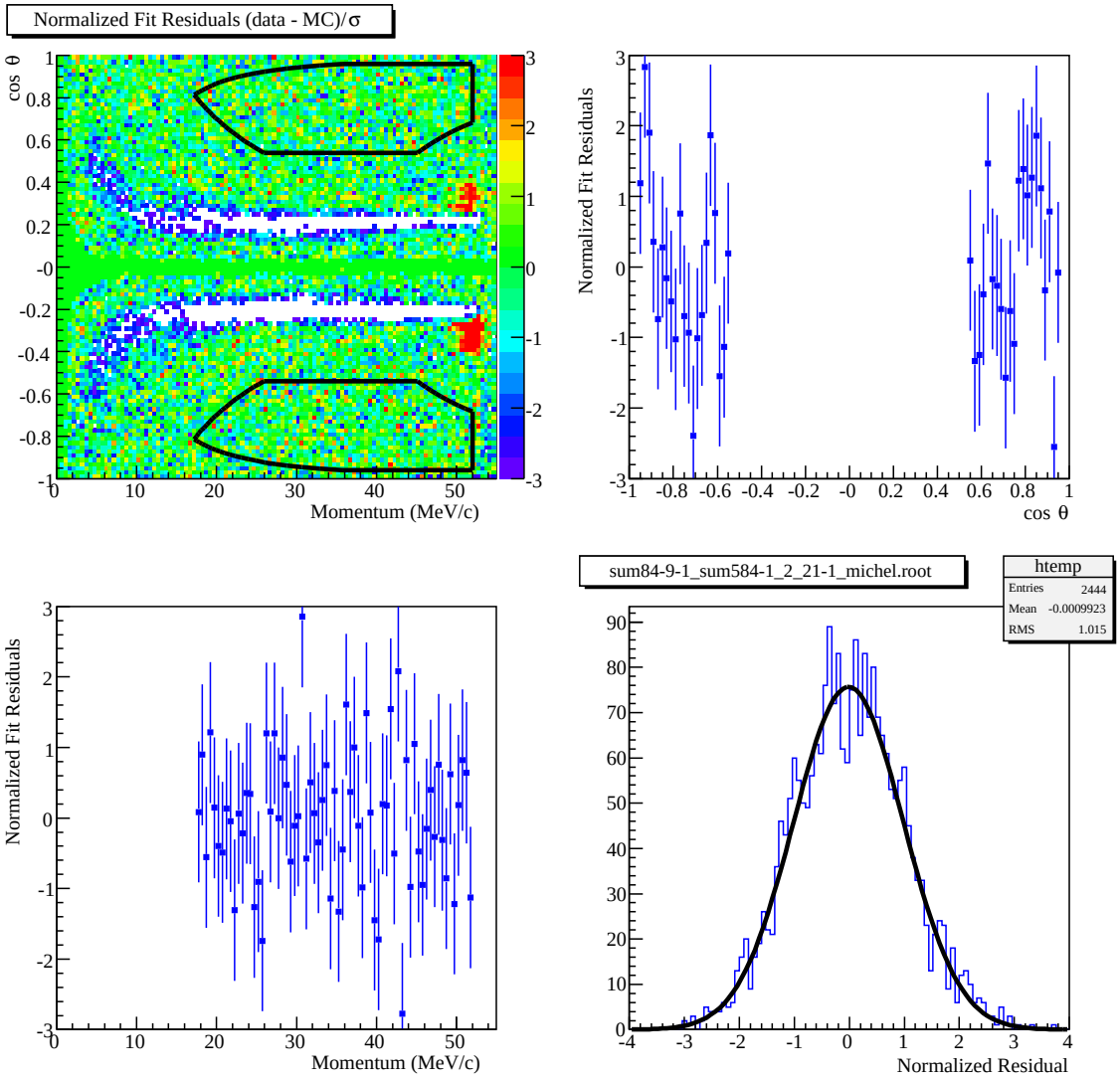

Figure 8.4: The normalized residuals of the data to simulation fit for the nominal aluminum data set (84). The top right and bottom left plots show the projections onto the $\cos\theta$ and momentum axes, respectively. Only events contained in the fiducial region, inscribed by the black lines in the 2-d plot on the top left, were used for the projections. The bottom right plot shows the accumulated normalized residuals through the fiducial region with a Gaussian fit superimposed.

8.1.1 White Box Validation

To ensure that the black box results are credible, a test of the measurement procedure is carried out after hidden parameters were revealed to the experiment. This test, called the white box procedure, is a test of the internal consistency of the analysis

	ρ	δ	ξ
Measured Values	0.74991	0.75072	1.00083
White Box Values	0.74991	0.750665	0.998996
Difference	0.00000	-0.00005	0.00183
Corrections	0.00010	0.00004	0.00060
Expected Results ($\times 10^{-4}$)	-1.0	-0.9	12.3
Test 1: Silver Stopping Target			
Measured Difference ($\times 10^{-4}$)	2.9 ± 3.5	2.9 ± 6.0	20.2 ± 7.4
Test 2: Aluminum Stopping Target			
Measured Difference ($\times 10^{-4}$)	1.0 ± 3.2	2.7 ± 5.6	5.1 ± 6.8
Test 3: Silver Stopping Target, Random Input			
Measured Values	0.74991	0.75072	1.00083
White Box Values	0.753227	0.746542	0.996412
Difference	-0.00331	0.00418	0.00442
Corrections	0.00010	0.00004	0.00060
Expected Results ($\times 10^{-4}$)	-34.1	41.4	38.2
Measured Difference ($\times 10^{-4}$)	-29.1 ± 3.5	45.4 ± 6.1	41.8 ± 7.5

Table 8.3: Results from the white box validation procedures. Tests 1 and 2 used the same input parameters for the test for the silver stopping target and the aluminum target, respectively. Test 3 used a set of randomly selected parameters for the white box. The results of these tests are universally consistent with the expected values. There is a 28% χ^2 probablility that this set of values will result from an unbiased fitting procedure.

procedures independent of the muon decay parameters used in the simulation. To implement the validation, a new decay sample generator is produced, with the decay parameter values fixed to their measured values. The results of analyzing these decay samples should be consistent with zero for the test to be a success. This test has been conducted on the previous rounds of the TWIST analysis, and was applied again for the final analysis round to make sure that the changes to the analysis did not break the internal consistency of the analysis. Such a test can only be done after the box is opened because it requires a violation of the blind condition of the analysis.

Because of the requirement on $P_\mu \xi \delta / \rho$, the actual decay parameters could not be used for this test. Instead, the value of $P_\mu \xi$ was defined to be $\rho/\delta = 0.998996$. Consequently the criterion for success changes a little, as the expected difference $P_\mu \xi_{data} - P_\mu \xi_{MC} = 18.3 \times 10^{-4}$.

Two different white box simulations were completed using the measured values of ρ and δ with the maximum allowed value of $P_\mu \xi$. By accident a third white box was

Parameter	Value	Reference
Current TWIST decay parameters		
ρ	0.74991 ± 0.00028	
δ	0.75072 ± 0.00033	
ξ	$1.00084^{+16.9}_{-11.9}$	
Previous decay parameters		
ρ	0.7518 ± 0.0026	[4]
δ	0.7486 ± 0.0038	[45]
$P_\mu\xi$	1.0027 ± 0.0085	[46]
$P_\mu\xi\delta/\rho$	0.99787 ± 0.00082	[23]
Parameters from positron Polarization		
ξ'	1.00 ± 0.04	[4]
ξ''	0.65 ± 0.36	[47]
$\bar{\eta}$	0.02 ± 0.08	[4]
α/A	0.015 ± 0.052	[47]
β/A	0.002 ± 0.018	[47]
η	0.071 ± 0.037	[48]
η''	0.105 ± 0.052	[48]
α'/A	-0.047 ± 0.052	[47]
	-0.0034 ± 0.0219	[48]
β'/B	0.017 ± 0.018	[47]
	-0.0005 ± 0.00080	[48]

Table 8.4: Important results for muon decay analyzes used as input for the global analysis. The two sided limit for ξ required an assumption about its distribution of potential values.

generated using a set of randomly generated decay parameters. These simulations were fit against the data and the results were compared to the expected differences; that is the difference in the decay parameters between the data and the white box simulation, plus the corrections in the analysis for momentum calibration and depolarization effects. All three tests show strong consistency between the values of the decay parameters measured from the simulation and the expected values, with differences that are less than one standard deviation. The χ^2 probability of this degree of consistency occurring is 28%. The white box results are summarized in Table 8.3. This establishes the self consistency of the TWIST results.

	2004	2008	2010
$\lvert g^S_{RR}\rvert$	0.166	0.062	0.031
$\lvert g^V_{RR}\rvert$	0.033	0.031	0.015
$\lvert g^S_{LR}\rvert$	0.125	0.074	0.041
$\lvert g^V_{LR}\rvert$	0.060	0.025	0.018
$\lvert g^T_{LR}\rvert$	0.036	0.021	0.012
$\lvert g^S_{RL}\rvert$	0.424	0.412	0.412
$\lvert g^V_{RL}\rvert$	0.110	0.104	0.103
$\lvert g^T_{RL}\rvert$	0.122	0.104	0.103
$\lvert g^S_{LL}\rvert$	0.550	0.550	0.550

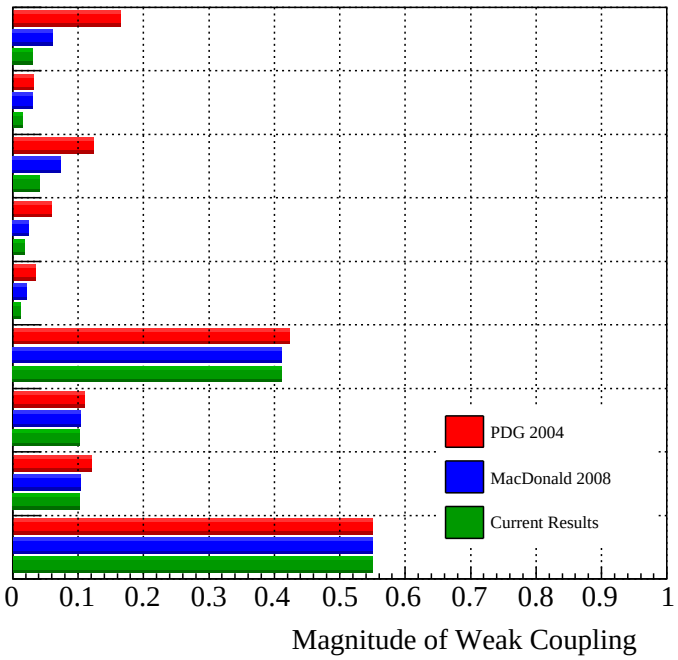

Figure 8.5: 90% confidence limits on the coupling constants from before the TWIST experiment, resulting from the TWIST intermediate analysis, and resulting from the TWIST final analysis.

8.2 Global Fit Results

To make a more complete determination of the properties of the muon decay, a global fit must be done using results from all available experiments. The important results used are summarized in Table 8.4. These results include the decay parameter results described here and the measurements of various parameters derived from the longitudinal and transverse polarization of the decay positron[4][47][48].The global fit, written by Gagliardi *et. al.* [18], uses a Monte Carlo integration to calculate new central values for all of the parameters associated with the weak interaction and the weak coupling constants of Equation 2.1, allowing for the physical constraints on the interaction. The output of this procedure is shown in Table 8.5. The most likely set of muon decay parameters that satisfy the constraints of the system is also included. The improvements in the output are compared visually to previous results in Fig.8.5.

A product of this procedure is new indirect determination of $\eta = -0.0033 \pm 0.0045$ which improves upon the old limit by a factor of nearly 3/4. A consensus was reached that the value of η determined from the global fit would be used for the final value

Parameter	Result from [1] ($\times 10^{-3}$)	Current Results ($\times 10^{-3}$)
Q_{RR}	< 0.96	< 0.24
Q_{LR}	< 1.38	< 0.42
Q_{RL}	< 42	< 42
Q_{LL}	> 955	> 955
B_{LR}	< 0.64	< 0.34
B_{RL}	< 10.8	< 10.8
ρ	0.74964 ± 0.00035	0.74964 ± 0.00014
δ	0.74997 ± 0.00065	0.75035 ± 0.00022
ξ	-	0.99862 ± 0.00040
η	-0.0042 ± 0.0064	-0.0033 ± 0.0046

Table 8.5: Parameters output by the global analysis described by the text. 90% confidence level upper limits are given for the interaction probabilities, $Q_{\epsilon\mu}$ and $B_{\epsilon\mu}$. Intermediate TWIST global fit results are given from Ref. [1] to show where the current TWIST results improve the limits on the interaction probabilities.

of ρ. This new eta makes no changes in the final central values ρ, δ, and $P_\mu\xi$, although it does change the associated systematic uncertainty. Such a correction is considered to be reasonable because the majority of the weight in the global fit result for η is thought to come from measurements of the positron transverse momentum. This decision carries over into the final systematic uncertainty as well. The final uncertainty for ρ then decreases by approximately 1 part in 10^{-5} so that the final reported value is $\rho = 0.74996 \pm 0.000089 \pm 0.00027$.

8.3 Left Right Symmetric Models

The final results of the TWIST experiment are not physical within the framework of the left-right symmetric models. In this class of models δ is required to be 3/4, while $P_\mu\xi\delta/\rho$ is bound by $\pm$ 1, which implicitly bounds $\rho \leq 3/4$. However, limits on the parameters of the model can be set based on the measurements.

The value of ρ sets a limit on the mixing angle of the potential W_1 and W_2 bosons (see Eq.2.27), while the values of $P_\mu\xi$ and $\xi\delta/\rho$ restrict the mass of the W_2 boson in addition to the mixing angle (see Eq.2.23 and Eq.2.25). The limits for the Manifest and Pseudo-Manifest models are shown in Fig.8.6. In the left-right symmetric model the new value for ρ sets a 90% confidence limit on the value of the mixing angle $\zeta_g < 0.0193$ [49].

In the Manifest left right model, the limits set on the W_2 mass cannot compete with the direct limits set by experiments such as D0 and CDF. However when the conditions on the relative strengths of the couplings are relaxed, as is the case in the pseudo-manifest model, the TWIST results do not lose their significance while the direct search is no longer applicable.

8.4 Outlook for Future Measurements of ρ

Further improvements in the statistical precision in ρ will require refinements in the systematic uncertainties. The statistical uncertainty of ρ decreases as $1/\sqrt{N}$, where N is the number of events collected by the experiment. To decrease the statistical precision by an order of magnitude, the number of muon decay events collected will have to increase by a factor of 100. This will require an intense, stable muon source over longer run period to complete such a data set. The collection rate of the TWIST apparatus made the time the limiting factor for such an attempt as the data acquisition has difficulty handling muon trigger rates greater than 5 kHz due to a combination of a hardware limitations and the software's limited ability for handling multiple muons in an event imposed by the muon lifetime. Both of these problems will have to be considered in the design of a new experiment. An increase in statistics will not be productive unless there is an accompanying increase in the control of the accompanying systematics.

The leading systematic for ρ lie in the positron interactions, the momentum calibration, and the external uncertainties. Improvement in the determination of the systematic due to the bremsstrahlung rate will be important. To refine this systematic, the reconstruction of data and simulation must have a better match for radiative components of the momentum loss through the active detector region. The matching Monte Carlo simulation would require a validation at a much higher precision than the few percent that currently exists to make such an improvement feasible. A further possibility is to fit the momentum loss through the detector region. This will require a much more precise detector and track reconstruction than what was used for the TWIST measurement. This would also reduce the systematics associated with the momentum calibration.

Further improvements in the systematics will not be possible if there are not improvements the measurements of η or calculation of the higher orders in the radiative corrections. The correlation between η and ρ means that a better measurement of

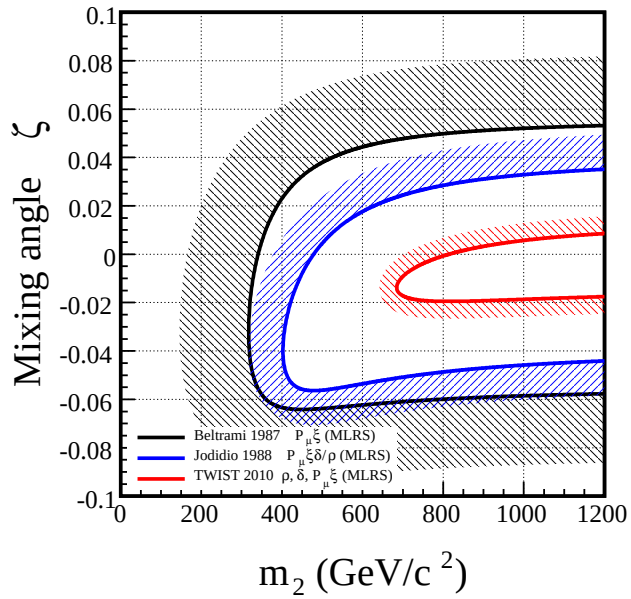

a) Manifest left right symmetric model

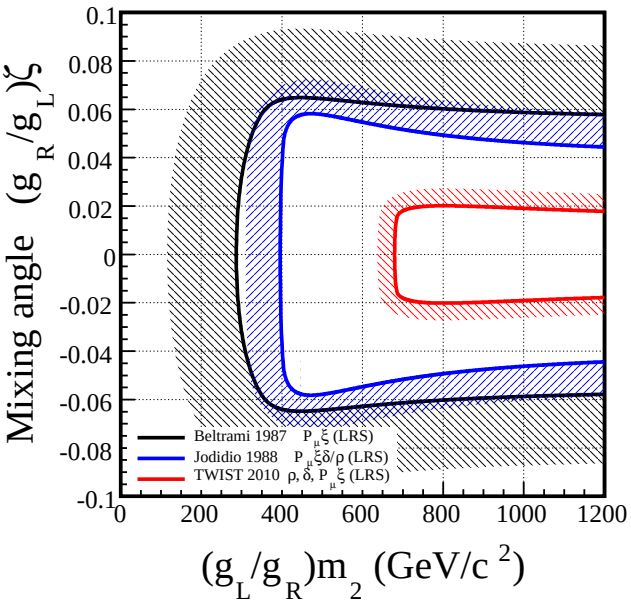

b) Pseudo-manifest left right symmetric model

Figure 8.6: Limits on the $\zeta - m_2$ phase space allowed by existing muon decay measurements for the manifest (a) and psuedo-manifest (b) left right symmetric models as defined in [5] . The allowed region is contained by the solid line.

ρ will not be possible if there is no better direct measurement of η. These measurements can be taken from measurements of the positron polarization. To a lesser extent, calculations of the higher order radiative corrections will also be necessary for measurements of precision greater than a part in 10^4.

Many issues, including the anomalous $P_\mu \xi\delta/\rho$ measurement, may be resolved if the TWIST detector system has better resolution for small angle positron tracks, particularly in the downstream direction. This could be achieved by using a detector with a larger active area in the U-V plane and a lower magnetic field. The lower magnetic field allows for the effective measurement of smaller transverse momenta, while the larger active area is required to avoid losing positron tracks with large transverse momenta. To increase the active area of the detector a larger bore solenoid would be required as that was a limiting factor in the detector construction. For example if the maximum momentum allowed is to be maintained for a magnetic field of 1 Tesla, and the stopping target radius remains the same, then the diameter of the active area of the detector modules must be 62.76 cm, which is larger than the bore of the TWIST solenoid. This would allow a minimum transverse momentum of 5 MeV/c, and likewise lower the minimum longitudinal momentum cut, but more importantly, it would allow for an increase in the upper fiducial limit such that $|\cos\theta| < 0.98$.

Alternatively, a secondary spectrometer system specifically for far forward positrons would help by providing a redundant measurement of the far forward positrons. If there is sufficient overlap in the angle and momentum space sampled by these detectors it might also help to resolve some of the momentum calibration problems observed in the TWIST experiment. Such considerations would be useful for further experiments.

Chapter 9

Search For Rare Decay Modes

By collecting a large sample of muon decays, the TWIST experiment has produced an excellent event sample for searches for decay signals that are not allowed in the standard model. Only a small number of the commonly considered rare decay signals can be competitively measured in the TWIST spectrum. The main candidates are two body decay signals where the muon decays into a positron and a neutral Nambu-Goldstone (NG) or pseudo Nambu-Goldstone (pNG) boson that does not decay further before leaving the detector. This was discussed in detail in Section 2.2. Of particular interest are cases where there are anisotropies in the decay signal as described in Equation 2.28.

Measurements of $\mu^+ \to e^+\gamma$ are not accessible to the experiment because it was not designed to detect photons from the muon decays. Measurements of $\mu^+ \to e^+e^+e^-$ are not practical because the acceptance of the TWIST detector does not cover the 4π solid angle necessary to determine three decay tracks and trace them back to a decay vertex with the necessary consistency. The number of well reconstructed events collected by the TWIST experiment is also much smaller than the sample sizes of the dedicated $\mu^+ \to e^+\gamma$ or $\mu^+ \to e^+e^+e^-$ experiments.

A measurement of two body signals in the TWIST muon decay spectrum was completed by adding a model of the decay into the TWIST `mcfitter` program. The model of the two body decay signal was derived from the momentum response function determined from the TWIST simulation as shown in Fig. 9.1. Multiple cases of the signal anisotropy were considered. The statistical uncertainty of the measured signals depend on how the anisotropy of the decay signal relates to the anisotropy of the background. Systematic uncertainties in the TWIST spectrum make a significant contribution to the total uncertainty, particularly at the endpoint of the decay spec-

trum. For this reason, special consideration is applied to the production of NG bosons. The significance of any decay signals found and their associated confidence intervals must be computed using the combined systematic and statistical uncertainties.

9.1 Modelling Two Body Decays

A two body decay will produce a surplus of positrons that peak at a momentum p_X. The most probable momentum is dictated by the mass of the X^0 boson. For a NG boson, the mass of the X^0 boson is by definition zero and the peak will appear at the endpoint of the spectrum, $p_X = W_{e\mu} = 52.828$ MeV/c. For a pNG boson

$$p_X = \sqrt{\left(\frac{M_\mu^2 - m_X^2 + m_e^2}{2M_\mu}\right)^2 - m_e^2}. \tag{9.1}$$

The two body decay signal is assumed to be dominated by the momentum response. Thus, the model for the two body decay is determined from the simulation by using the difference between the reconstructed positron momentum and the momentum of the positron at its time of decay, as derived from the Monte Carlo vertex banks. This choice to use the Monte Carlo derived momentum response removes

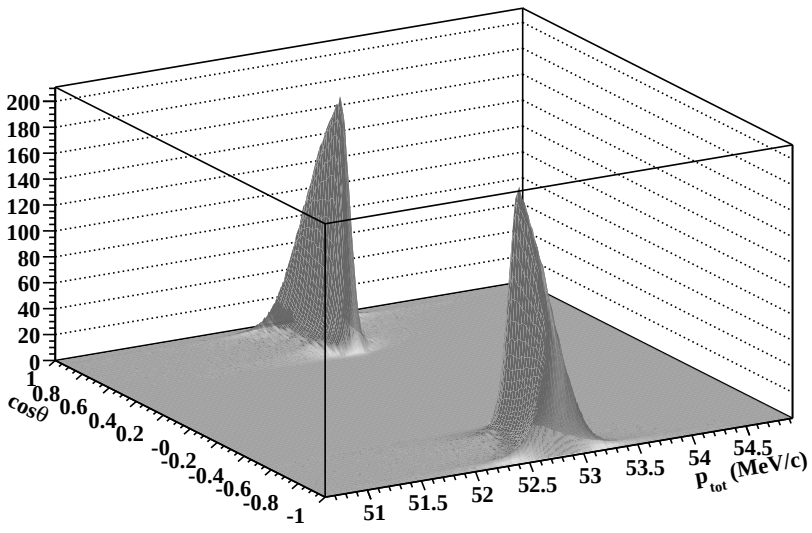

Figure 9.1: Peak added to the muon decay spectrum to model the presence of a two body muon decay at the endpoint.

potential systematics uncertainties that may result both from the assumption of the shape of the model of the $\mu^+ \to e^+ X^0$ decay and the distortions due to the momentum loss. It is valid to assume that the momentum response will dominate the width decay signal if the width of the rare decay peak is less than 100 keV. For this to be true, an unobserved particle must have a lifetime of at least $\hbar/100$ keV $= 6.6 \times 10^{-21}$ s.

The momentum response was computed as a function of $\cos\theta$ in 100 bins of constant width. The magnitude of the raw momentum response will vary as a function of $\cos\theta$ because its statistics were derived from the muon decay distribution. The decay signal model was forced to be isotropic by averaging the content of the upstream and downstream Δp distributions for bins with matching $|\cos\theta|$. Anisotropic peaks were produced by multiplying the content of the bins of the isotropic peak distribution by a factor of $\mathcal{A}_\pm = 1 \pm \cos\theta$.

Since the momentum response also varies slowly as a function of momentum, the response was developed as a set of eight separate histograms, each integrated over a 5 MeV/c range through the fiducial region. A two body decay peak at a momentum p_X that falls within the range $p \in [35, 40]$ MeV/c, for example, is assumed to be well described by the response function integrated over the same range.

9.2 The Background Spectrum

The standard TWIST simulation is used for the background to eliminate potential systematics. Since the data and the Monte Carlo simulation are analyzed in the same way, variations that appear in the decay spectrum due to analysis effects are cancelled out in the spectrum fit. If a smooth, theoretical muon decay spectrum is assumed as the background for this measurement systematic uncertainties will have to be defined for the analysis biases, detector granularities, and inefficiencies that are not necessary when the standard TWIST analysis is used.

Introducing a two body decay to the muon decay spectrum can alter the nature of the background. This is a particular problem at the endpoint of the decay spectrum where the ECal of the spectrum is determined. Since the ECal is known to be related to the decay parameters linearly, this effect may be corrected by allowing the muon decay parameters to vary with the amplitude of the introduced two body signal.

To sample signals that are on the order of 100 keV/c wide, based on the detector momentum response, the simulation spectrum was rebinned with a width of 10 keV/c.

This is in contrast to the 500 keV/c bin width used in the standard muon decay parameter analysis. This choice results in a bias in the measured values of the muon decay parameters. This bias is shown in Fig. 9.2. This is an effect due to the unequal statistics bias described in Section 6.2.3, which is exaggerated by the small bin size. As with the standard Monte Carlo fitting algorithm, an extended likelihood function was not implemented for the difference between two Poisson distributed random numbers, because the suitable statistic was not known. The decay parameters are not consistent with the nominal analysis, but this is not a problem for the purposes of the peak search. Since this bias is statistically driven it can be reduced by adding the data sets together before the fitting algorithm is applied to the data. Since this makes an order of magnitude increase in statistics over a single data set, the effective bias resulting from the small bins is consistent with the 100 keV/c bin width.

9.2.1 Combination of Data Sets

The separation of data into sets is not optimal from the standpoint of a counting experiment. The data sets can be combined trivially if the momentum response is identical from data set to data set after momentum calibration. Set to set differences are generally not sufficient to alter the shape to the momentum response distribution. The momentum response is mostly driven by the momentum loss in the detector which means that it will be mostly constant while the detector material is unchanged. In these cases it is reasonable to add all of the data histograms and all of the Monte Carlo histograms together prior to fitting.

More caution is required when the momentum loss and resolution is different between the various simulated set in the summation as is the case when data from different targets are added together. The ratio of the number of events in Ag data to the number of events in Al data should be preserved in the decay signal model, which was derived from the difference between the reconstructed momentum and the truth bank momentum at the time of decay. The accumulated number of fiducial events in data and simulation is shown in Table 9.1. The ratio of events between the simulation and the data for each target must also be matched to simplify the normalization of the response function. This was achieved by removing the reduced momentum data sets (90, 91, and 92) from the sum of all data sets. With the ratios of the data to the Monte Carlo simulation matched between Ag and Al targets, the ratio between the two targets must be matched in the response function. The simulated Al response

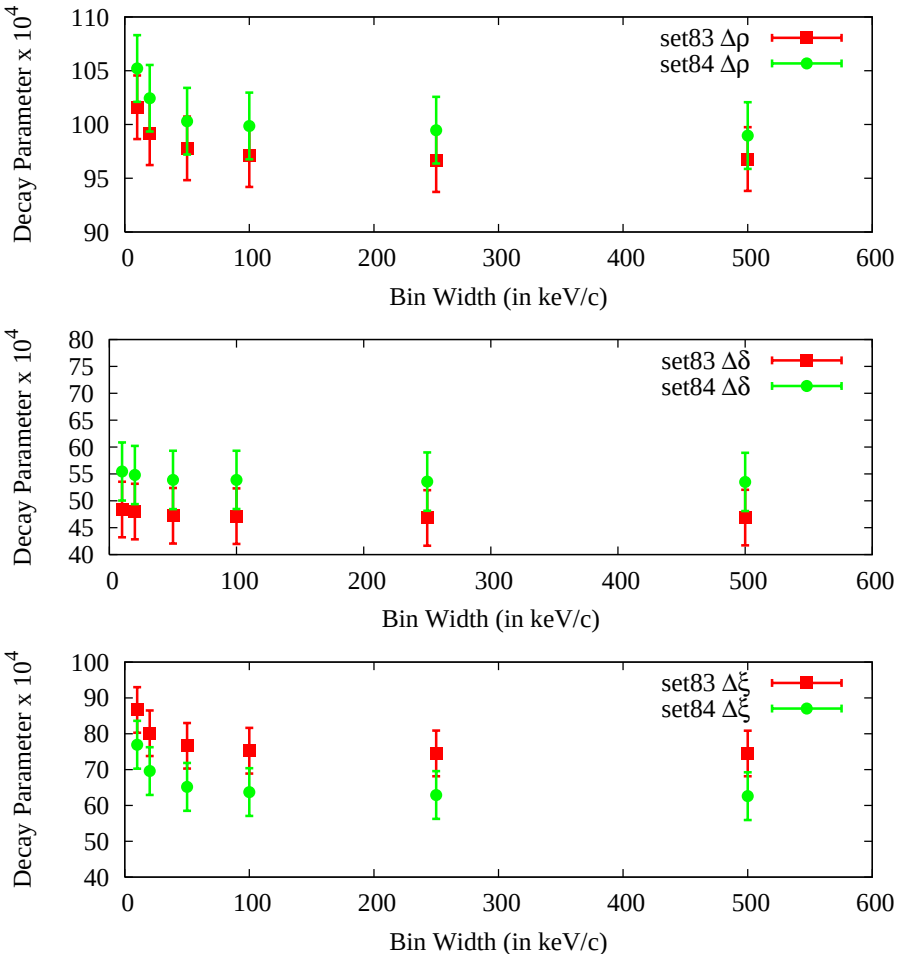

Figure 9.2: Biases for the decay parameters that results from using histogram momentum bins smaller than the nominal (500 keV) bin widths. This analysis used 10 keV bin widths which produce significant biases for ρ and $P_\mu\xi$. The same data sets were used for each point in the graphs so the errors are strongly correlated.

Target Material	Data	Simulation
Silver	3.025×10^8	8.850×10^8
Aluminum	2.517×10^8	5.839×10^8

Table 9.1: The number of counts in the fiducial region for data and simulation for both stopping targets.

distribution was derived using 65% of the runs used for the derivation of the simulated Ag response. The two distributions were added together to provide the model of the $\mu^+ \to e^+ X^0$ signal for the determination of its branching ratio.

9.3 The Search Algorithm

The search for a $\mu^+ \to e^+ X^0$ signal uses the following algorithm;

- The input files and histogram definitions are read from the configuration file. The input files include the suite of histograms used for the standard MC spectrum fitting (ie. data, base, and derivative histograms) described in Section 6.1. A 3-dimensional histogram containing the momentum response versus momentum and angle is also read into the program.

- A fit of the decay parameter differences between the data and Monte Carlo spectra is performed as described in Section 6.1.

- The program loops in finite steps across the momentum fiducial of the spectrum 50 keV/c wide. The momentum response is read into the algorithm centred at the chosen momentum in the same format as the other spectra.

- The data is fit to the base spectrum using the coefficients of the decay parameters and the amplitude of the two body decay signal as free parameters, for each 50 keV/c step in the loop. The results of the fit are stored for later analysis.

The results of the fits are compiled as functions of the peak momentum at the end of the algorithm. The fiducial region was expanded to include the endpoint of the decay spectrum so that $p_{tot} < 53.0$ MeV/c. Otherwise the fiducial limits on the positron momentum and angle for this measurement are identical to those described in Section 4.5.

The normalization of the $\mu^+ \to e^+ X^0$ signal was completed so that its fitting coefficient is the branching ratio. In the standard TWIST spectrum fitter, the derivative spectra are normalized by the N_{thrown} of the derivative spectrum. The peak used to model the signal is multiplied by an efficiency factor of the number of counts reconstructed in the base Monte Carlo spectrum divided by the number of positrons reconstructed in the peak, $N_{rec}^{eff}/N_{rec}^{peak}$. The total magnitude of the peak signal in the spectrum fit in the ith bin is $\Delta\mathcal{S} = A\mathcal{E}^{-1}\nu_i^{peak}$ where A is the fitting parameter of the peak and $\mathcal{E} = N_{rec}^{eff}/N_{thrown}^{eff}$ is the efficiency and $\nu_i^{peak} = N_i^{peak}/N_{rec}^{peak}$ is the

normalized content of the ith bin of the spectrum, as defined in Section 6.1. So,

$$\begin{aligned} \Delta\mathcal{S}_i &= A\frac{N^{eff}_{thrown}}{N^{eff}_{rec}}\frac{N^{eff}_{rec}}{N^{peak}_{thrown}}\frac{N^{peak}_{i}}{N^{peak}_{rec}} \\ &= A\frac{N^{base}_{thrown}N^{peak}_{i}}{N^{peak}_{thrown}N^{peak}_{rec}} \end{aligned} \tag{9.2}$$

where N^{peak}_{thrown} is the number of counts thrown in the spectrum used to sample the response peak. This normalization forces the A to be the integrated amplitude of the peak divided by the total number of reconstructed positron decays, $A = N^{peak}_{rec}/N^{eff}_{rec}$, which is the branching ratio.

To test whether the normalization procedure produces a reasonable measure of the branching ratio, a peak was added to a simulated decay spectrum and the peak search was run on the altered spectrum. The peak consisted of one run of isotropically distributed, mono-energetic positrons starting from the target. A total of 8.52×10^4 events were added to a spectrum of 1.075×10^8 events at 30 MeV/c. A branching ratio of $\mathcal{B} = 7.9\times10^{-4}$ is expected. The branching ratios measured from the test spectrum

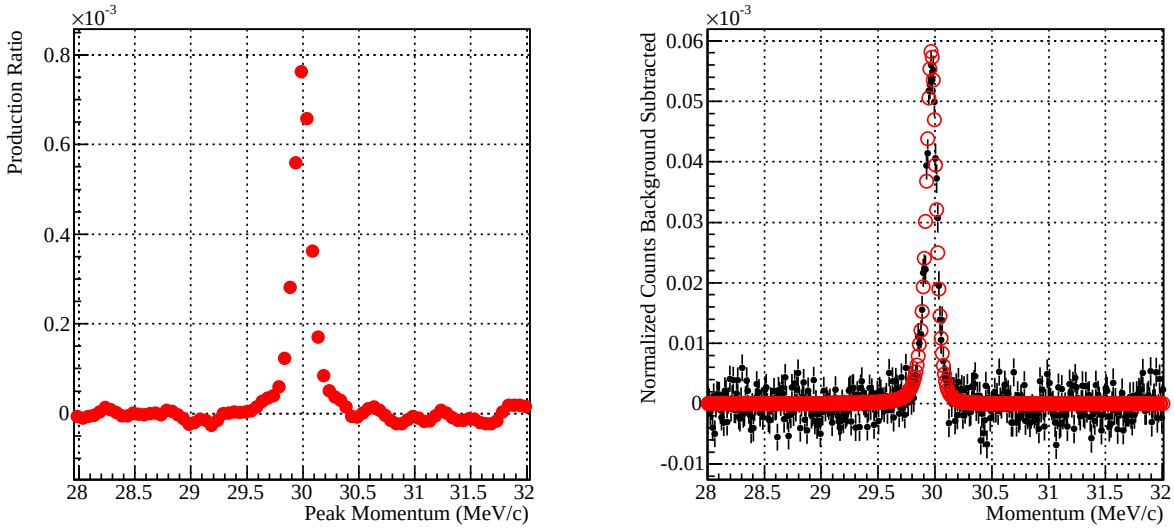

Figure 9.3: Figure on right shows the branching ratios measured from a simulation with a $\mu^+ \rightarrow e^+X$ peak added at 30 MeV/c. The branching ratio of the test peak was expected to be 0.79×10^{-3}. The right figure shows the normalized counts of the altered simulation with the background subtracted (•) accumulated in momentum bins 10 keV/c wide. The peak fit is overlaid (◯).

in the region about the generated peak is shown in Fig. 9.3. The largest measured peak has a branching ratio, $\mathcal{B} = (7.6 \pm 0.1) \times 10^{-4}$.

9.4 Statistical Considerations

The significance of potential signals must be well defined for this search. A p-value was defined describing the probability that the data for a given branching ratio that has a lesser or equal compatibility with the null hypothesis, as defined in Equation 32.37 of [4], and by Sinervo[50]. To calculate the p-value I define a test statistic, t, for the data where the observed value is

$$t_{obs} = \sqrt{\chi_0^2 - \chi_{obs}^2}, \text{ when } \chi_0^2 > \chi_{obs}^2 \tag{9.3}$$

where χ_0^2 is calculated for the spectrum fit without the peak added to the spectrum, while χ_{obs}^2 was calculated for the spectrum with a peak added. The p-value when

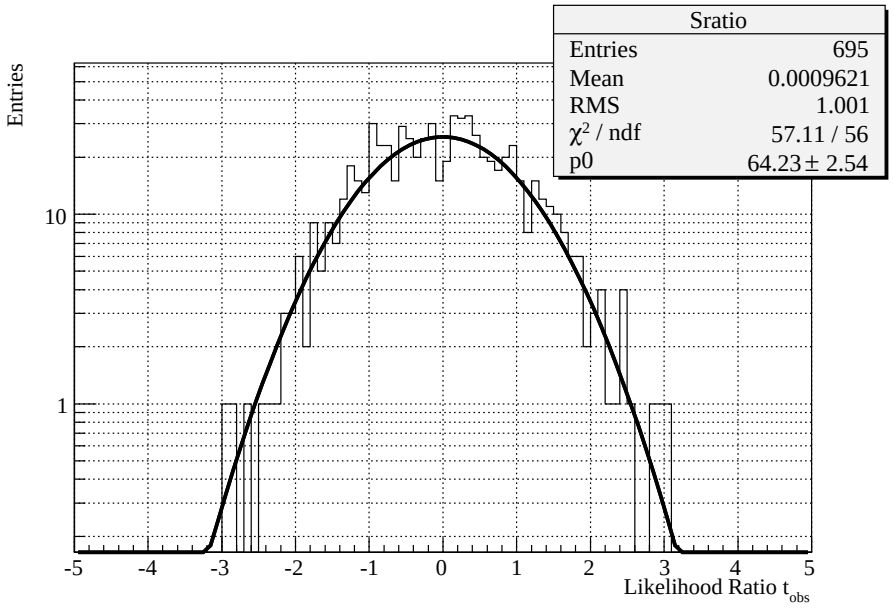

Figure 9.4: The distribution of t_{obs} generated from a peak search conducted between two uncorrelated simulations of standard model muon decays.

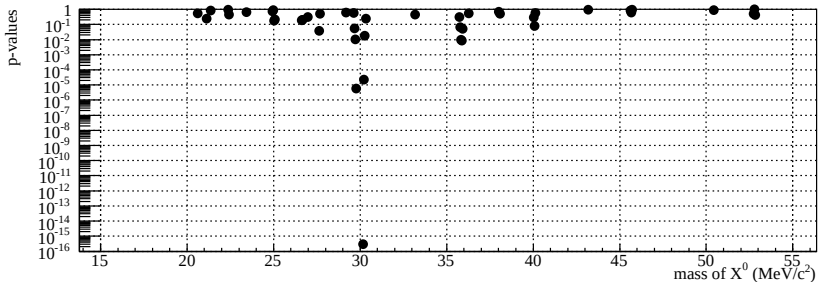

Figure 9.5: p-values expressed for peaks found in a difference between a simulated muon decay spectrum with a $\mu^+ \to e^+ X^0$ peak added at 30 MeV/c and a standard simulation, assuming that there are 64 uncorrelated trials.

multiple trials is considered is explicitly written in [51]

$$\begin{aligned} p &= P(t_{obs} > t|H_0; N_{trials}) \\ &\approx N_{trials} P(t_{obs} > t|H_0) = N_{trials} \frac{\mathrm{Erfc}(t_{obs}/\sqrt{2})}{2} \end{aligned} \tag{9.4}$$

where $P(t_{obs} > t|H_0)$ is the cumulative probability of observing a signal with a test statistic $t < t_{obs}$ given the null hypothesis H_0, when N_{trials} is the number of statistically independent trials within the investigated momentum range. This expression is only valid for $p < 1$. The number of trials can be estimated by considering the distribution of $sign(\mathcal{B})t_{obs}$ for a peak search completed between two uncorrelated simulations. A fit to the distribution using a normalized Gaussian distribution, with a mean value of 0 and a width of 1, will give the effective number of trials for this search. The distribution, shown in Fig. 9.4, indicates that the effective number of trials is 64. Alternatively, the argument can be made that consecutive peaks must be separated by 550 keV/c to be uncorrelated based on the results shown in Fig. 9.3. Assuming a momentum range between 17 and 52.8 MeV/c this means that the number of trials should be approximately 65. Fig. 9.5 shows the p-values of the test shown in Fig. 9.3. The p-value of the added peak in the branching ratio validation is 5.5 $\times 10^{-13}$. Other peaks appear in the figure at 28 and 36 MeV/c, but such false peaks are expected.

While the p-value defined in Eq. 9.4 is valid for a two body search in the bulk of the spectrum, a different definition is required for consideration of the mass-less case.

In this case, where the peak position is known, the p-value is simply

$$p = \mathrm{Erfc}\left(\left|\frac{\mathcal{B}}{\sqrt{2}\sigma_{\mathcal{B}}}\right|\right) \tag{9.5}$$

where $\mathcal{B}$ is the branching ratio and $\sigma_{\mathcal{B}}$ is its total uncertainty.

The confidence intervals for the branching ratios were defined using the method outlined by Feldman and Cousins [52]. The purpose of using this method is to avoid the requirement of a null hypothesis in the presence of small signals. This method defines a confidence region based on an ordering principle that assumes a null hypothesis for values of the branching ratio less than zero. The resulting confidence intervals provide continuous limits without having to make an a priori decision about whether an upper bound or an interval is called for in a given circumstance.

9.5 Systematics

The measurement of the peak amplitude has a few possible systematic effects relating to the calibration of the momentum and the detector resolution. The most significant systematic errors appear at the endpoint due to uncertainties in the ECal. Effects that alter the spectrum in a smooth way away from the endpoint will not affect the amplitude of a two body decay signal.

The presence of a positron peak at the endpoint will alter the momentum calibration. The magnitude of the change increases with the magnitude of the added peak. The parameters of the upstream endpoint as a function of the branching ratio of a decay producing NG boson is shown in Fig. 9.6 for endpoint fits between a simulation of the decay spectrum with a peak added at the endpoint and an uncorrelated simulation. The addition of a peak to the endpoint alters the parameters of the endpoint linearly with respect to the branching ratio of the decay at the endpoint. The ECal parameter B_{US} changes by 9.55 ± 0.12 keV/c and A_{US} changes by 5.54 ± 0.12 keV/c if the branching ratio of a decay at the endpoint is 10^{-4}. For branching ratio limits of parts in 10^5, this contribution drops below the statistical significance of the endpoint calibration fits. The downstream parameters are similarly affected by the addition of an isotropic peak.

Uncertainties in measurement of the branching ratio at the endpoint due to the ECal were calculated in the same way as for the standard TWIST analysis. The ECal will change the measured branching ratio at the endpoint of the spectrum far more

than in the bulk of the spectrum because a mismatch at the endpoint will create a large apparent peak. Away from the spectrum endpoint the difference between the data and the Monte Carlo simulation is smooth and will not appear as isolated $\mu^+ \to e^+ X^0$ signals.

To quantify the uncertainty of the $\mu^+ \to e^+ X^0$ branching ratio due to the ECal parameters, the tree analysis was performed on a simulated muon decay set four times; each time with a different momentum calibration parameter set to a selected value. The peak fitting procedure was applied to the calibrated spectra. The results established sensitivities for the branching ratios to the ECal parameters which were used to define of statistical uncertainties in the measurement of the branching fraction at each momentum, p_X, using the expression,

$$\sigma^2_{\mathcal{B}}(p) = \frac{\partial \mathcal{B}(p)}{\partial q_\alpha} \frac{\partial \mathcal{B}(p)}{\partial q_\beta} V_{\alpha\beta}. \tag{9.6}$$

As in Section 6.2.3, $q_\alpha \in \{a_{up}, b_{up}, a_{dn}, b_{dn}\}$ is the set of the endpoint parameters while $V_{\alpha\beta}$ is the covariance between the q_α and q_β. At a given peak momentum, p_X, the final uncertainties were averaged over all data sets used in the search.

The same calculation is used to determine the magnitude of an effect due to the "ecmc model systematic". This effect is introduced by defining a matrix

$$V = \begin{pmatrix} 0 & 0 & 0 & 0 \\ 0 & (1.6\text{ keV})^2 & 0 & (1.6\text{ keV})^2 \\ 0 & 0 & 0 & 0 \\ 0 & (1.6\text{ keV})^2 & 0 & (1.6\text{ keV})^2 \end{pmatrix} \tag{9.7}$$

to approximate the unknown uncertainties in the endpoint calibration model. This assumes that there is a 100% correlation between the upstream and the downstream uncertainty. Assuming that there is no correlation between the offsets results in a smaller, less conservative, uncertainty from this contribution. Both endpoint calibration uncertainties were added in quadrature to the base statistical uncertainty determined by the fit for the $\mu^+ \to e^+ X^0$ signal.

The calculated systematic uncertainty at the endpoint is significant. The uncertainties calculated using Eq. 9.6 for the peaks near the endpoint are shown in the Table 9.2. The statistical uncertainty and the branching ratios of these data points are also shown. The p-values of peaks appearing at the given momenta shown in Table

		In units of $\times 10^{-6}$				
p (MeV/c)	m_{X^0} (MeV/c^2)	$\mathcal{B}$	Base Stat.	Ecal. Stat.	Ecal. Sys.	p-value
52.825	0.89	12.6	1.72	4.88	13.7	0.28
52.775	3.37	12.7	2.13	8.82	13.3	0.37
52.725	4.68	9.02	2.46	10.9	10.6	0.60
52.575	7.32	-1.79	3.03	4.16	4.16	0.83
52.425	9.24	2.17	3.29	0.81	0.41	0.93

Table 9.2: Branching fractions and their uncertainties for two body decay signals near the endpoint. The probability that these peaks are consistent with the null hypothesis are shown in the right most column. This shows that the effect of the momentum calibration decreases away from the endpoint. Because the momentum bins were defined to be 10 keV/c in width, the peak closest to the endpoint peaks is consistent with a boson with a mass of 0.89 MeV/c^2.

9.2 include the systematic uncertainty using Eq. 9.5. After including the systematic uncertainty the measured $\mu^+ \to e^+ X^0$ are consistent with the null hypothesis.

Equation 9.6 still requires that the branching ratios increase linearly with the endpoint parameters. The linearity was tested by calculating the sensitivity of the branching ratio to the endpoint calibration parameters using parameters altered by 50 keV/c and 100 keV/c. The results suggest that the uncertainty does not scale linearly at all momenta. However, the deviation is small except for cases below the endpoint between 52.2 MeV/c and 52.6 MeV/c. At 52.8 MeV this non-linearity is not noticeable.

9.6 Results

The measured branching ratios and their uncertainties are shown in Fig. 9.7. While decay signals were determined at all momenta throughout the fiducial region, peaks determined below 20 MeV/c were ignored for the sake of this discussion because of the relatively small statistics due to the fiducial constraints. The 90% confidence intervals, as functions of the inferred X^0 mass, are shown in Fig. 9.8. The associated p-values less than 1 are shown in Fig. 9.9.

These results are summarized in Table 9.3. Three potential cases for the angular behaviour of the decay signal were tested; an isotropic decay signal, a negative anisotropic decay signal, where the angular behaviour matches that of the muon decay spectrum, and a positive anisotropy. Results for mass-less, Nambu-Goldstone boson,

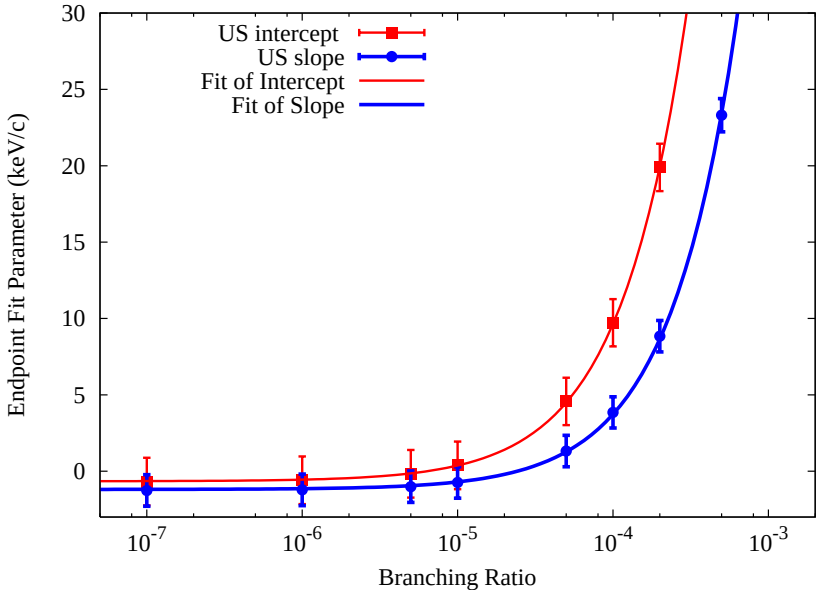

(a) Upstream endpoint calibration parameters

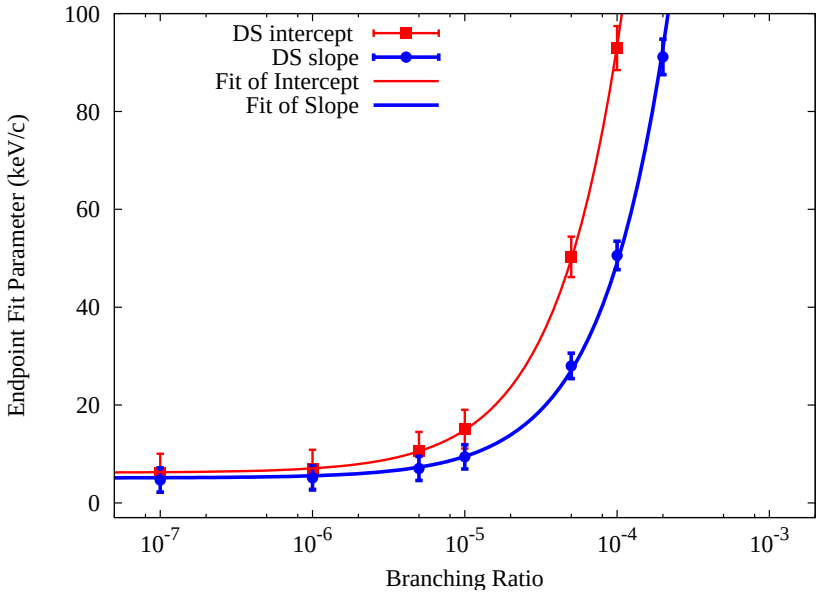

(b) Downstream endpoint calibration parameters

Figure 9.6: The upstream (a) and downstream (b) endpoint calibration fit parameters measured from adding a isotropic peak at a momentum of 52.828 MeV/c, corresponding to a two-body decay generating a mass-less boson.

and the average branching ratio for massive pseudo-Goldstone bosons are shown. The average 90% upper limits are shown with black lines relative to the 90% confidence intervals in Fig 9.8. The p-values for the NG bosons and the minimum p-values for

the pNG bosons are shown. All of the p-values for the NG bosons are consistent with the null hypothesis at the 30% level. In contrast the minimum p-values for the detection pNG bosons is on the order of 10% when the background and the signal are of very different anisotropies, and 3% when the signal matches the background. The calculated upper limits are likewise larger to reflect this behaviour.

The previously published measurements are also shown for comparison. These results show a significant improvement on the upper limits on the branching ratio of pNG bosons. The limits on NG bosons are only interesting in the case of a negative anisotropy in the decay signal because the Jodidio measurement involved a sample with a much larger event density over a much smaller phase space ($\cos\theta > 0.97$) with a better relative resolution.

These minimum p-values are for the discovery of a boson at 56 MeV/c^2 or $p_X = 37$ MeV/c. This feature appears regardless of the assumed anisotropy of the signal and is common to Ag and Al target data.

Decay signal		90% Upper Limit	p-value
Isotropic	Average	8.1×10^{-6}	0.10
	Endpoint	3.3×10^{-5}	0.31
Negative Anisotropic	Average	8.4×10^{-6}	0.03
	Endpoint	6.7×10^{-5}	0.34
Positive Anisotropic	Average	5.7×10^{-6}	0.10
	Endpoint	8.5×10^{-6}	0.28
Bryman, 1986 [22]	Average	3×10^{-4}	
Jodidio, 1986 [23]	Endpoint	2.5×10^{-6}	

Table 9.3: The 90% upper limits on the branching ratios of two body decays assuming isotropic, negative anisotropic, and positive anisotropic decay signals. The average value through the spectrum and the upper limit at the endpoint is shown along with the p-values determined from the measured branching ratio. Also shown are the two comparable previous measurements. This represents an improvement in the limit on pNG bosons by a factor of 37. The limit on NG bosons is not competitive in the isotropic or positive anisotropic case, while the Jodidio result is not applicable to the negative anisotropic result.

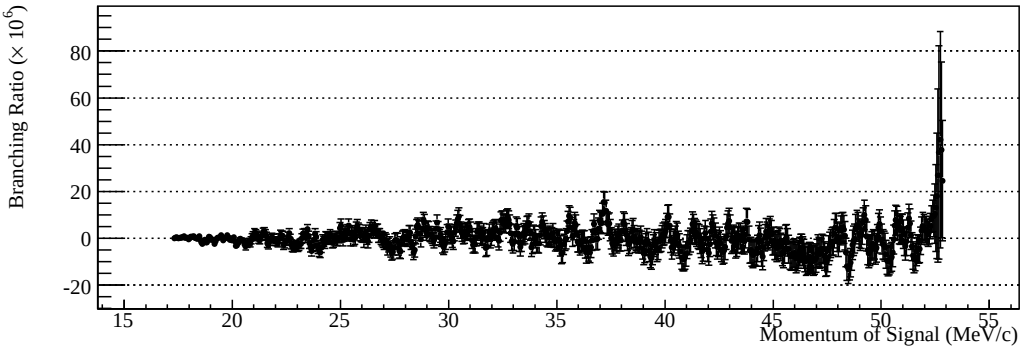

(a) Two body decay branching ratios measured from the TWIST data assuming a negative anisotropic signal

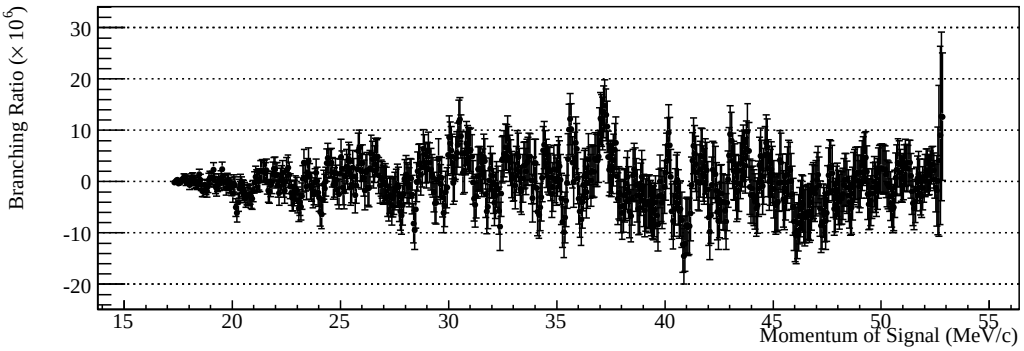

(b) Two body decay branching ratios measured from the TWIST data assuming an isotropic signal

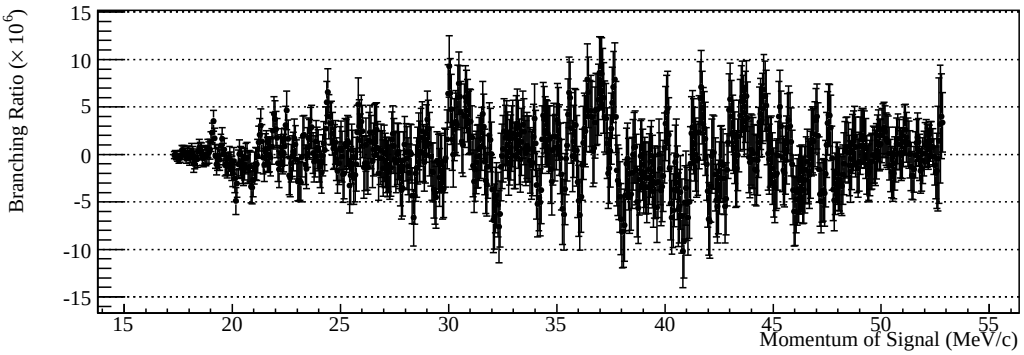

(c) Two body decay branching ratios measured from the TWIST data assuming a positive anisotropic signal

Figure 9.7: The branching ratios measured from the decay spectrum as a function of the decay positron momentum.

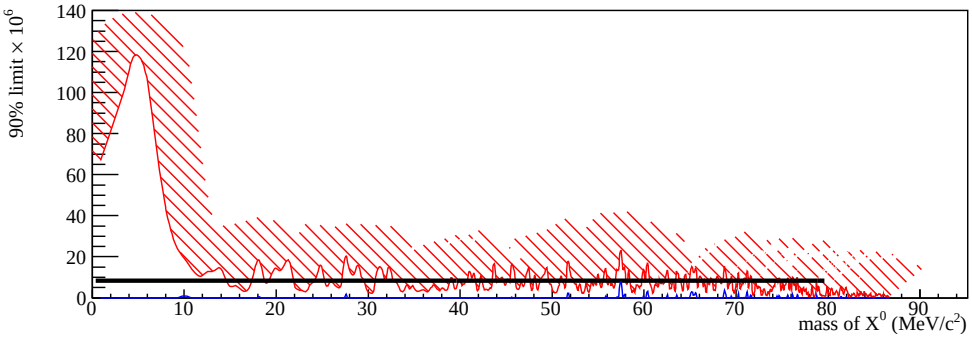

(a) Confidence intervals defined for negative anisotropic decay signals

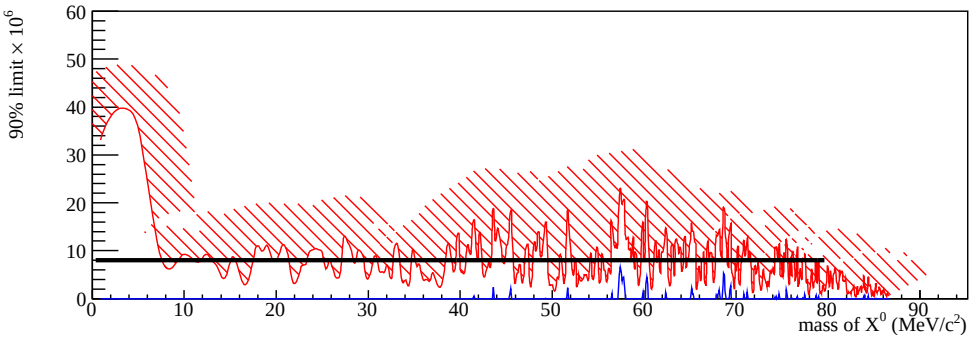

(b) Confidence intervals defined for isotropic decay signals

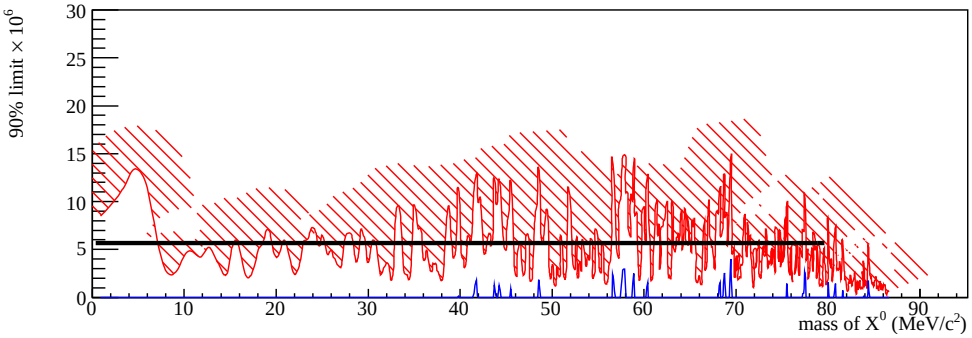

(c) Confidence intervals defined for positive anisotropic decay signals

Figure 9.8: 90% FC confidence intervals on the production of isotropic and anisotropic two body decay signals. Limits when positrons preferentially appear upstream of the target is shown in the upper graphic, while the limits for preferential downstream decays appear in the lower graphic. The allowed region is between the shaded (red) upper limits and the lower limits (blue). The thick black line shows the average value of the upper limits.

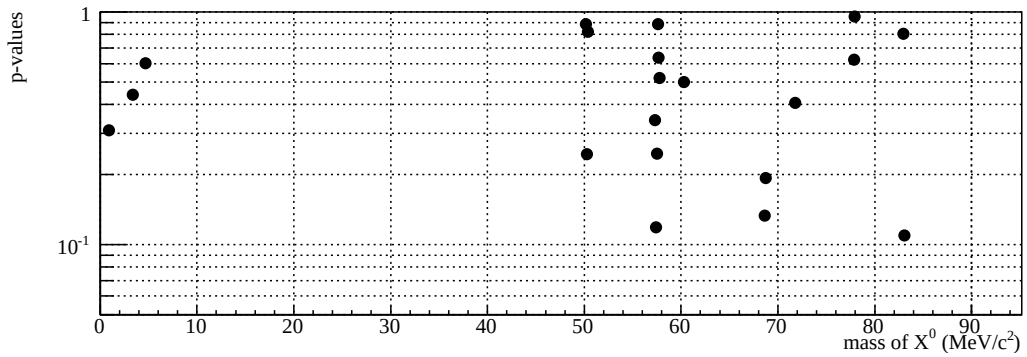

Figure 9.9: p-values less than 1 determined for the likelihood of observing the measured branching ratio corresponding to the production of a pNG boson of mass m_{X^0} with a isotropic decay signal assuming that there are no two body decay signal anywhere in the spectrum.

Chapter 10

Conclusion

The TWIST experiment is successful in its precision goals of an order of magnitude improvement over previous measurements of the muon decay parameters. The measured value of the isotropic parameter that resulted from the blinded analysis of the TWIST data is $\rho = 0.74991 \pm 0.00009(\text{stat}) \pm 0.00028(\text{sys})$. This is compared with the results reported by Derenzo in 1969 of $\rho = 0.7518 \pm 0.0026$. The measured value of ρ is completely consistent with the $V - A$ prediction of 3/4. This measurement in combination with the decay parameters $P_\mu \xi$ and δ has some significant ramifications for the determination of the some of the weak interaction coupling constants.

There is a significant inconsistency in the blinded measurement because the value of the combination $P_\mu \xi \delta / \rho$ is greater than 1. This suggests that there is a (small) region of the decay positron spectrum that is not positive-definite, which is not physically possible. This region is well outside of the fiducial region of the spectrum, so it is not feasible to verify this directly. The source of this inconsistency is under continuing investigation. At this time a conclusion for this investigation has not been reached.

The rare decay search conducted with the TWIST data did not find evidence for a two body decay signal. The search for $\mu^+ \to e^+ X^0$ decay signals when the X^0 particle is massive generated some significant improvements on the 90% upper limits on the branching ratios over previous searches. Three different classes of signals were considered for the search; the limit on isotropic decay signals was 8.1×10^{-6}, the limit on signals with anisotropy matching the background was 8.4×10^{-6}, and the limit on signals with anisotropy opposite to the background was 5.7×10^{-6}. This is the first direct search for these anisotropic signals, while the isotropic limit constitutes a factor of 37 improvement on the previous comparable limit.

Limits for decays involving mass-less X^0 are strongly limited by the systematics. These decays occur in a region that is strongly affected by the momentum calibration procedures, and so shape measurements in this region are strongly affected by the uncertainties on the endpoint calibration procedure itself. The 90% upper limit on isotropic signals consistent with mass-less X^0 is 3.3×10^{-5}; a factor of 13 larger than the previously published limits. The branching ratio of mass-less signals with anisotropy matching the background muon decays have a 90% upper limit of 6.7×10^{-5}. The true strength of this measurement is its ability for setting a direct branching ratio on mass-less signals with anisotropy opposite to the background muon decays two which previous experiments are not sensitive. In this special case a 90% upper limit on the branching ratio of 8.5×10^{-6} is set using the TWIST data.

Bibliography

[1] R. MacDonald *et al.*, "Precision measurement of the muon decay parameters ρ and δ," *Phys. Rev.*, vol. D78, p. 032010, 2008.

[2] L. Rosenson, "Momentum spectrum of positrons from the decay of μ^+ mesons," *Phy. Rev.*, p. 958, February 1958.

[3] L. Rosenson, "Measurement of the muon-decay spectrum with a wire spark-chamber spectrometer," *Phys. Rev.*, p. 1967, April 1967.

[4] C. Amsler *et al.*, "Review of particle physics," *Phys. Lett.*, vol. B667, p. 1, 2008.

[5] P. Herczeg, "On decay in left-right-symmetric electroweak models," *Phys. Rev. D*, vol. 34, pp. 3449–3456, December 1986.

[6] D. H. Perkins, *Introduction to High Energy Physics*. New York: Cambridge University Press, fourth. ed., 2000.

[7] D. J. Griffiths, *Introduction to Elementary Particles*. John Wiley and Sons, 1987.

[8] C. M. G. Lattes, G. P. S. Occhialini, and C. F. Powell, "Observations on the tracks of slow mesons in photographic emulsions. 1," *Nature*, vol. 160, pp. 453–456, 1947.

[9] E. P. Hincks and B. Pontecorvo, "The absorption of charged particles from the 2.2-mu-sec meson decay," *Phys. Rev.*, vol. 74, pp. 697–698, 1948.

[10] J. Steinberger, "On the Use of subtraction fields and the lifetimes of some types of meson decay," *Phys. Rev.*, vol. 76, pp. 1180–1186, 1949.

[11] L. Michel, "Interaction between four half spin particles and the decay of the mu meson," *Proc. Phys. Soc.*, vol. A63, pp. 514–531, 1950.

[12] S. E. Derenzo, "Measurement of the low-energy end of the mu-plus decay spectrum," *Phys. Rev.*, vol. 181, pp. 1854–1866, 1969.

[13] E. P. Hincks and B. Pontecorvo, "Search for gamma-radiation in the 2.2-microsecond meson decay process," *Phys. Rev.*, vol. 73, pp. 257–258, 1948.

[14] W. Fetscher, H. J. Gerber, and K. Johnson, "Muon decay: Complete determination of the interaction and comparison with the standard model," *Phys. Lett. B*, vol. 173, pp. 102–106, May 1986.

[15] W. Fetscher and H. J. Gerber, "Precision measurements in muon and tau decays," *Adv. Ser. Direct. High Energy Phys.*, vol. 14, pp. 657–705, 1995.

[16] A. Arbuzov and K. Melnikov, "$\mathcal{O}(\alpha^2 \ln(m_\mu/m_e))$ corrections to electron energy spectrum in muon decay," *Phy. Rev.*, vol. D66, p. 093003, 2002.

[17] A. Arbuzov, A. Czarnecki, and A. Gaponenko, "Muon decay spectrum: Leading logarithmic approximation," *Phy. Rev.*, vol. D65, p. 113006, 2002.

[18] C. A. Gagliardi, R. E. Tribble, and N. J. Williams, "Global analysis of muon decay measurements," *Phys. Rev.*, vol. D72, p. 073002, 2005.

[19] R. J. Erwin, J. Kile, M. J. Ramsey-Musolf, and P. Wang, "Neutrino mass implications for muon decay parameters," *Phys. Rev.*, vol. D75, p. 033005, 2007.

[20] M. Collaboration, M. L. Brooks, *et al.*, "New limit for the family-number non-conserving decay $\mu^+ \to e^+\gamma$," *Phys.Rev.Lett.*, vol. 83, pp. 1521–1524, 1999.

[21] U. Bellgardt *et al.*, "Search for the decay $\mu^+ \to e^+e^+e^-$," *Nucl. Phys.*, vol. B299, p. 1, 1988.

[22] D. A. Bryman and E. T. H. Clifford, "Exotic muon decay $\mu \to ex$," *Phys. Rev. Lett.*, vol. 57, p. 2787, 1986.

[23] A. Jodidio, B.Balke, *et al.*, "Search for right-handed currents in muon decay," *Physical Review D*, vol. 34, no. 7, pp. 1967–1990, 1986.

[24] R. Eichler *et al.*, "Limits for shortlived neutral particles emitted μ^+ or π^+ decay," *Phys. Lett.*, vol. B175, p. 101, 1986.

[25] M. Hirsch, A. Vicente, J. Meyer, and W. Porod, "Majoron emission in muon and tau decays revisited," *Phys. Rev. D*, no. 79, p. 055023, 2009.

[26] J. Hu, G. Sheffer, Y. Davydov, D. Gill, P. Gumplinger, R. Henderson, B. Jamieson, C. Lindsay, G. Marshall, K. Olchanski, A. Olin, R. Openshaw, and V. Selivanov, "Time expansion chamber system for characterization of twist low-energy muon beams," *Nuclear Instruments and Methods in Physics Research Section A: Accelerators, Spectrometers, Detectors and Associated Equipment*, vol. 566, no. 2, pp. 563–574, 2006.

[27] J. Bueno, *A direct measurement of $P_\mu^\pi \xi$ from muon decay.* PhD thesis, University of British Columbia, 2009.

[28] R. S. Henderson *et al.*, "Precision planar drift chambers and cradle for the twist muon decay spectrometer," *Nucl. Instrum. Meth.*, vol. A548, pp. 306–335, 2005.

[29] A. Hillairet, "Window and event classification." Private Communication—TWIST Software Forum Posting: key=1220394735, June 2008.

[30] R. Armenta, "Twist magnet: Field map study final report." TWIST Technical Note TN-68, August 2002.

[31] G. Marshall, "Comparisons of field maps and opera maps in the tracking regions: I:nmr maps and opera." Private Communication—TWIST Physics Forum Posting: key=1237499093, March 2009.

[32] A. Hillairet, "Drift chambers alignment." Private Communication—TWIST Alignment Forum Posting:key=1194305614, November 2007.

[33] R. Brun and F. Rademakers, "ROOT: An object oriented data analysis framework," *Nucl. Instrum. Meth.*, vol. A389, pp. 81–86, 1997. Also see `root.cern.ch`.

[34] A. S. G. "Computing and N. Division", "Geant – detector description and simulation tool," CERN Program Library Long Writeup W5013, CERN Geneva, Switzerland, CH-1211 Geneva 23, Switzerland, 1993.

[35] J. Bueno, "Re:target thickness: Ag re-measured." Private Communication—TWIST General Forum Posting: key=1245099786, June 2009.

[36] M. Paterno, "Calculating inefficiencies and their uncertainties." `http://home.fnal.gov/~paterno/images/effic.pdf`, May 2003.

[37] A. Gaponenko, "Monte-carlo fitting: the spectrum expansion." TWIST Technical Note TN-80, April 2003.

[38] R. Barlow and C. Beeston, "Fitting using finite monte carlo samples," *Computer Physics Communications*, vol. 77, no. 2, pp. 219 – 228, 1993.

[39] G. Marshall, "Comparisons of field maps and opera maps in the tracking regions: Iv: Opera corrections for hall and nmr maps at 2.0 t." Private Communication—TWIST Physics Forum Posting: key=1240340214, April 21 2009.

[40] B. Jamieson *et al.*, "Measurement of p(mu) xi in polarized muon decay," *Phys. Rev.*, vol. D74, p. 072007, 2006.

[41] R. MacDonald, *A precision measurement of the muon decay parameters Rho and Delta*. PhD thesis, University of Alberta, June 2008.

[42] A. Grossheim, "Resolution systematic." Private Communication—TWIST Physics Forum Posting: key=1249269764, August 2009.

[43] A. Olin, "Re: Length scale systematics for relative ecal, gen 584." Private Communication—TWIST Physics Forum Posting, July 2009.

[44] A. Hillairet, "Cathode foil position systematic." Private Communication—TWIST Physics Forum: key=1258406918, November 2009.

[45] B. Balke *et al.*, "Precise measurement of the asymmetry parameter δ in muon decay," *Phys. Rev.*, vol. D37, pp. 587–617, 1988.

[46] I. Beltrami *et al.*, "Muon decay: Measurement of the integral asymmetry parameter," *Phys. Lett.*, vol. B194, pp. 326–330, 1987.

[47] H. Burkard *et al.*, "Muon decay: Measurement of the positron polarization and implications for the spectrum shape parameter eta, v-a and t invariance," *Phys. Lett.*, vol. B150, pp. 242–246, 1985.

[48] N. Danneberg *et al.*, "Muon decay: Measurement of the transverse polarization of the decay positrons and its implications for the Fermi coupling constant and time reversal invariance," *Phys. Rev. Lett.*, vol. 94, p. 021802, 2005.

[49] C. A. Gagliardi, "Re: Final decay parameters results, delta coversion adjusted." Private Communication—TWIST Physics Forum Posting, February 2010.

[50] P. K. Sinervo, "Signal significance in particle physics," in *Durham 2002, Advanced statistical techniques in particle physics*, pp. 64–76, 2002.

[51] B. Aubert *et al.*, "Search for dimuon decays of a light scalar boson in radiative transitions $\Upsilon \to \gamma A^0$," *Phys.Rev.Lett.*, vol. 103, p. 081803, 2009.

[52] G. J. Feldman and R. D. Cousins, "A unified approach to the classical statistical analysis of small signals," *Phys.Rev.D*, vol. 57, pp. 3873–3889, 1998.